logarithmic potential (spheroidal)

$$\Phi_{\rm eff} = \tfrac{1}{2}v_0^2 \ln\left(R^2 + \frac{z^2}{q^2}\right) + \frac{L_z^2}{2R^2}, \qquad (3.70)$$

for a given Lz
a special orbit

guiding centre:
minimum in $\Phi_{\rm eff}$.

$$\frac{\partial \Phi_{\rm eff}}{\partial R} = 0$$

$$\frac{\partial \Phi_{\rm eff}}{\partial z} = 0$$

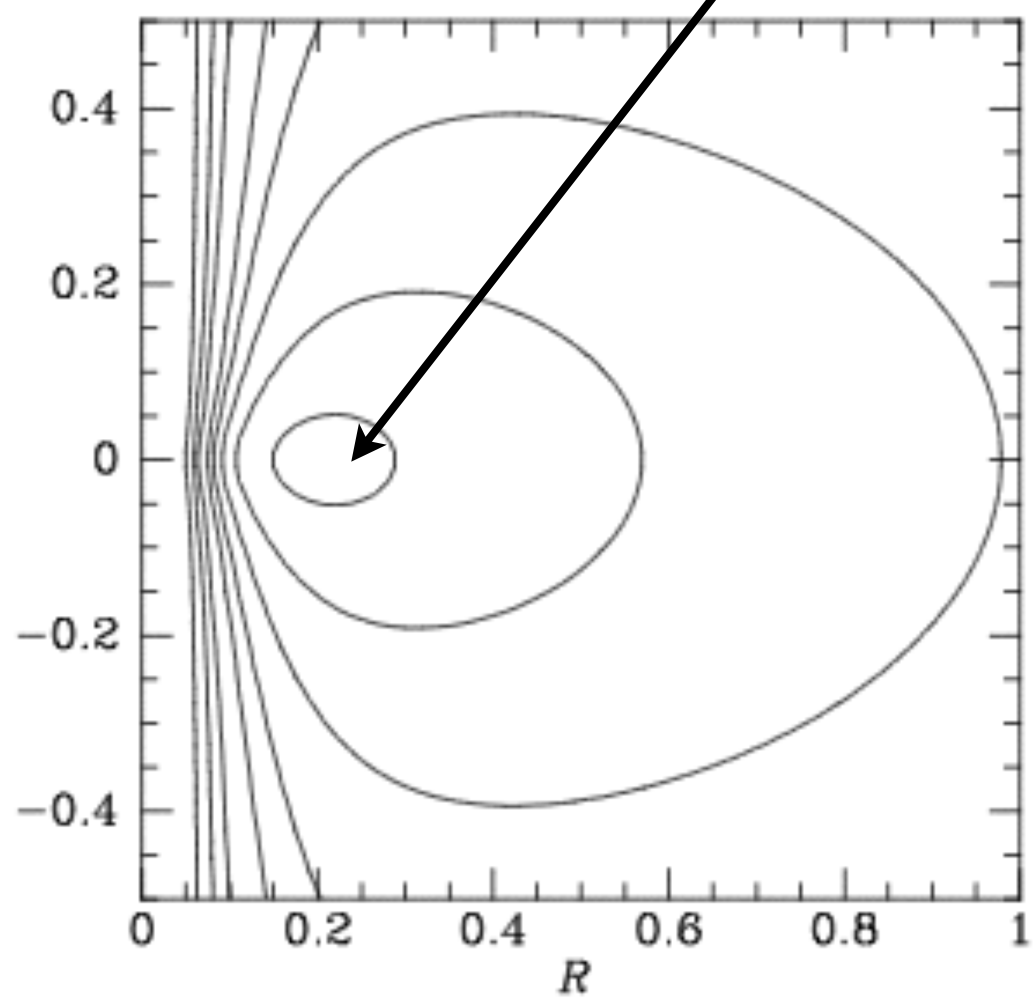

otential of equation (3.70) when $v_0 = 1$,
−0.5, 0, 0.5, 1, 1.5, 2, 3, 5. The axis ratio
ight.

different zvc for orbits of different E/Lz

The epicycle approximation

Epicycle direction are always retrograde;
opposite to planetary orbits

at apo-apse, moves slower relative to circular orbit

$$x(t) = X\cos(\kappa t + \alpha), \qquad y = -\gamma X \sin(\kappa t + \alpha) \equiv -Y\sin(\kappa t + \alpha).$$

$$\boxed{\gamma \equiv \frac{2\Omega_g}{\kappa}}$$

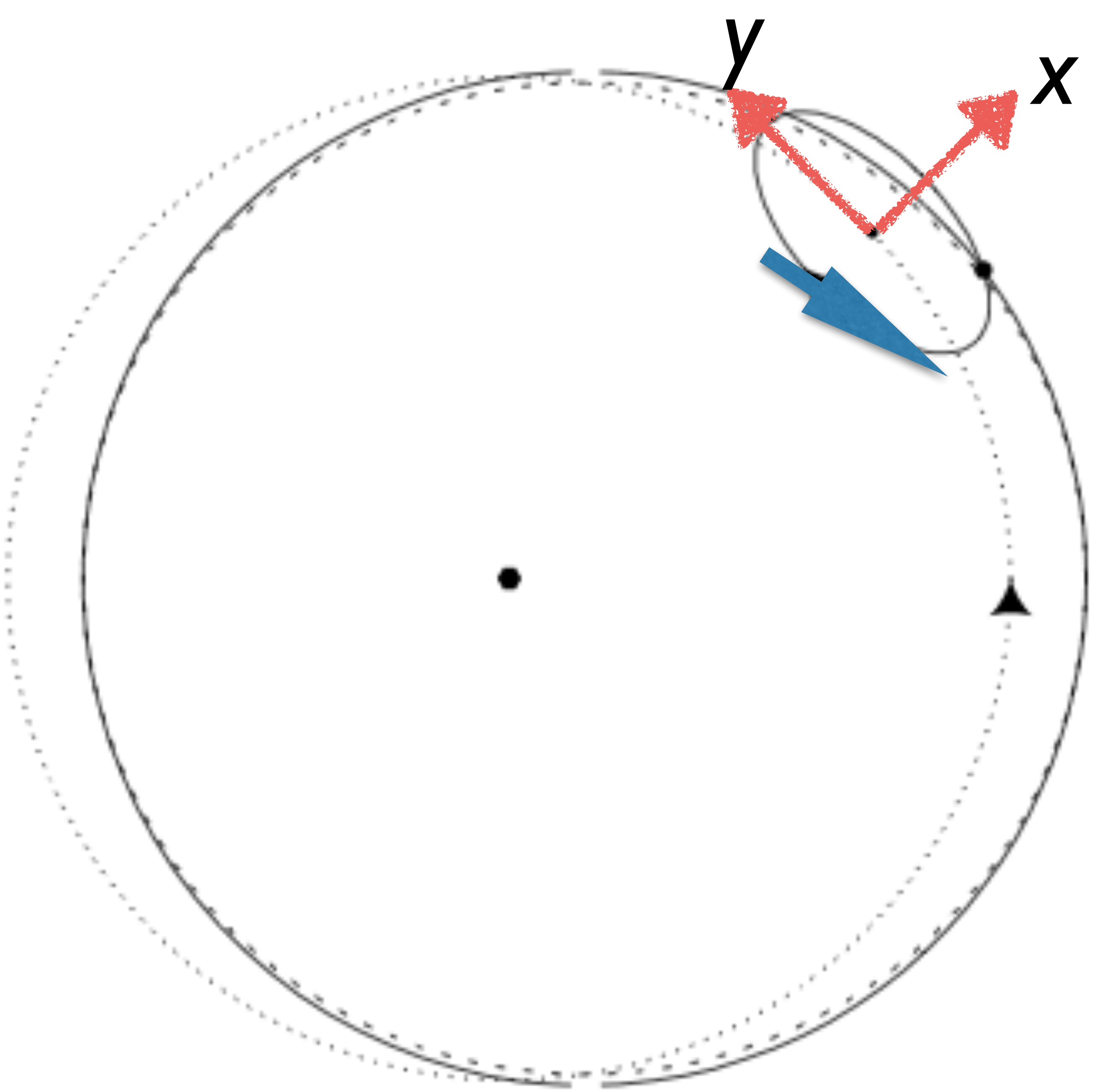

Keplerian: X/Y = 0.5
Harmonic: X/Y = 1
Galatic: X/Y ~ 0.7

$$\dot{x}^2 \equiv \sigma_R^2 = \tfrac{1}{2}\kappa^2 X^2$$
$$\dot{y}^2 \equiv \sigma_\theta^2 = \tfrac{1}{2}\kappa^2 Y^2$$

for stars with the same guiding center orbits

The epicycle approximation

vertical frequency: ν

radial frequency: κ

rotational frequency: Ω

independent measures of the potential

1st application: taking <v> of solar neighbourhood

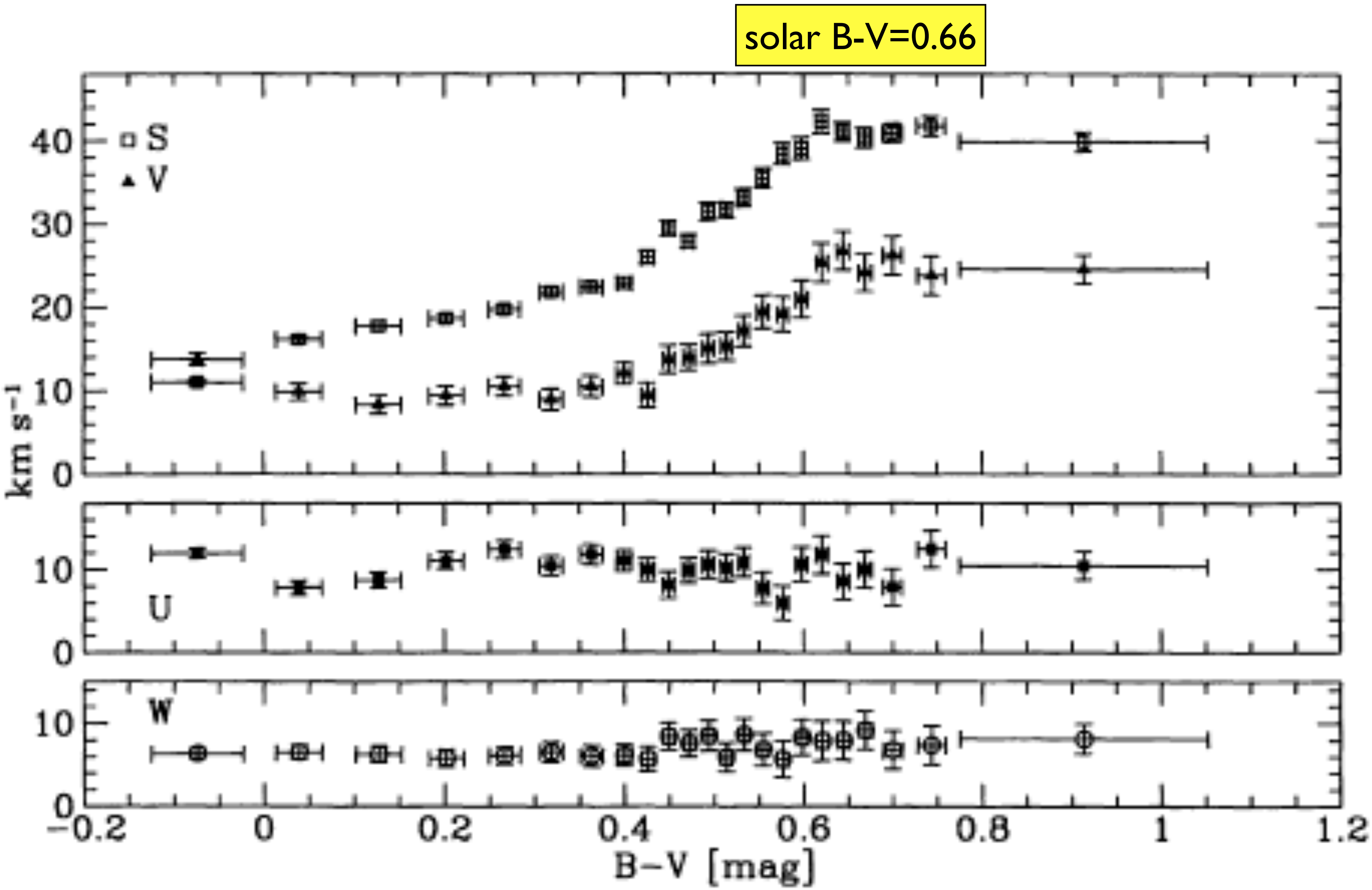

mponents U, V and W of the solar motion with respect to stars with different colour $B-V$. Also shown is the variation of the

2nd application: velocity dispersion

$$\sigma_i^2 =< (v_i - \bar{v}_i)^2 >$$

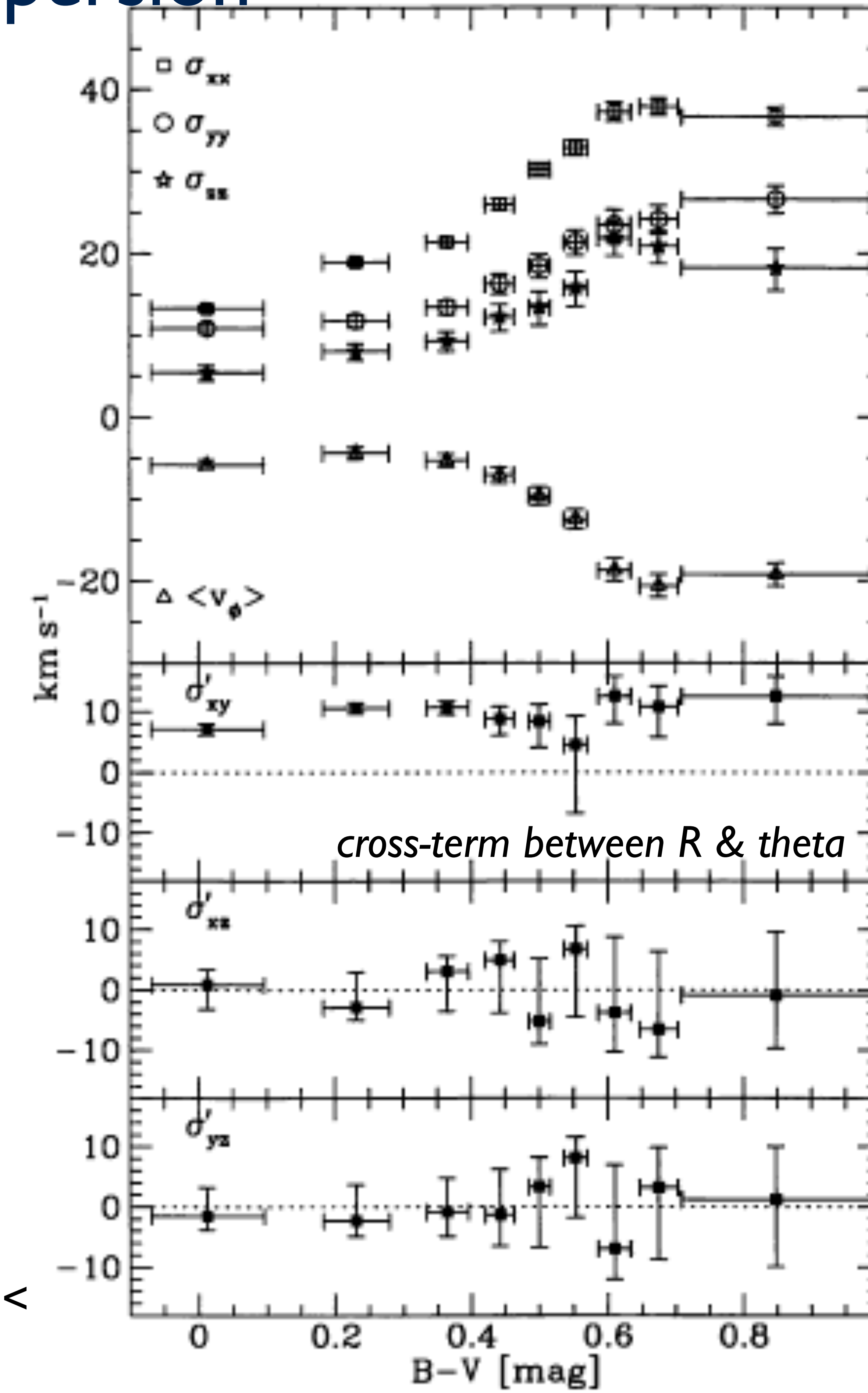

Figure 5. Velocity dispersions for stars in different colour bins. The top panel shows the mean rotation velocity (negative values imply lagging with respect to the LSR) and the three main velocity dispersions. In the three bottom panels $\sigma'_{ij} = \mathrm{sign}(\sigma^2_{ij})\,|\sigma^2_{ij}|^{1/2}$ is plotted for the mixed components of the tensor σ^2_{ij}.

for stars near the mid-plane (Hipparcos data, |z| < 100pc), Dehnen & Binney '98

Measuring Solar peculiar velocities (u_0, v_0, w_0)

by taking neighbourhood <V> averages

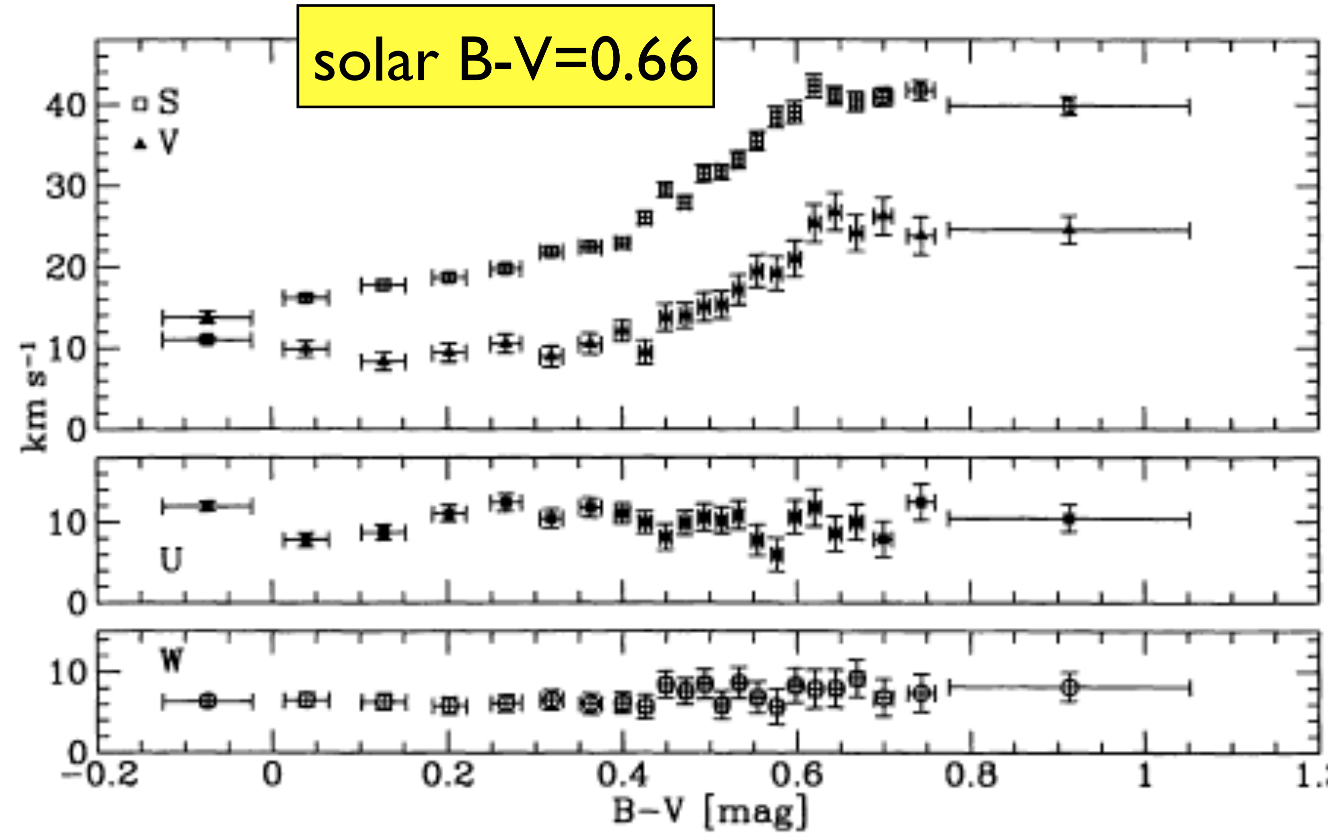

Figure 3. The components U, V and W of the solar motion with respect to stars with different colour $B-V$. Also shown is the variation of the dispersio
colour.

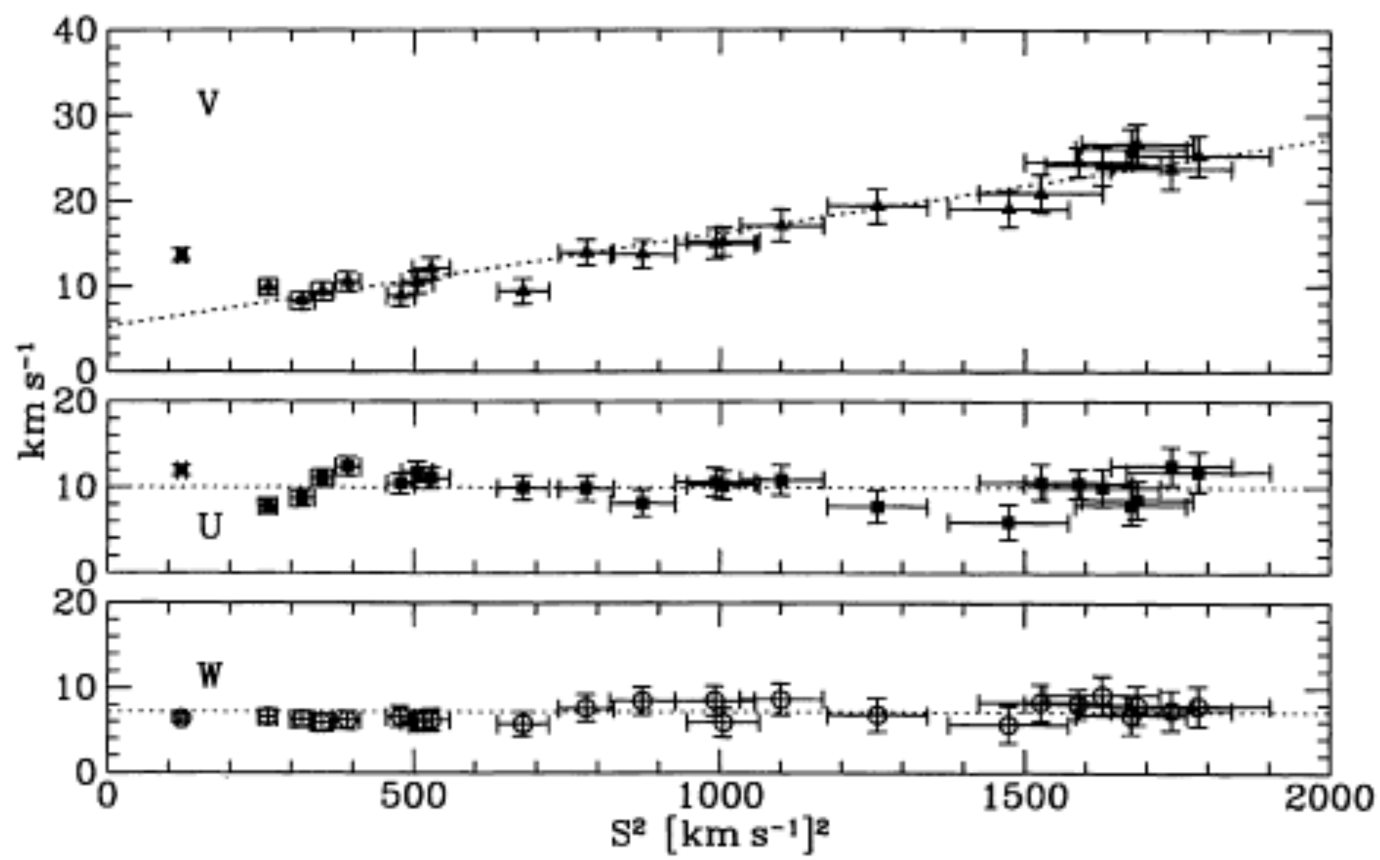

Figure 4. The dependence of U, V and W on S^2. The dotted lines correspond to the linear relation fitted (V) or the mean values (U and W) for stars bl
$B-V=0$.

extrapolating back to $S=0$. Ignoring stars blueward of $B-V=0$ mag we find

$$\begin{aligned} U_0 &= 10.00 \pm 0.36 \quad (\pm 0.08) \quad \mathrm{km\,s^{-1}}, \\ V_0 &= 5.25 \pm 0.62 \quad (\pm 0.03) \quad \mathrm{km\,s^{-1}}, \qquad (20) \\ W_0 &= 7.17 \pm 0.38 \quad (\pm 0.09) \quad \mathrm{km\,s^{-1}}, \end{aligned}$$

Dehnen & Binney '98

Schematic distributions of local (u,v)

u: R-direction, x
v: theta-direction, y

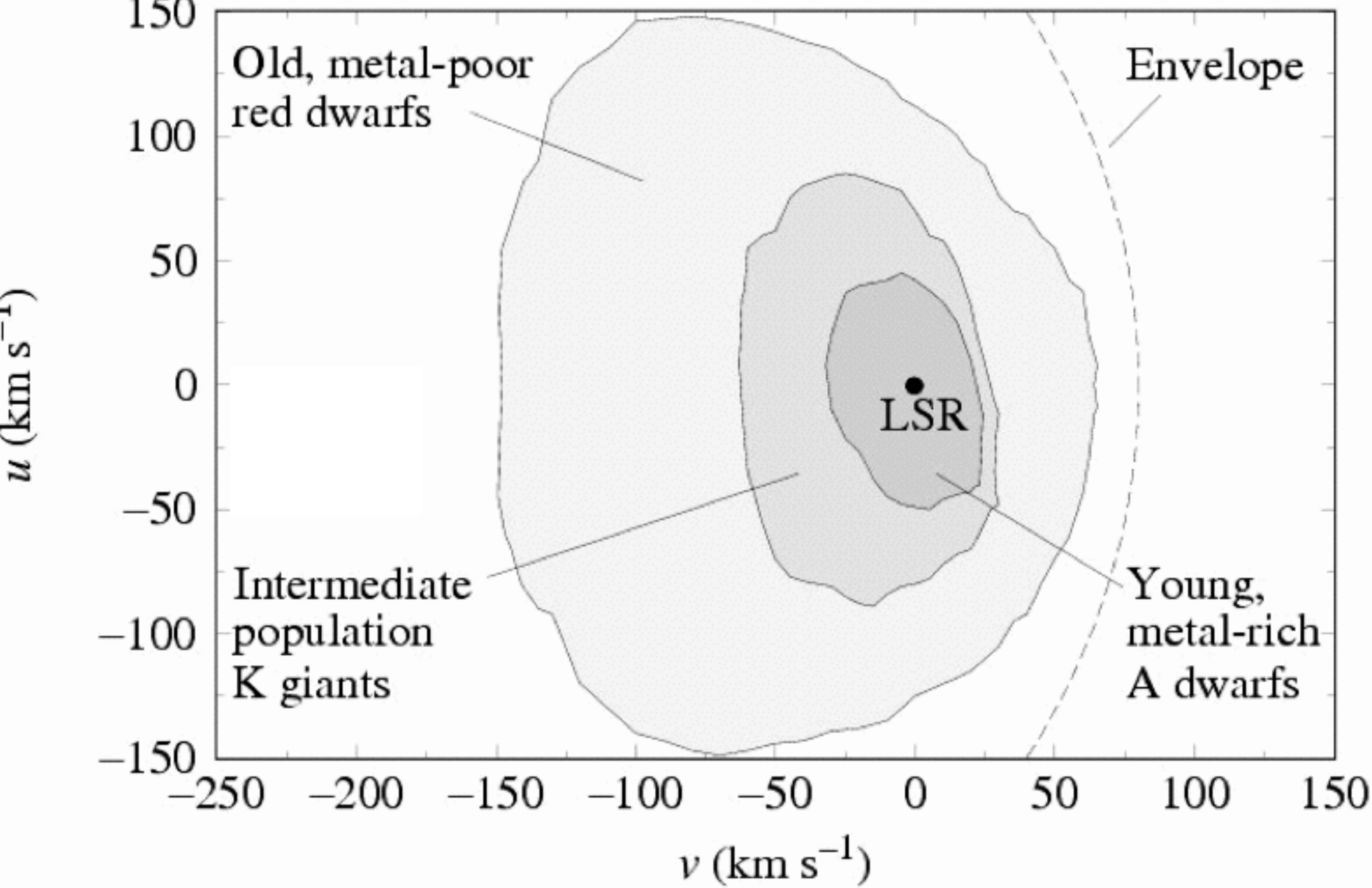

the ‘asymmetric drift’

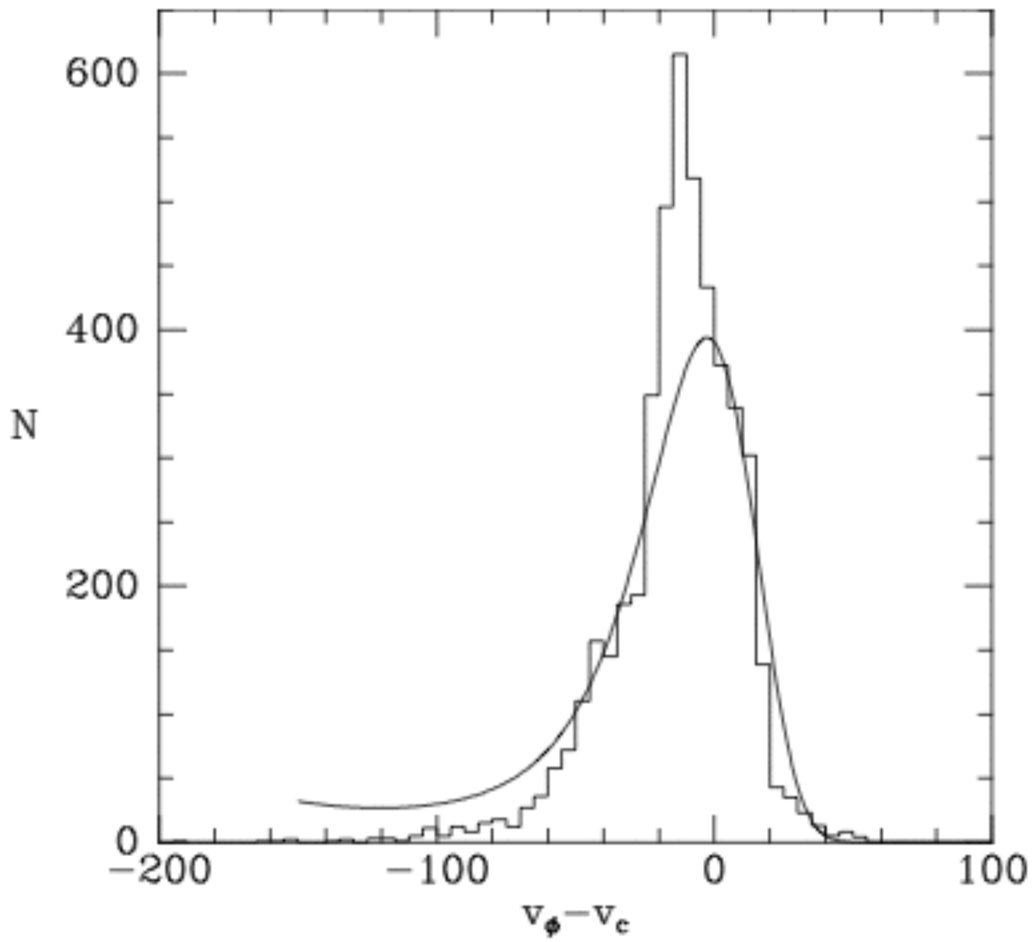

Figure 4.17 The distribution of v_ϕ components of 4787 F and G stars that have space velocities in Nordström et al. (2004). Stars with a high probability of having variable radial velocities are excluded. The smooth curve shows the distribution predicted by the Schwarzschild DF for a population with the same value of $\overline{v_R^2}^{1/2} = 34\,\mathrm{km\,s^{-1}}$.

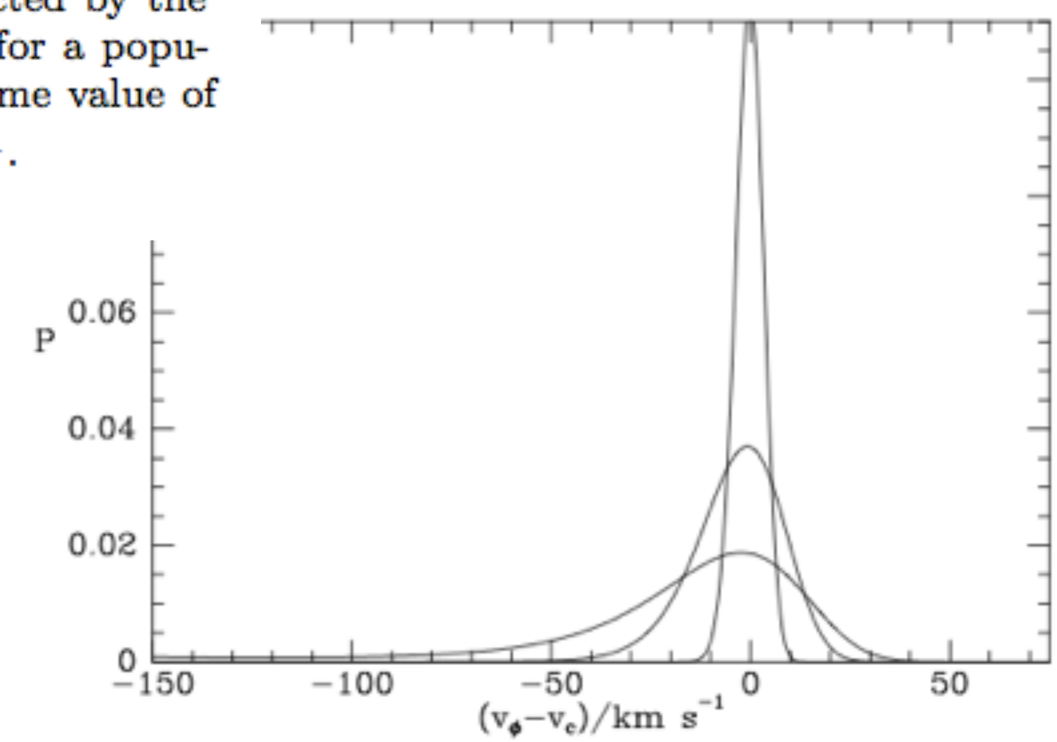

Figure 4.15 Three distributions of azimuthal velocities $\widetilde{v}_\phi$ predicted for stellar populations in the solar neighborhood by the DF (4.156). The circular speed has been assumed to be $v_0 = 220\,\mathrm{km\,s^{-1}}$ at all radii, $\sigma_R(L_z)$ and $\sigma_z(L_z)$ are taken to be proportional to $\exp[-L_z/(2v_0R_\mathrm{d})]$, while $\Sigma = \Sigma_0 \exp(-R/R_\mathrm{d})$, with $R_0/R_\mathrm{d} = 3.2$ (Table 1.2). The values of $\overline{v_R^2}^{1/2}$ for the three populations are 5, 15 and $30\,\mathrm{km\,s^{-1}}$, the largest value producing the widest spread in $\widetilde{v}_\phi$.

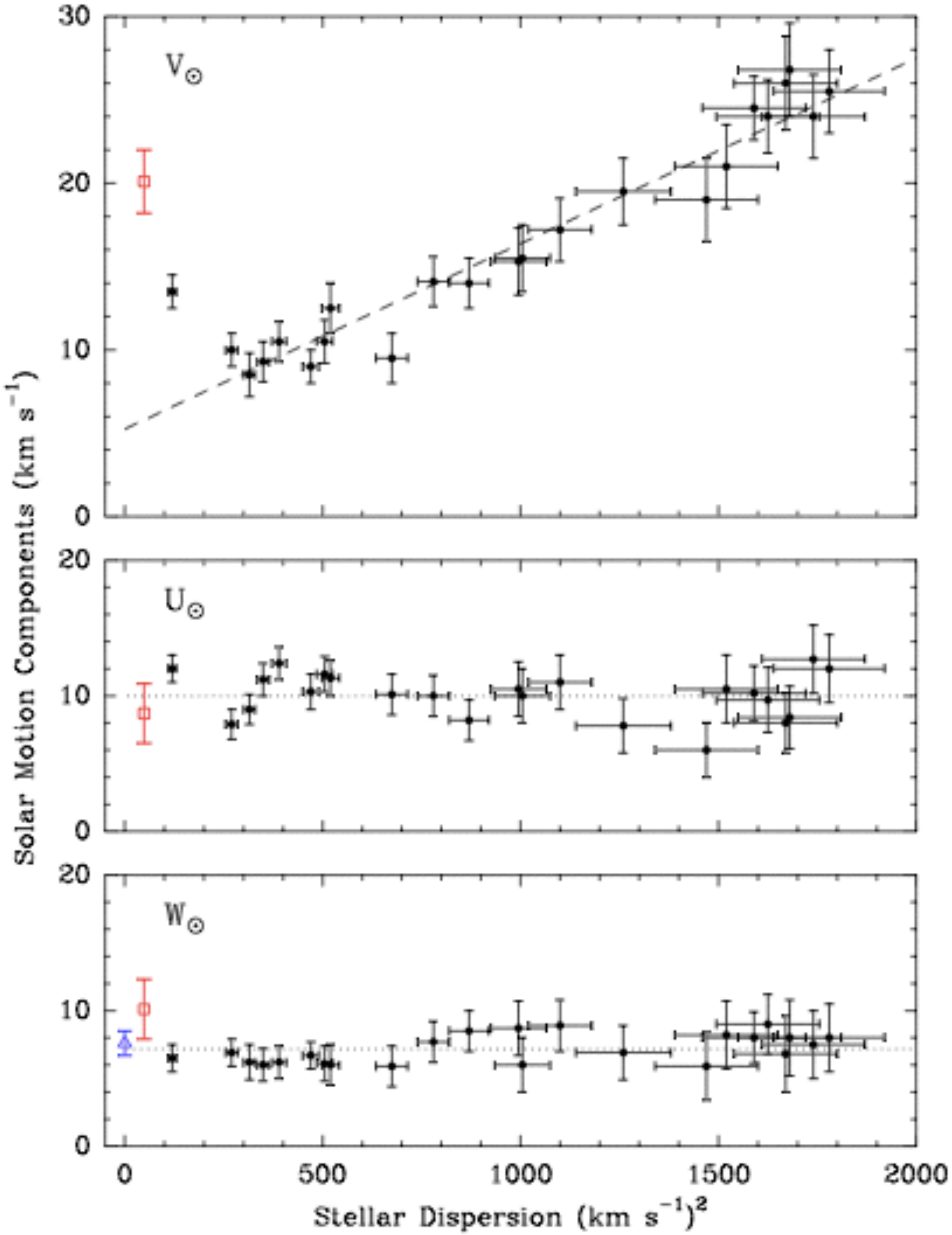

'asymmetric drift',
'rotational lag'
caused by two effects:
1)rotational support
2)density radial gradient

Reid et al '09: study of masers
in star forming regions

Figure 4. Solar motion components determined from *Hipparcos* stars (i.e., the reflex of the average motion of stars) vs. stellar velocity dispersion after Dehnen & Binney (1998). Top Panel: $V_\odot$ is the Solar Motion in the direction of Galactic rotation (i.e., toward $\ell = 90°$). The "asymmetric drift" is shown with the dashed line. Middle Panel: $U_\odot$ is the Solar Motion toward the Galactic center. Bottom Panel: $W_\odot$ is toward the north Galactic pole. Also plotted at 50 (km s^{-1})^2 dispersion with open red squares are solar motion parameters obtained from the parallax and proper motions of star forming regions, and at zero dispersion with an open triangle is the $W_\odot$ component inferred from the proper motion of Sgr A* by Reid & Brunthaler (2004). Note the good agreement of the $U_\odot$ and $W_\odot$ components between *Hipparcos* and this study. The large deviation of the $V_\odot$ component from the asymmetric drift from this study is not indicative of large $V_\odot$ value, but points to a significant deviation from circular orbits for very young stars.

Different determinations of the solar peculiar motion

very young stars: dispersion reflects parent cloud orbit; moving groups...

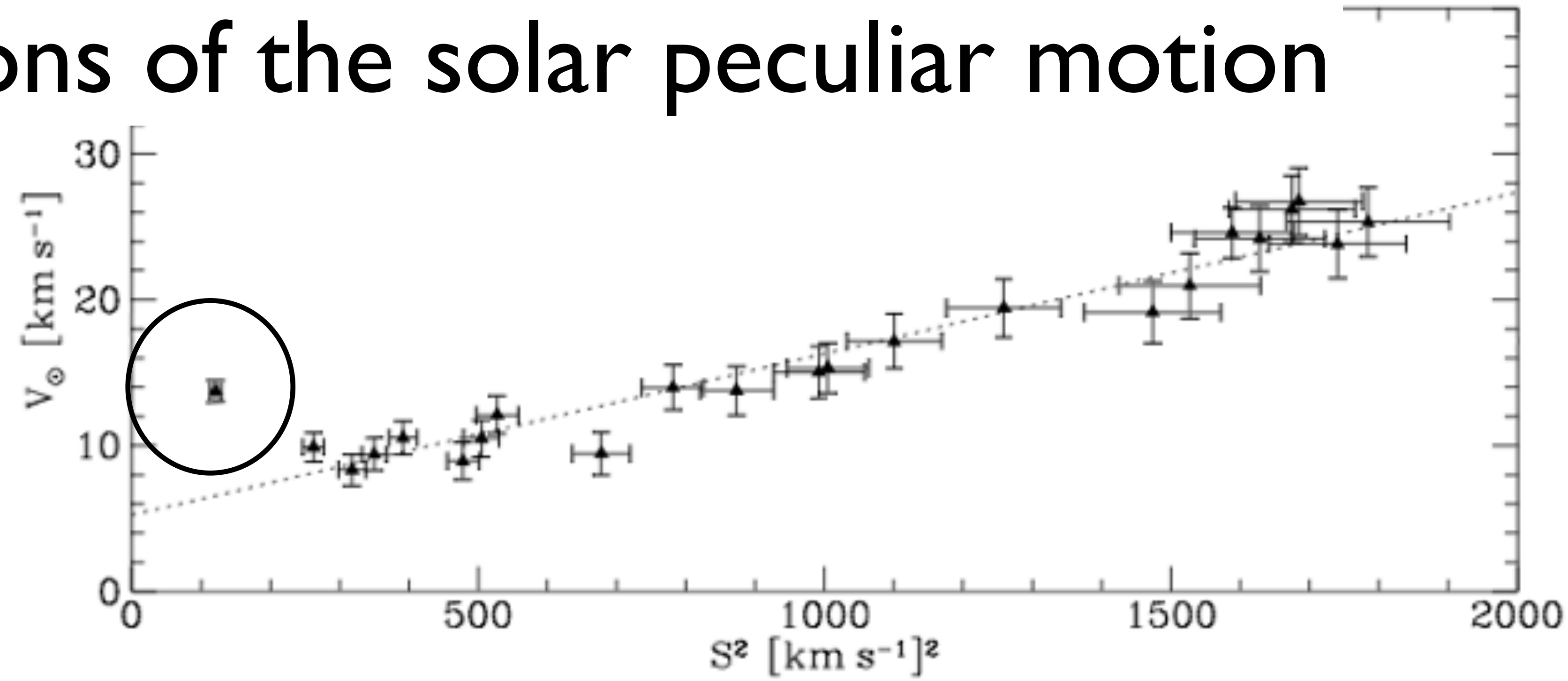

Figure 4.21 The asymmetric drift v_a for different stellar types is a linear function of the random velocity S^2 of each type. The vertical coordinate is actually $v_a + \widetilde{v}_{\phi,\odot}$ where $\widetilde{v}_{\phi,\odot}$ is the azimuthal velocity of the Sun relative to the LSR (after Dehnen & Binney 1998b).

Dehnen & Binney '98
(12,000 Hipparcos stars)

extrapolating back to $S = 0$. Ignoring stars blueward of $B - V = 0$ mag we find

$$U_0 = 10.00 \pm 0.36 \quad (\pm 0.08) \quad \mathrm{km\,s^{-1}},$$
$$V_0 = 5.25 \pm 0.62 \quad (\pm 0.03) \quad \mathrm{km\,s^{-1}}, \qquad (20)$$
$$W_0 = 7.17 \pm 0.38 \quad (\pm 0.09) \quad \mathrm{km\,s^{-1}},$$

Feast & Whitelock '97
(220 Cepheids)

$u_{\odot} = +9.3$ km s^{-1} (add
tions);
$v_{\odot} = +11.2$ km s^{-1} (add
tions);
$w_{\odot} = +7.61 \pm 0.64$ km s

Schonrich, Binney & Dehner '10
'the approach to the determination of V⊙ by DB98... is misleading'
(in fact, very young stars define V_0 perfectly)

U_0=11.1+/-0.7 km/s
V_0=12.2+/-0.5 km/s
w_0=7.3+/-0.4 km/s

Motion relative to the galactic centre can be measured.
= solar peculiar motion + rotation curve

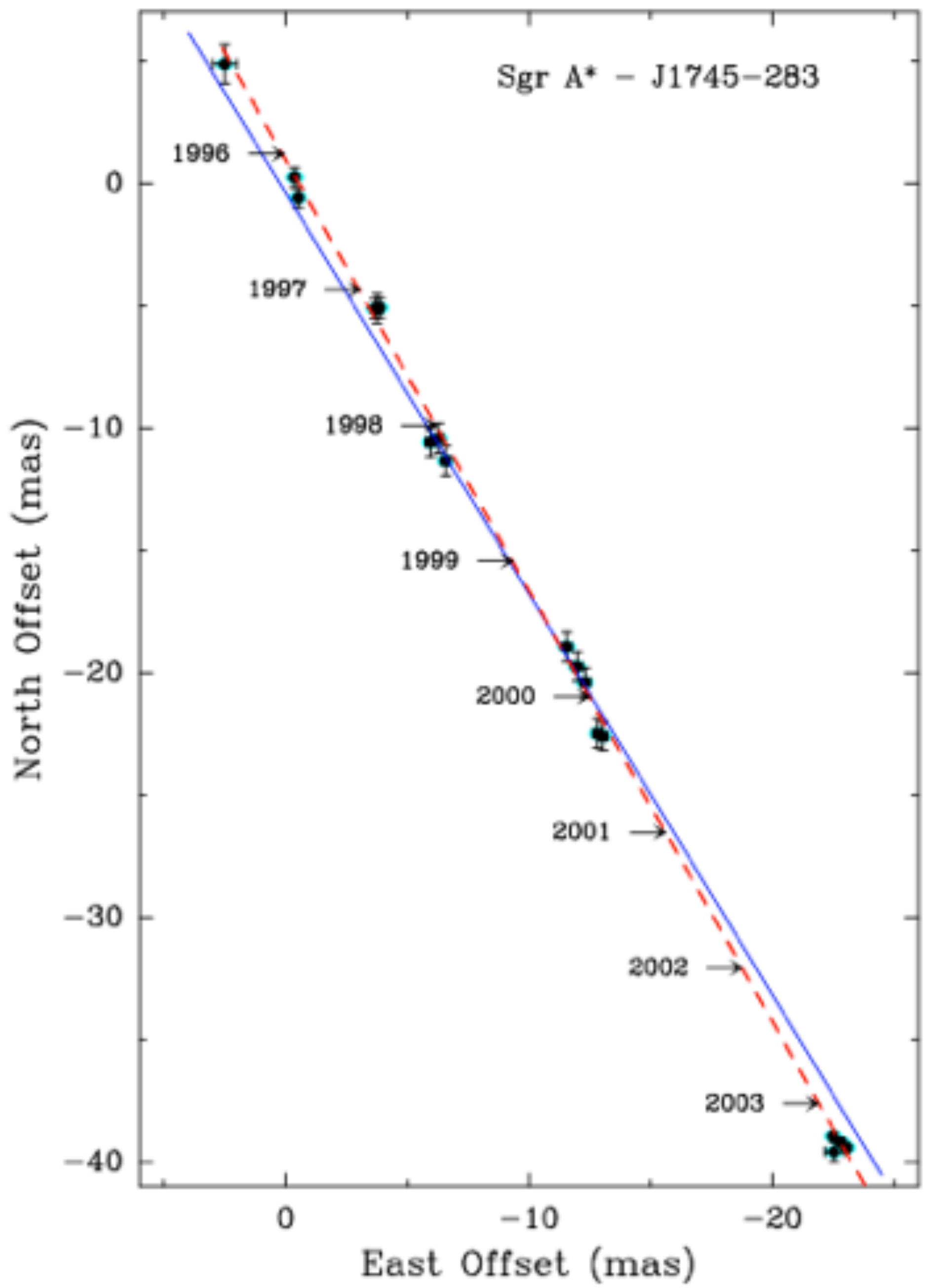

Fig. 1.— Position residuals of Sgr A* relative to J1745–283 on the plane of the sky. Each measurement is indicated with an ellipse, approximating the apparent scatter-broadened size of Sgr A* at 43 GHz and 1σ error bars, which include estimates of systematic uncertainties. The dashed line is the variance-weighted best-fit proper motion, and the solid line gives the orientation of the Galactic plane, which is tilted by 31.40° east of north in J2000 coordinates (see Appendix).

So rotation curve subject to bias in solar motion

More twists

Bovy et al '12, APOGEE data
v0 = 26 +/- 3 km/s; Milky Way mass down.

Table 2
Results for Galactic Parameters and Tracer Properties

Parameter	Flat Rotation Curve	Power-law $V_c(R) = V_c(R_0)\ (R/R_0)^{\beta}$
$V_c(R_0)$ (km s^{-1})	218 ± 6	218^{+4}_{-19}
β	...	$0.01^{+0.01}$
$dV_c/dR\,(R_0)$ (km s^{-1} kpc^{-1})	...	
A (km s^{-1} kpc^{-1})	$13.5^{+0.2}_{-1.7}$	
B (km s^{-1} kpc^{-1})	$-13.5^{+1.7}_{-0.2}$	
$(B^2 - A^2)/(2\pi G)$ ($M_\odot$ pc^{-3})	...	
Ω_0 (km s^{-1} kpc^{-1})	$27.0^{+0.3}_{-3.5}$	
R_0 (kpc)	$8.1^{+1.2}_{-0.1}$	
$V_{R,\odot}$ (km s^{-1})	$-10.5^{+0.5}_{-0.8}$	
$V_{\phi,\odot}$ (km s^{-1})	242^{+10}_{-3}	
$V_{\phi,\odot} - V_c$ (km s^{-1})	$23.9^{+5.1}_{-0.5}$	
$\mu_{\mathrm{Sgr\ A}^*}$ (mas yr^{-1})	$6.32^{+0.07}_{-0.70}$	$6.36^{+[illegible]}_{-0.86}$
$\sigma_R(R_0)$ (km s^{-1})	$31.4^{+0.1}_{-3.2}$	$32.2^{+0.2}_{-2.6}$
R_0/h_σ	$0.03^{+0.01}_{-0.27}$	$0.06^{+0.01}_{-0.17}$
$X^2 \equiv \sigma_\phi^2/\sigma_R^2$	$0.70^{+0.30}_{-0.01}$	$0.64^{+0.18}_{-0.02}$

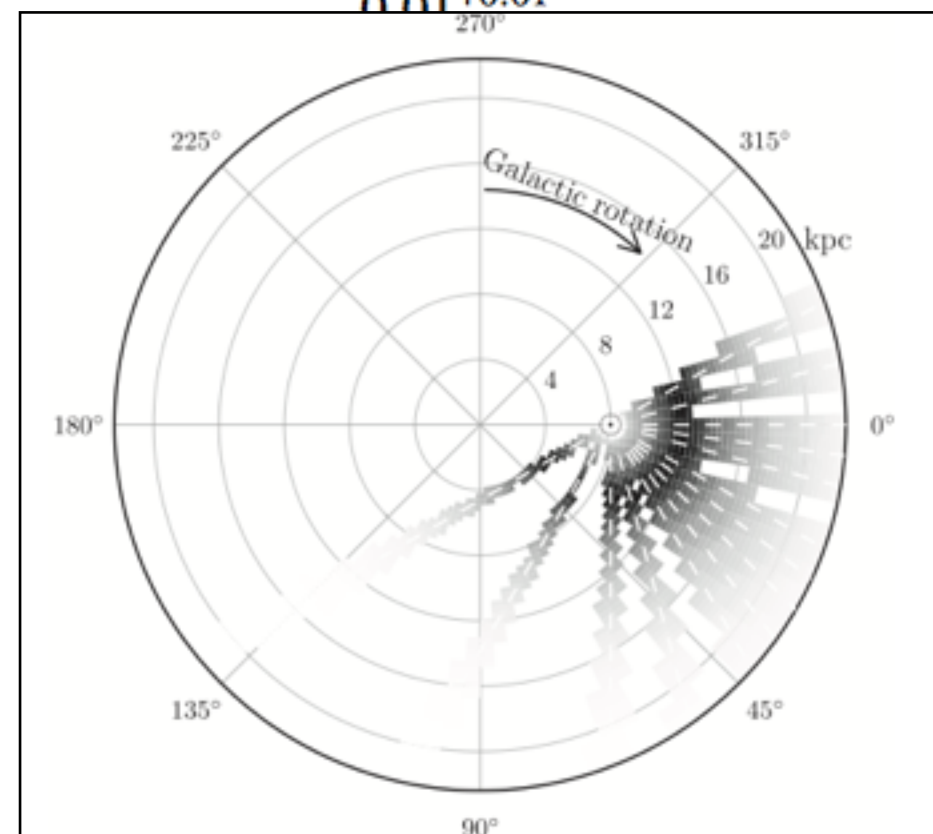

2nd application: velocity dispersion

$$\sigma_i^2 =< (v_i - \bar{v}_i)^2 >$$

velocity dispersion of stars increases with their mean ages

evidence for heating due to GMC or spiral arms/bars?

ratios of σ_R/σ_z, σ_R/σ_ϕ, cross-terms etc., constrain heating mechanisms

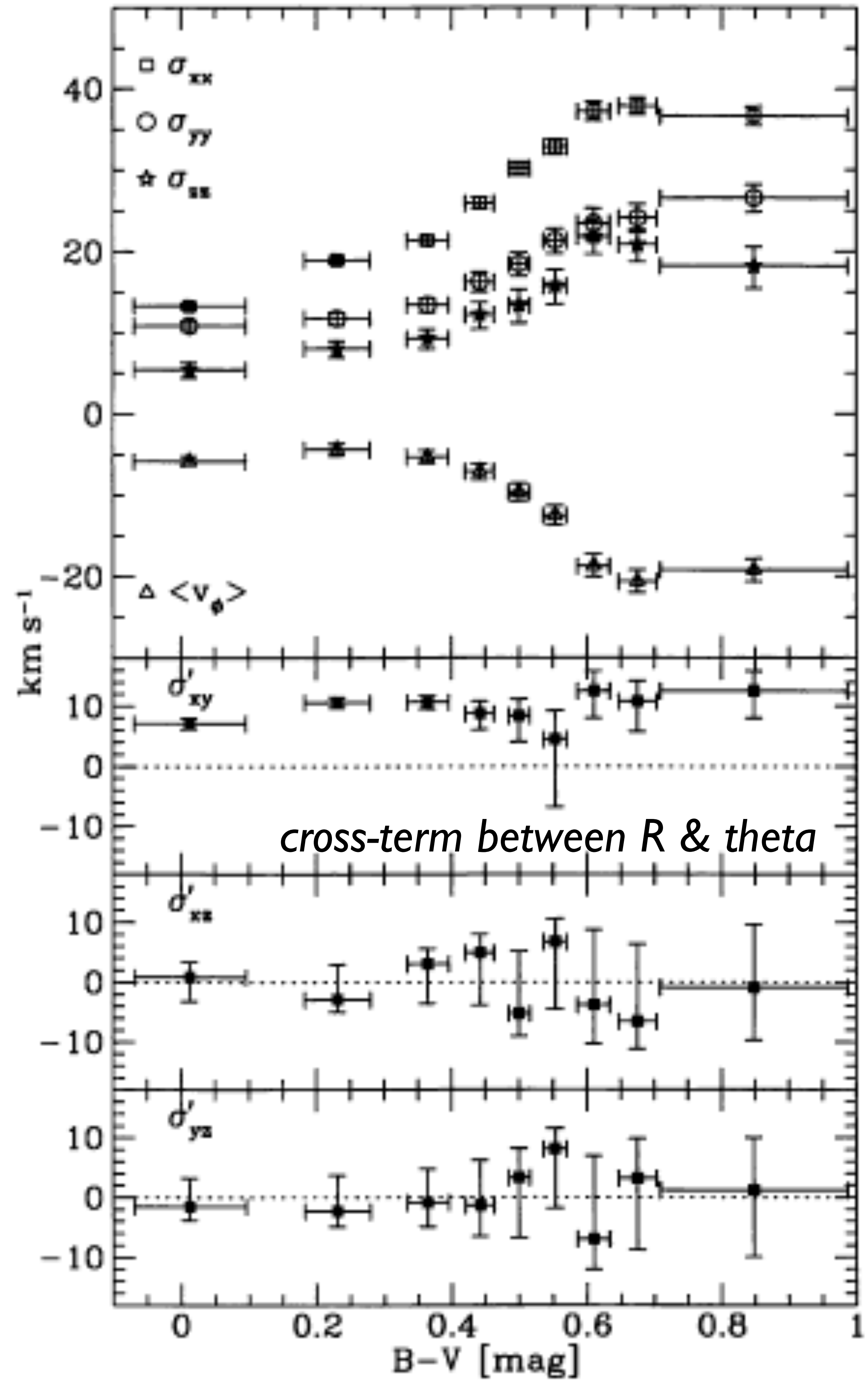

Figure 5. Velocity dispersions for stars in different colour bins. The top panel shows the mean rotation velocity (negative values imply lagging with respect to the LSR) and the three main velocity dispersions. In the three bottom panels $\sigma'_{ij} = \mathrm{sign}(\sigma^2_{ij})\,|\sigma^2_{ij}|^{1/2}$ is plotted for the mixed components of the tensor σ^2_{ij}.

for stars near the mid-plane (Hipparcos data, $|z| < 100$pc), Dehnen & Binney '98 ratio of σ_R/σ_ϕ also measures the gravitational potential

stars with the same guiding centres:

ratio of σ_R/σ_ϕ also measures the gravitational potential

$$x(t) = X\cos(\kappa t + \alpha),\qquad y = -\gamma X \sin(\kappa t+\alpha) \equiv -Y\sin(\kappa t + \alpha).$$

$$\boxed{\gamma \equiv \frac{2\Omega_g}{\kappa}}$$

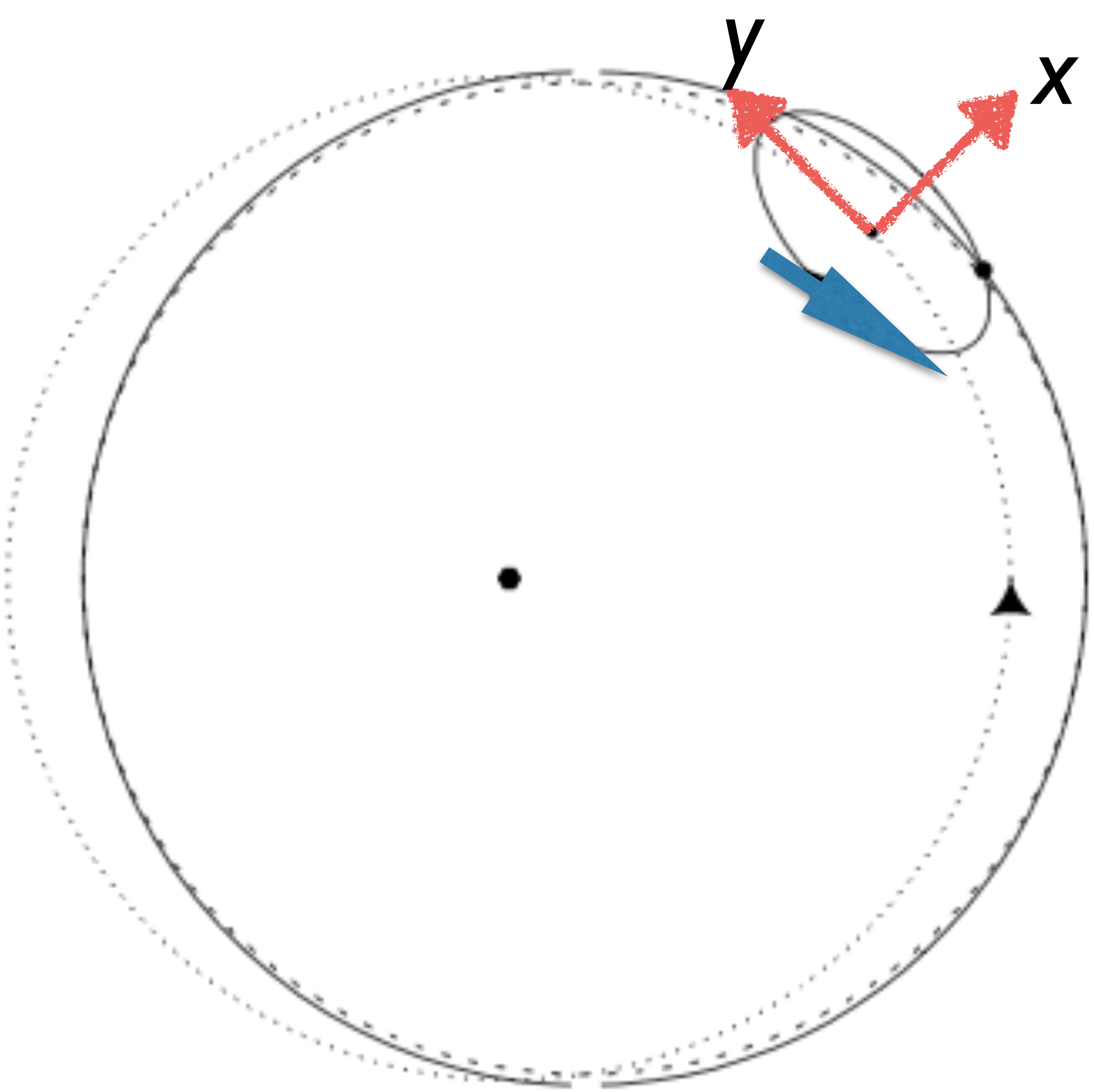

Keplerian: X/Y = 0.5
Harmonic: X/Y = 1
Galatic: X/Y ~ 0.7

$$\dot{x}^2 \equiv \sigma_R^2 = \tfrac{1}{2}\kappa^2 X^2$$
$$\dot{y}^2 \equiv \sigma_\theta^2 = \tfrac{1}{2}\kappa^2 Y^2$$

for stars with the same guiding center orbits

Practical problem: in the solar neighbourhood, stars have different guiding centres

Averaging over the phases α of stars near the Sun, we find

$$\overline{[v_\phi - v_c(R_0)]^2} = \frac{\kappa^2 X^2}{2\gamma^2} = 2B^2X^2. \qquad (3.98)$$

Similarly, we may neglect the dependence of κ on R_g to obtain with equation (3.84)

$$\overline{v_R^2} = \tfrac{1}{2}\kappa^2 X^2 = -2B(A-B)X^2. \qquad (3.99)$$

Taking the ratio of the last two equations we have

$$\boxed{\frac{\overline{[v_\phi - v_c(R_0)]^2}}{\overline{v_R^2}} \simeq \frac{-B}{A-B} = -\frac{B}{\Omega_0} = \frac{\kappa_0^2}{4\Omega_0^2}} = \gamma^{-2} \simeq 0.46. \qquad (3.100)$$

But stars also have different amplitudes (X is not a constant)

a distribution of X; centroid and dispersion depends on stellar ages; however…

392 *W. Dehnen and J. J. Binney*

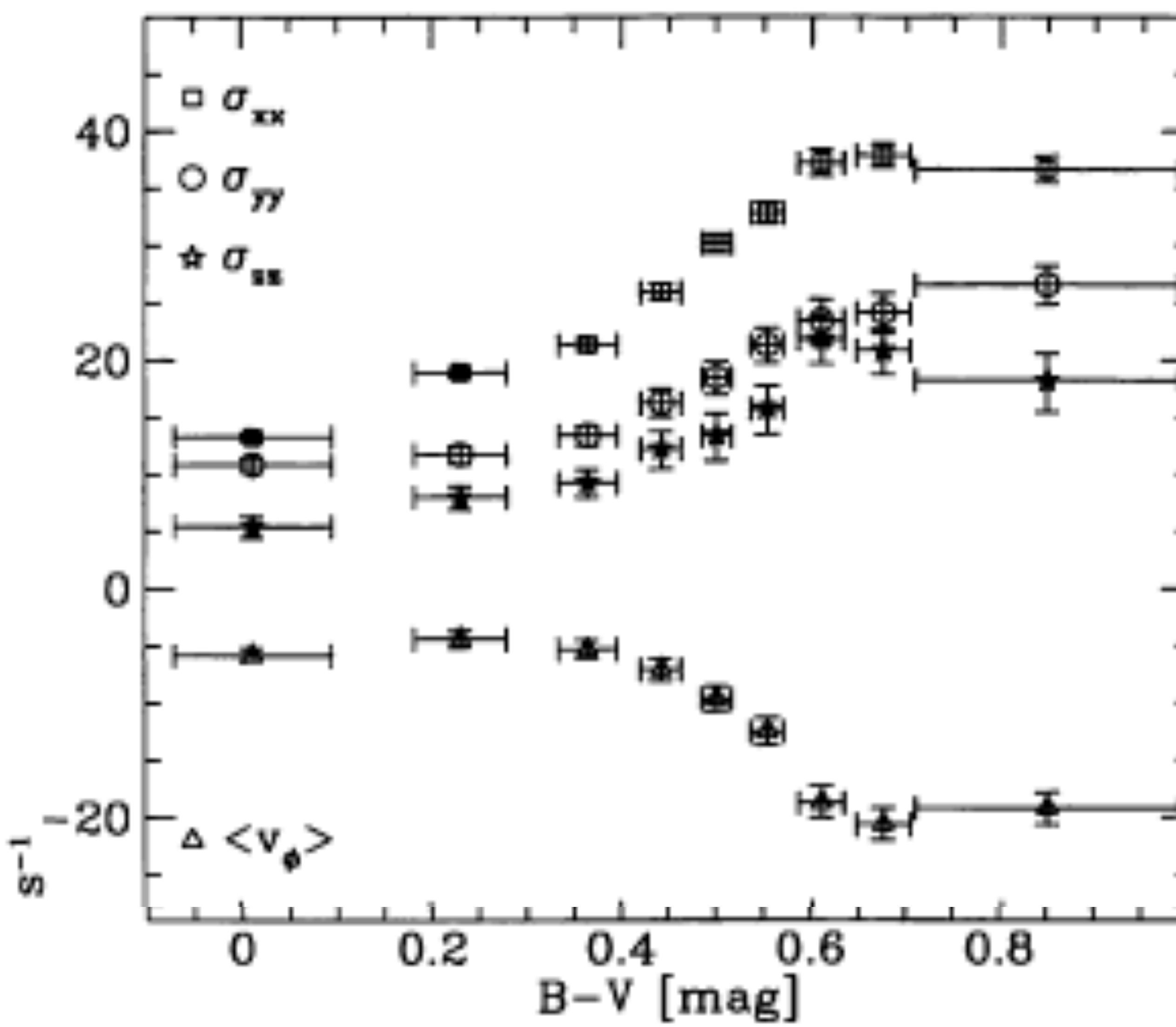

Figure 5. Velocity dispersions for stars in different colour bins. The top panel shows the mean rotation velocity (negative values imply lagging with respect to the LSR) and the three main velocity dispersions. In the three bottom panels $\sigma'_{ij} = \mathrm{sign}(\sigma^2_{ij})\,|\sigma^2_{ij}|^{1/2}$ is plotted for the mixed components of the tensor σ^2_{ij}.

we can measure κ/Ω, what about ν/Ω?

$$4\pi G\rho = \frac{1}{R}\frac{\partial}{\partial R}\left(R\frac{\partial\Phi}{\partial R}\right) + \frac{\partial^2\Phi}{\partial z^2}$$
$$\simeq \frac{1}{R}\frac{\mathrm{d}v_c^2}{\mathrm{d}R} + \nu^2, \quad \sim \nu^2$$

- *measure* ν *—> measure local matter density*
- *and since we are embedded in the disk…*
- *how do we go about this task?*
- *ratio of* σ_z/σ_ϕ *?*

Table 1.1 Inventory of the solar neighborhood

component	volume density ($\mathcal{M}_\odot\,\mathrm{pc}^{-3}$)	surface density ($\mathcal{M}_\odot\,\mathrm{pc}^{-2}$)	luminosity density ($L_\odot\,\mathrm{pc}^{-3}$)	surface brightness ($L_\odot\,\mathrm{pc}^{-2}$)
visible stars	0.033	29	0.05	29
stellar remnants	0.006	5	0	0
brown dwarfs	0.002	2	0	0
ISM	0.050	13	0	0
total	0.09 ± 0.01	49 ± 6	0.05	29
dynamical	0.10 ± 0.01	74 ± 6	–	–

NOTES: Volume and luminosity densities are measured in the Galactic midplane and surface density is the total within ± 1.1 kpc of the plane. Luminosity density and surface brightness are given in the R band. Dynamical estimates are from §4.9.3. Most other entries are taken from Flynn et al. (2006).

Spectral Energy Distribution of a galaxy

galaxy = Σ star light = $\int L(m)\, dN/dm\, dm$

In main sequence, $L \propto m^4$

Stars in the Solar Neighbourhood (mostly disk stars + some halo stars)

Number density of stars in the local neighbourhood

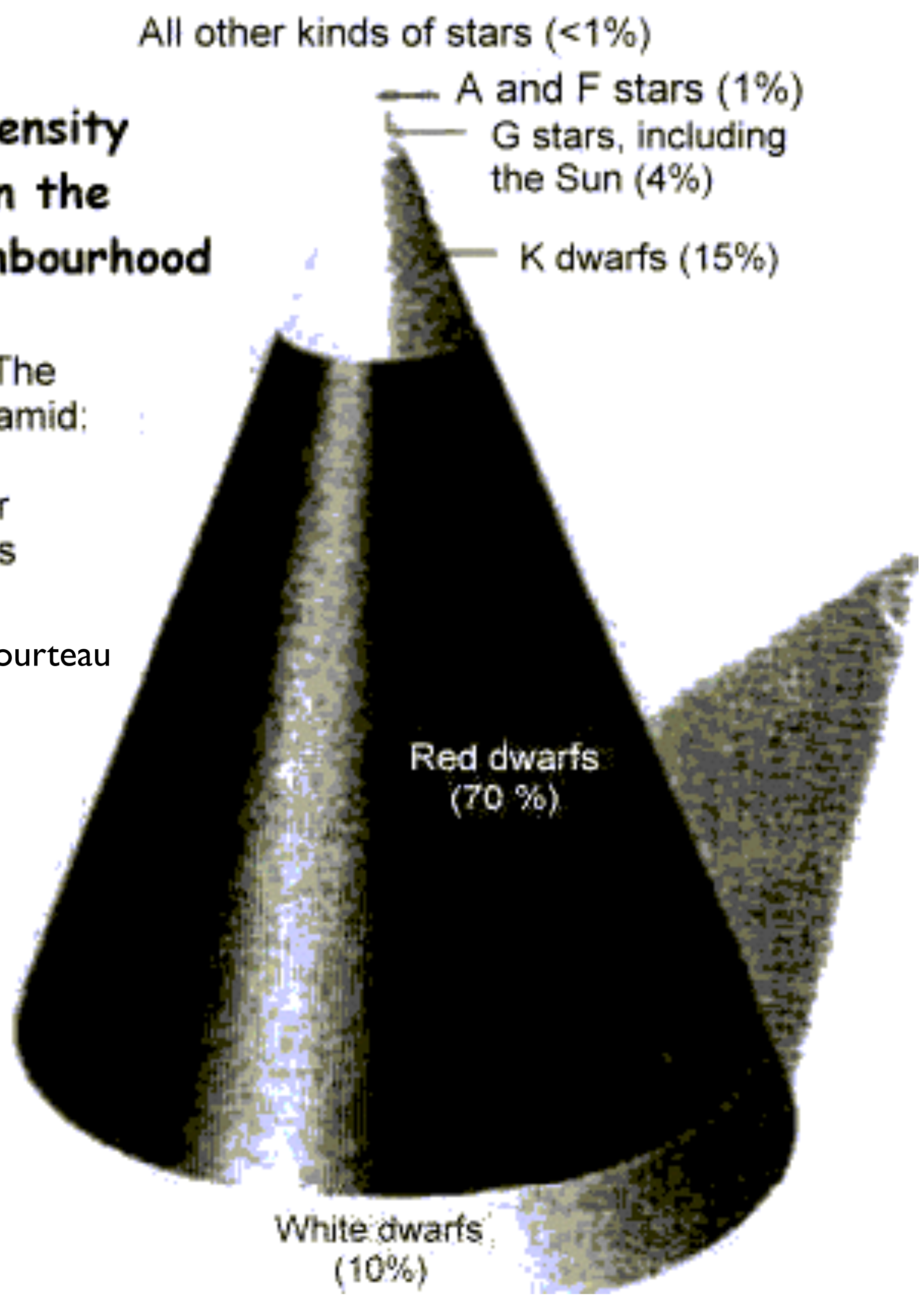

Figure 4 The stellar pyramid: dim stars outnumber bright ones

courtesy of S. Courteau

Melchior et al '07

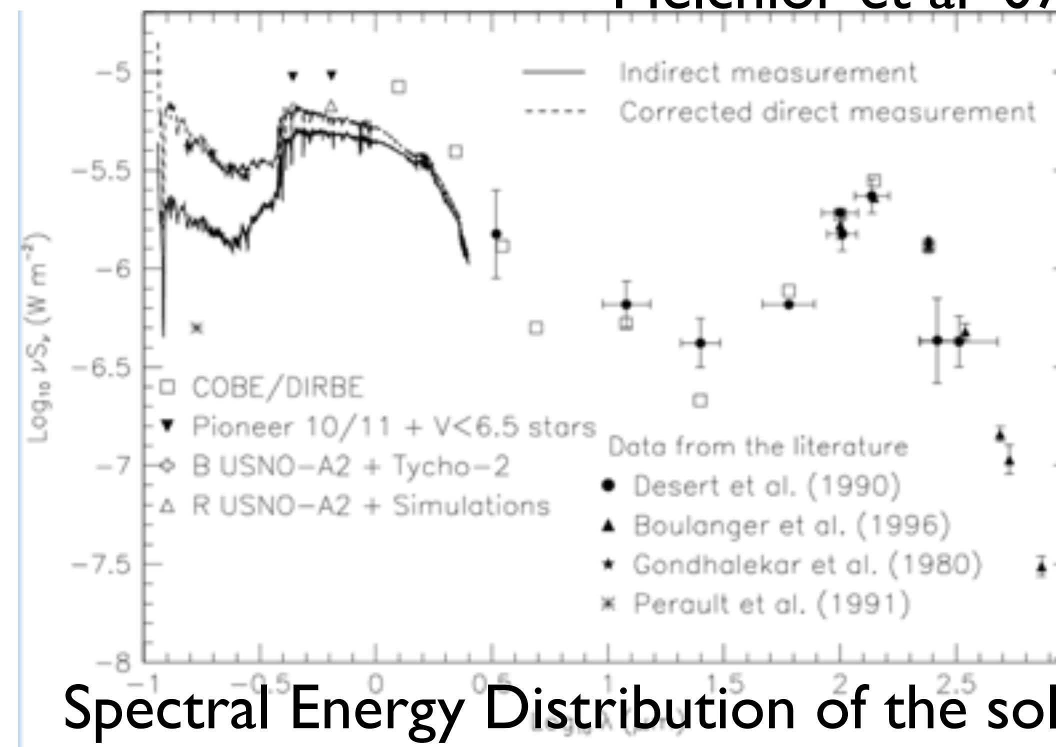

Spectral Energy Distribution of the solar neighbourhood

Melchior et al '07

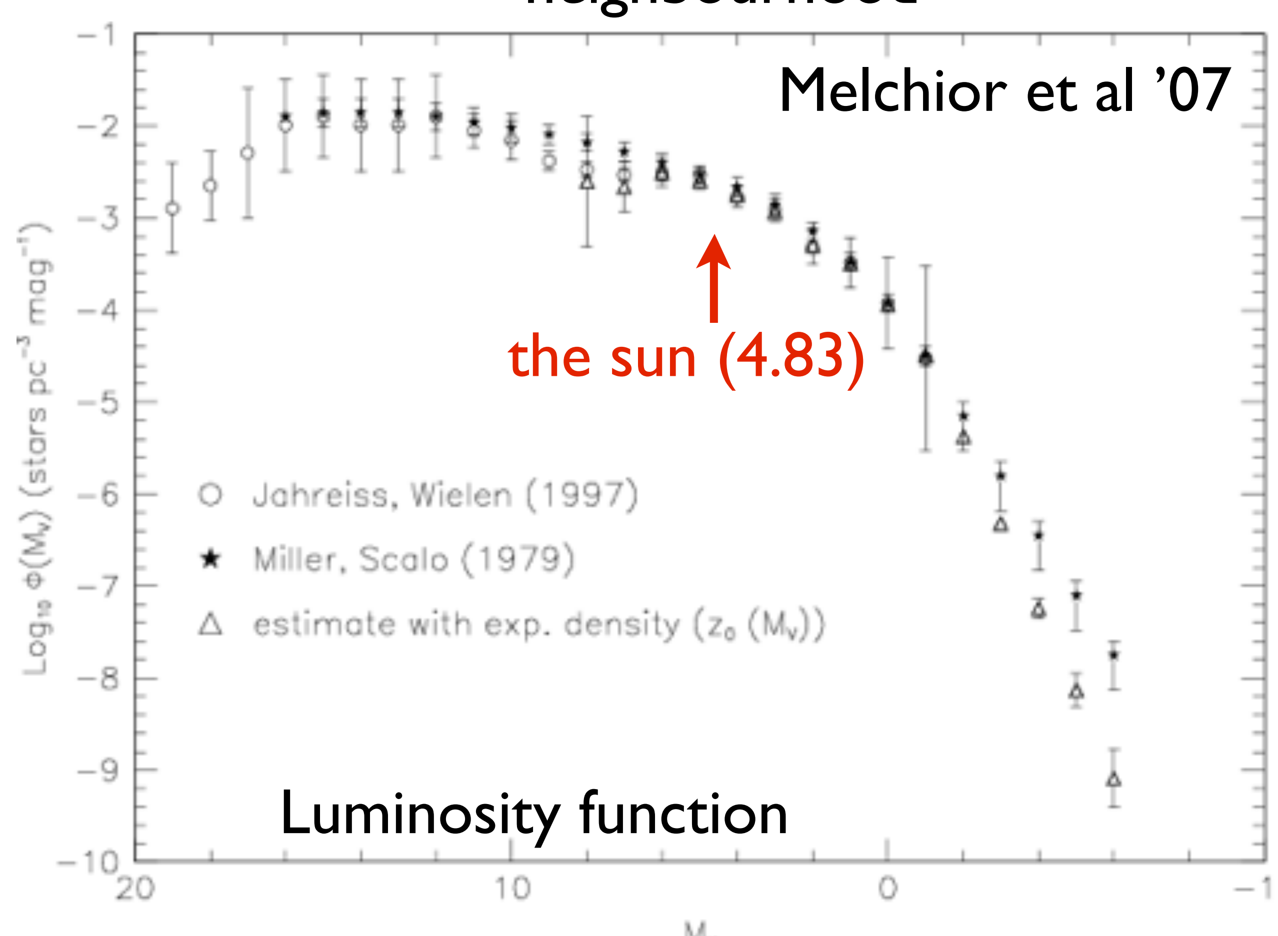

Luminosity function

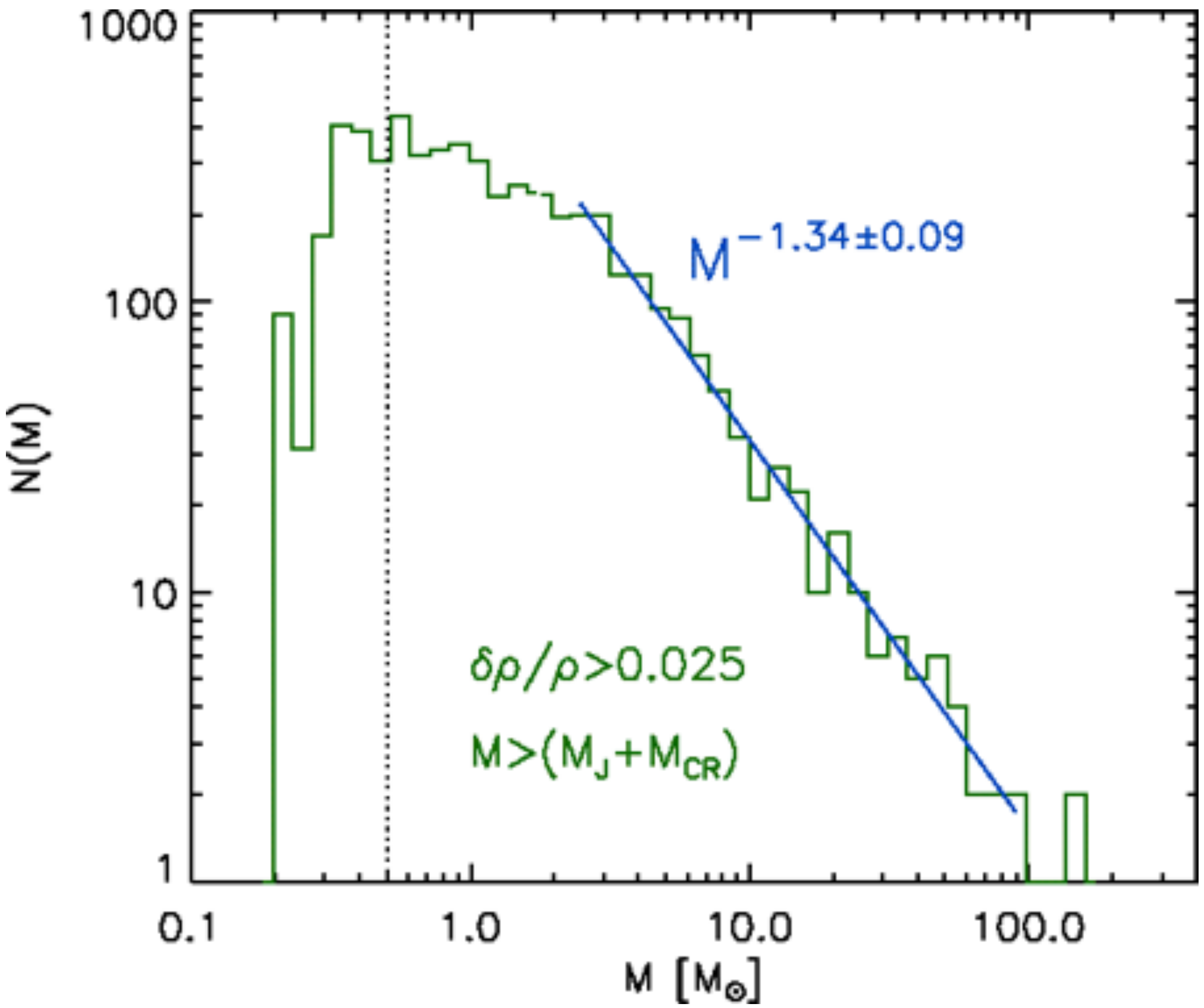

Initial mass function in the solar neighborhood

$dN = \xi(m)\ d \log m = n(m)dm$

star counts= initial mass function
convolve with
star formation rate
convolve with
stellar evolution

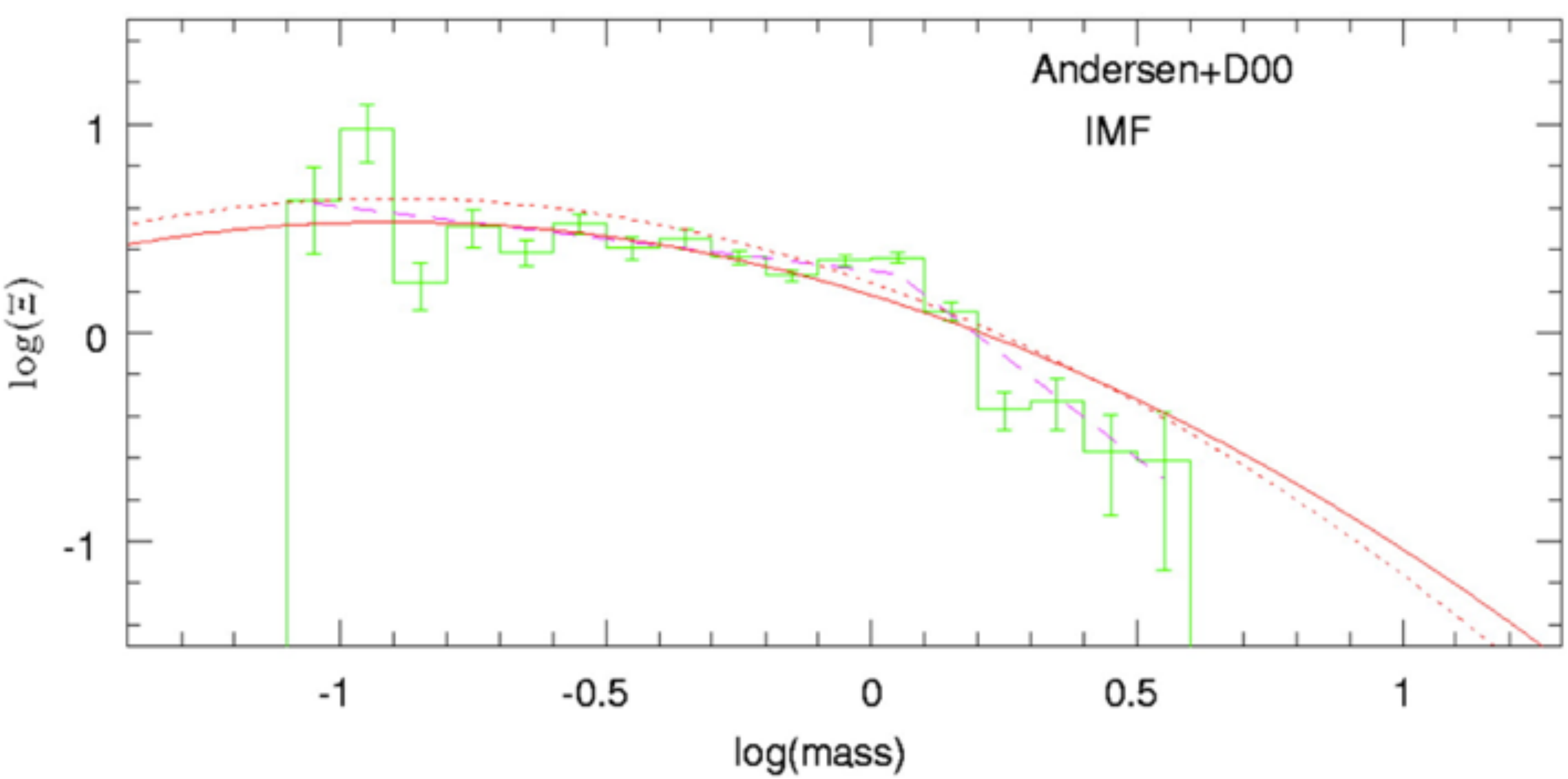

Mass function in the solar neighborhood

$dN = \xi(m)\ d \log m = n(m)dm$

Bruzual & Charlot '93 "Spectral evolution of stellar populations using isochrone synthesis"

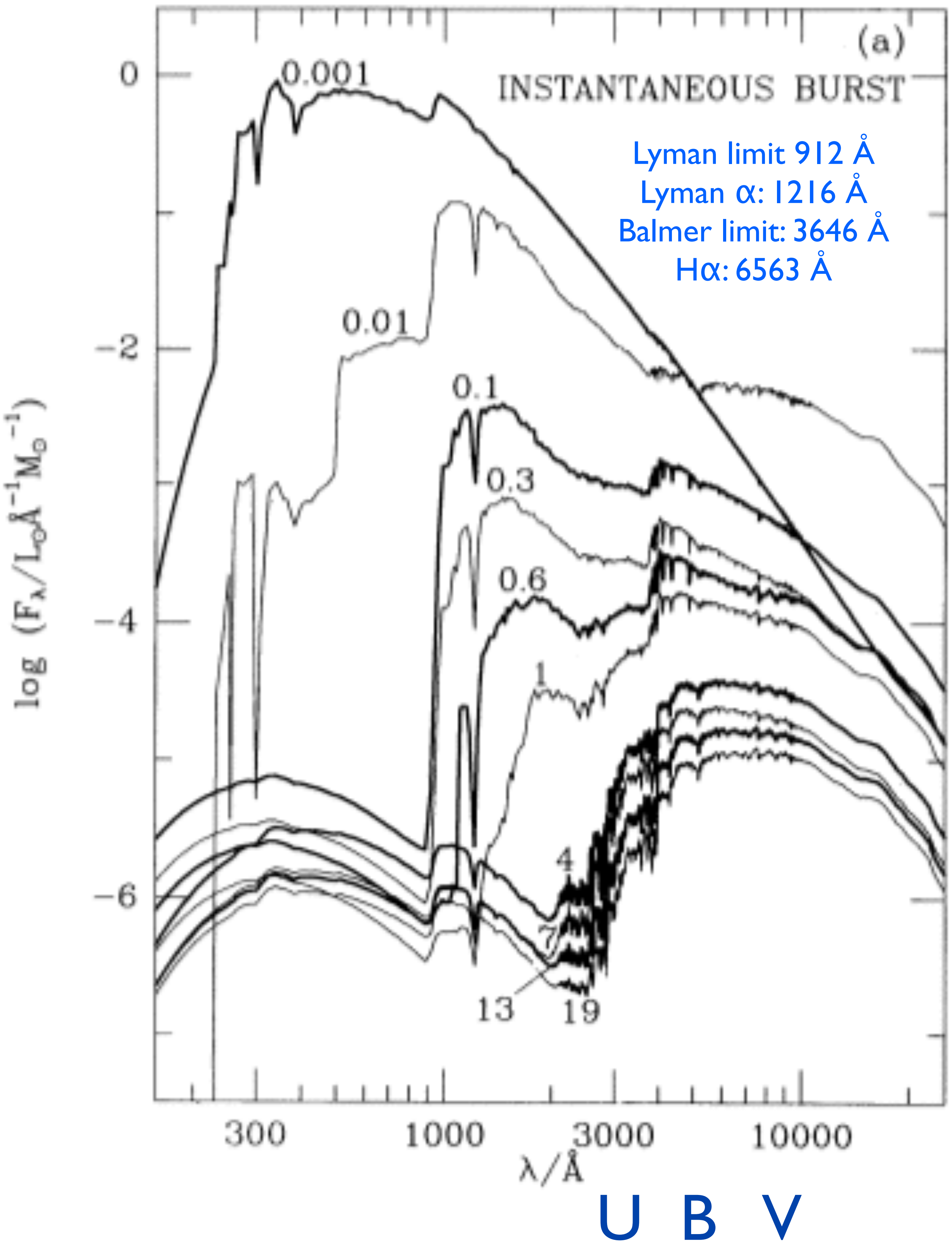

blue vs. red galaxies
(red means death)

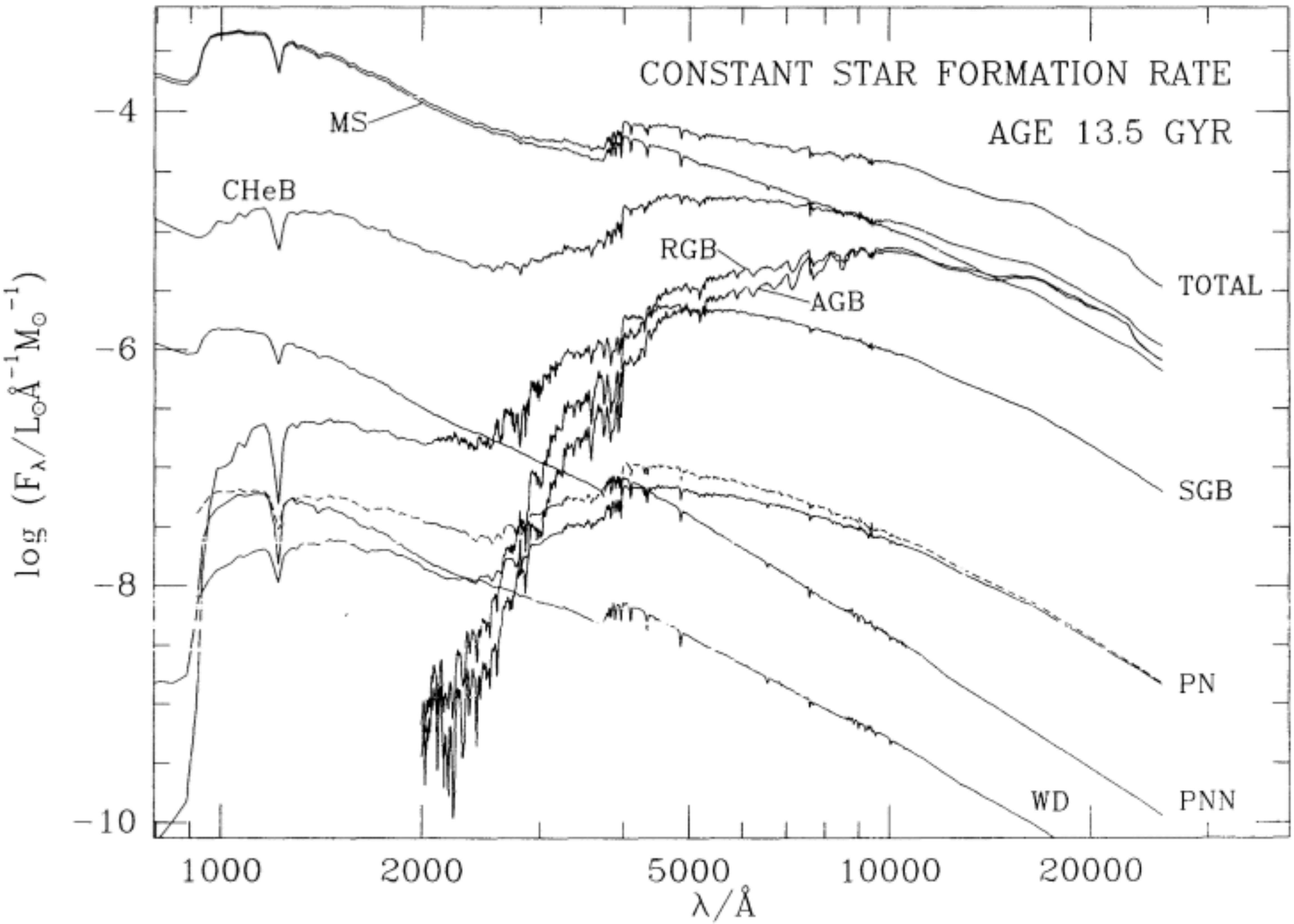

FIG. 10.—Same as Fig. 9 for a stellar population with constant star formation rate at age 13.5 Gyr

What is the SED of an elliptical galaxy?

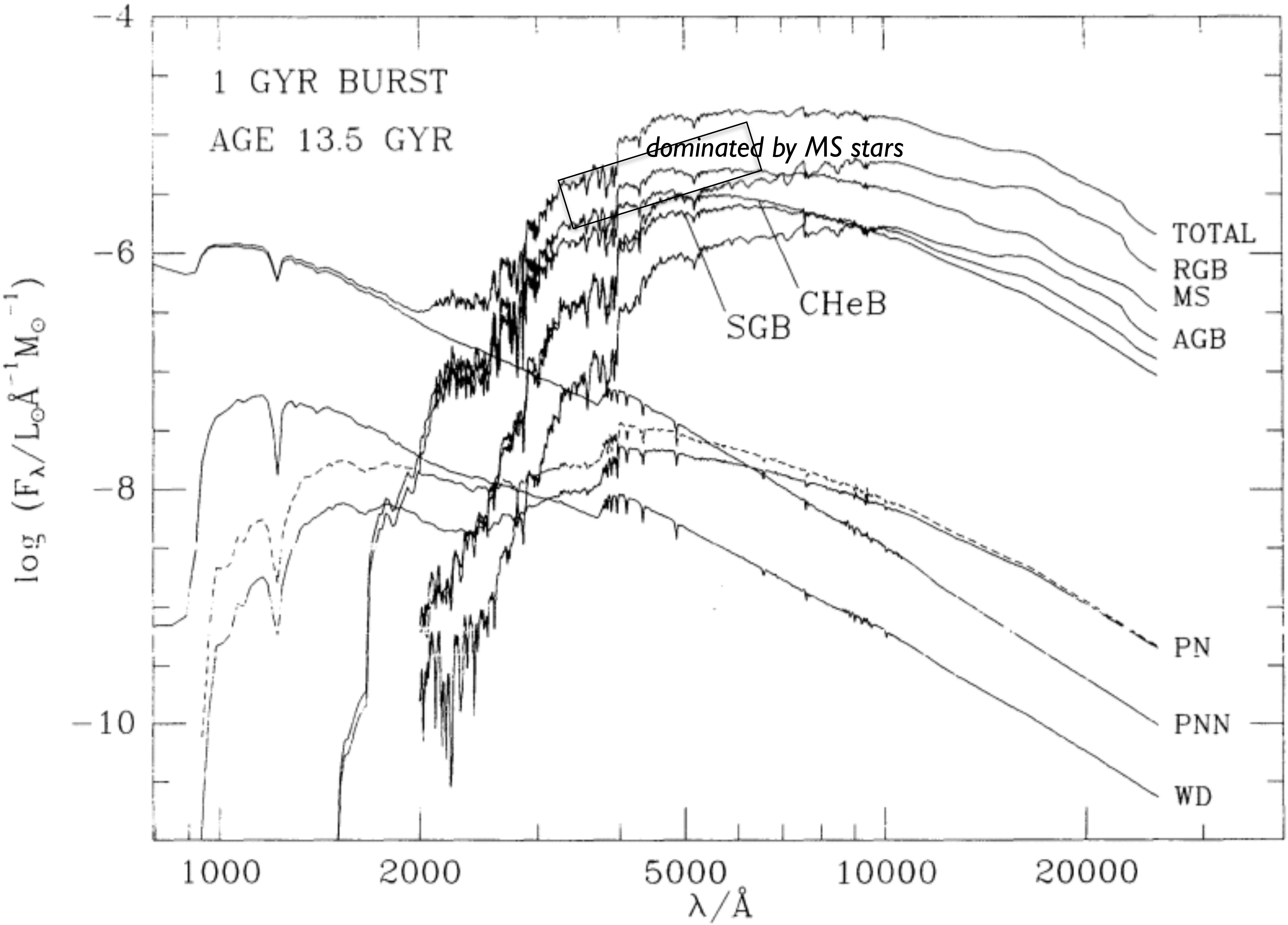

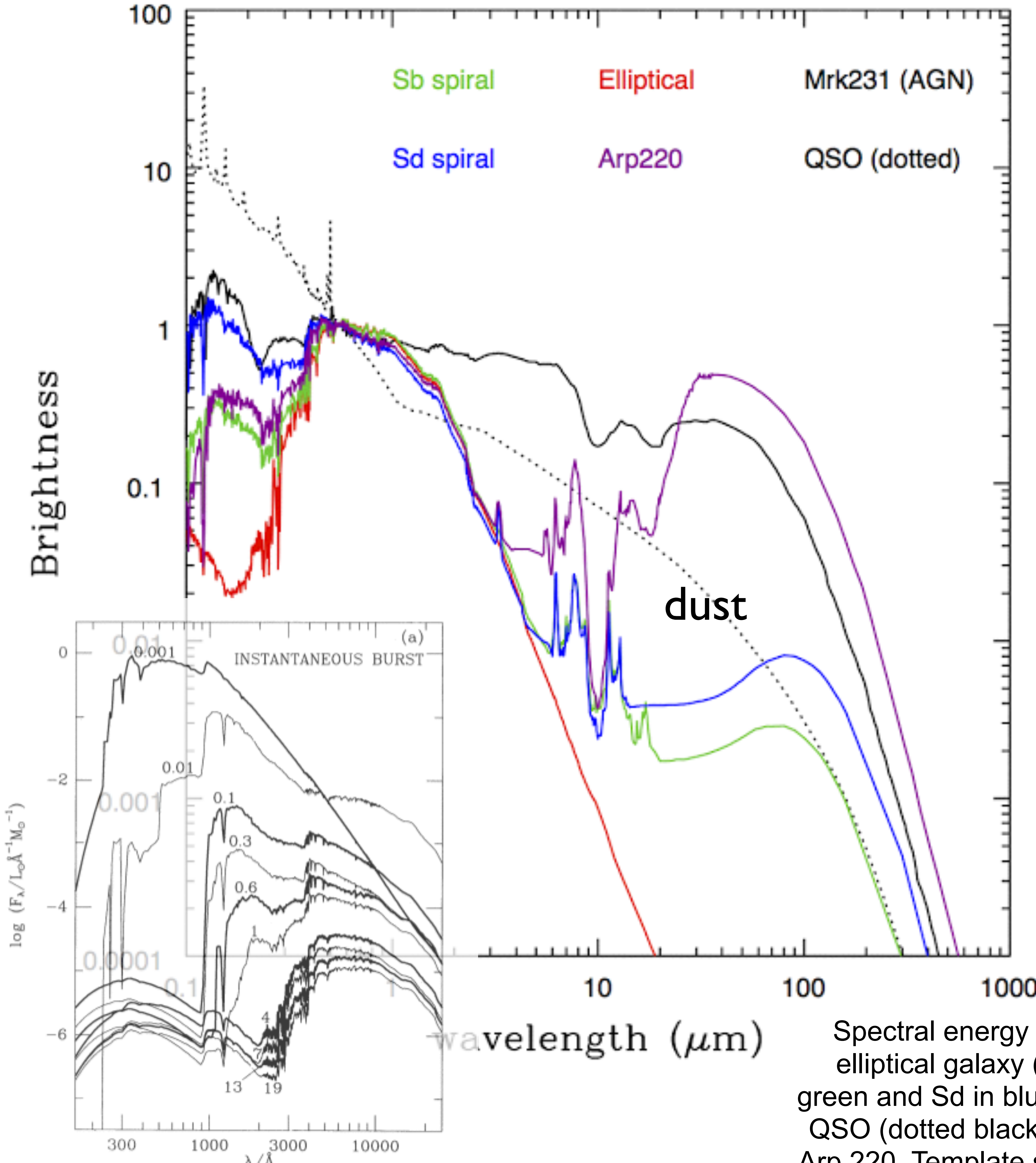

Infrared
gives new information

Spectral energy distributions for typical galaxies - an old elliptical galaxy (red), two types of spiral galaxies (Sb in green and Sd in blue), an AGN (Markarian 231, solid black), a QSO (dotted black), and a merging and star-bursting galaxy Arp 220. Template spectra are taken from Polletta et al. 2007.

Back to the solar neighbourhood

Local Velocity Dispersions — spectral types

u: R-direction, x
v: theta-direction, y

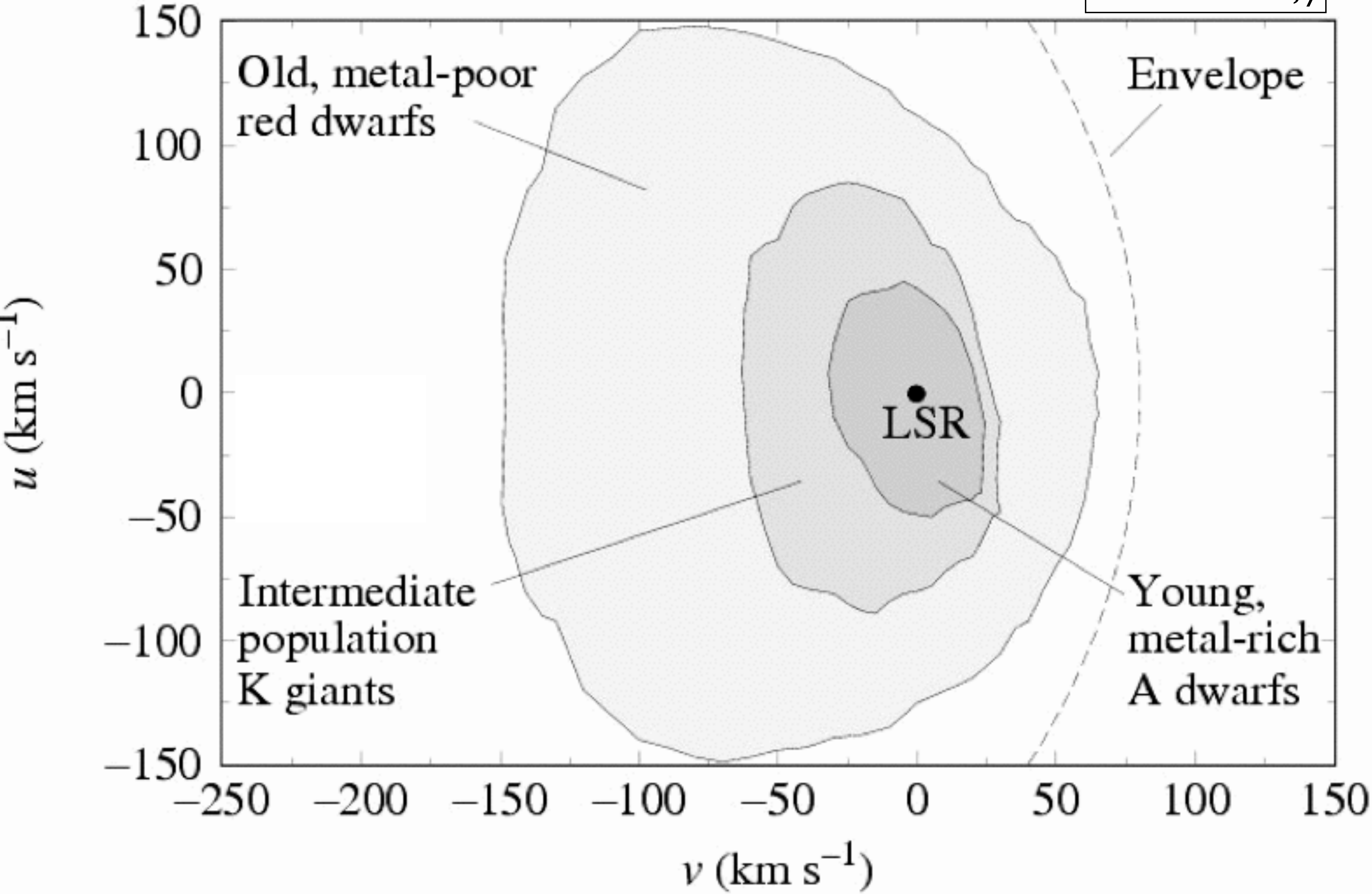

Local Velocity Dispersions — stellar age

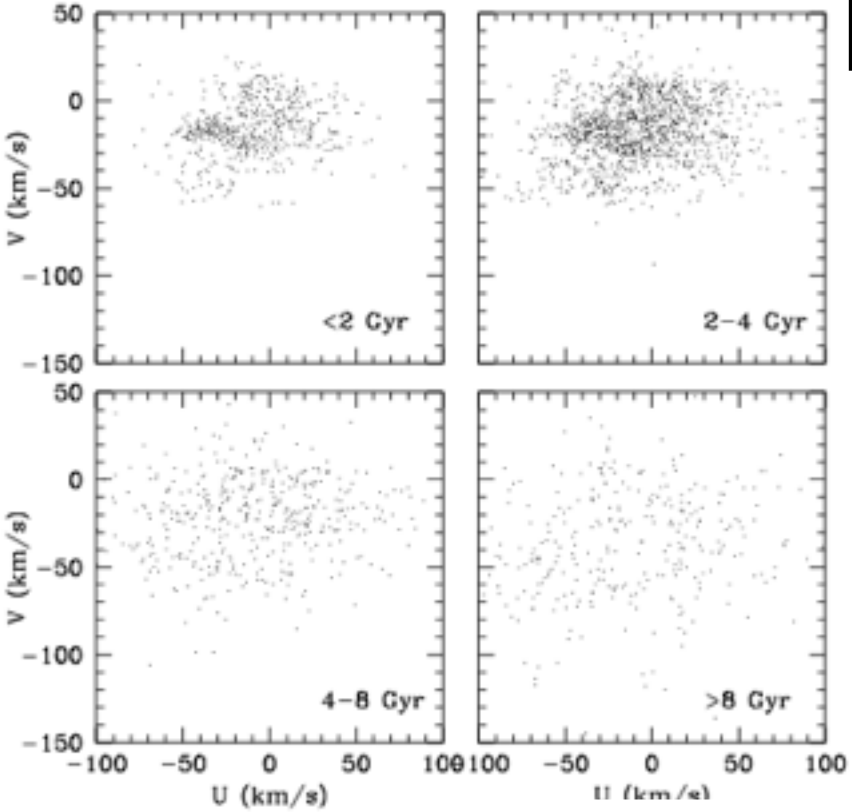

Fig. 6. $U - V$ diagram for the subsan
age groups.

Geneva-Copenhagen survey results
~14,000 F & G dwarfs

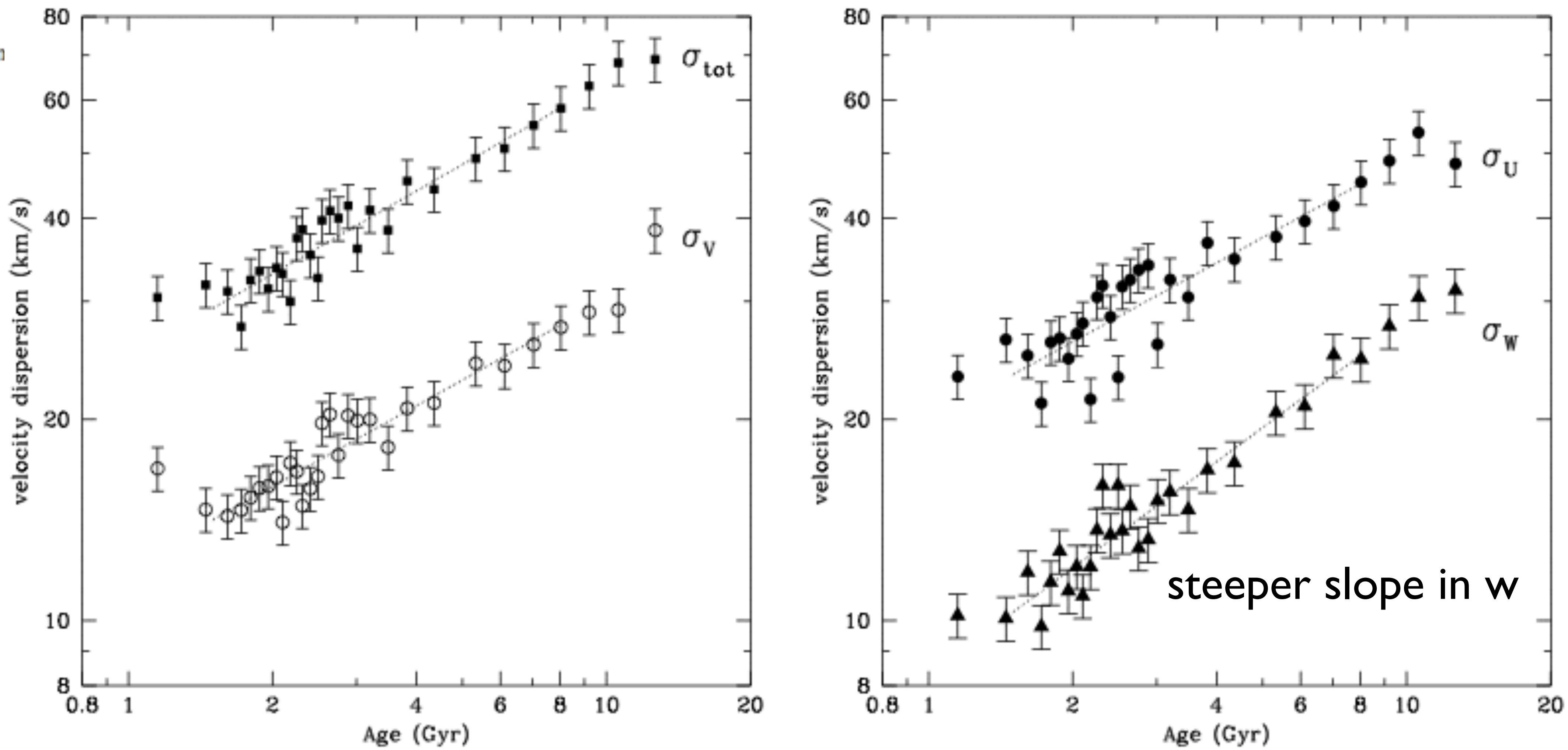

ig. 7. Velocity dispersions vs. age for the subsample with $\sigma_{Age} < 25\%$. The 30 bins have equal numbers of stars (88 in each); the lines show fitted ower laws. The 3 youngest and oldest bins were excluded from the fit.

Formation of the Galactic Disk

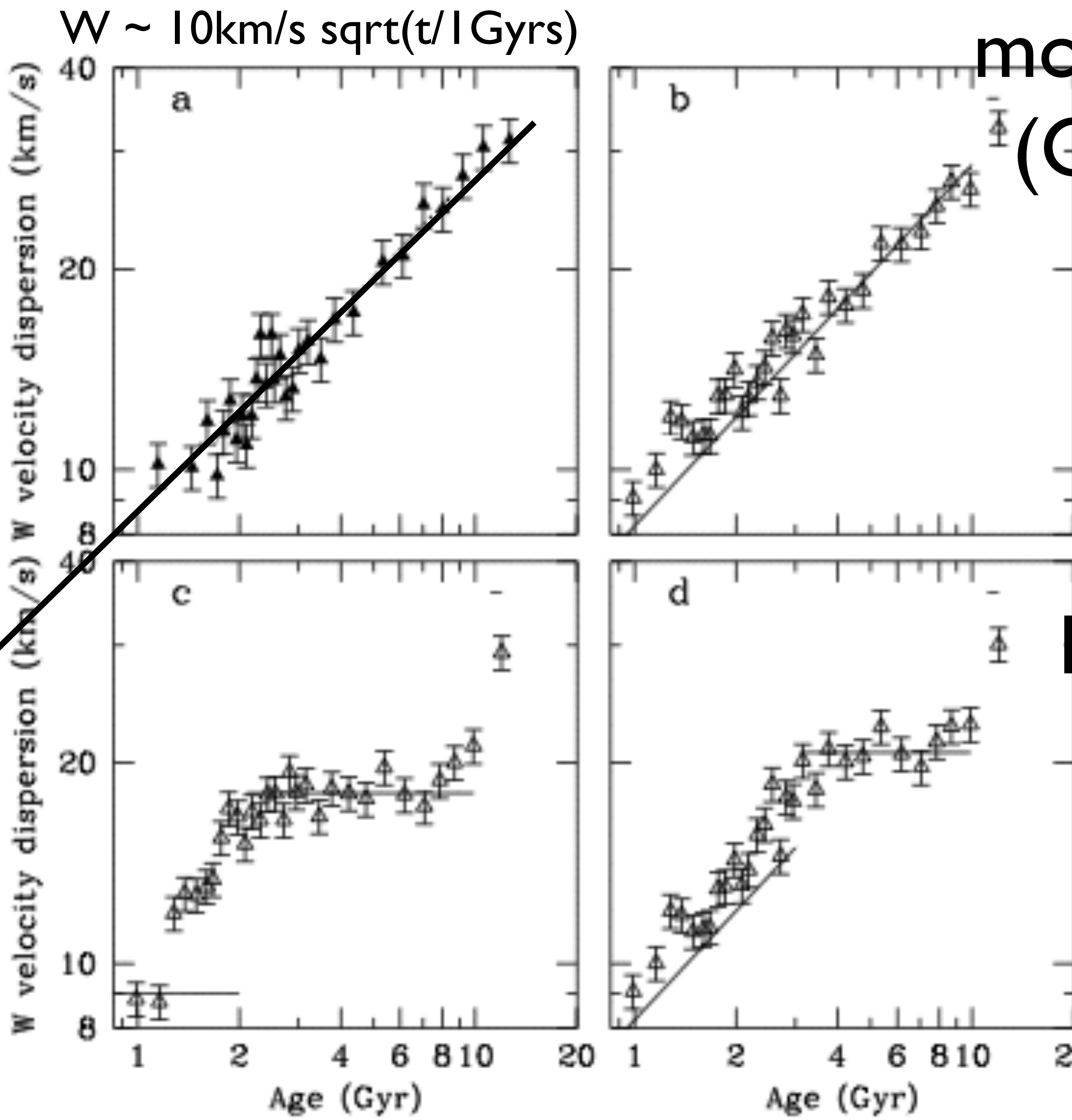

Fig. 8. a): observed AVR in *W* (Fig. 7) with the fitted power law. **b-d)**: simulated AVRs for three different disk heating scenarios (see text). *Open symbols*: rederived ages and velocity dispersions for the synthetic stars (sampling as in **a**); $\sigma_{\mathrm{Age}} < 25\%$).

model I: continuous stirring (GMC? radial migration?)

Model II: minor mergers

Model III: stirring + merger

GAIA will majorly improve on distances, & more stars

We have two disks (thin, thick)?

Star counts (SDSS, Juric et al '08)

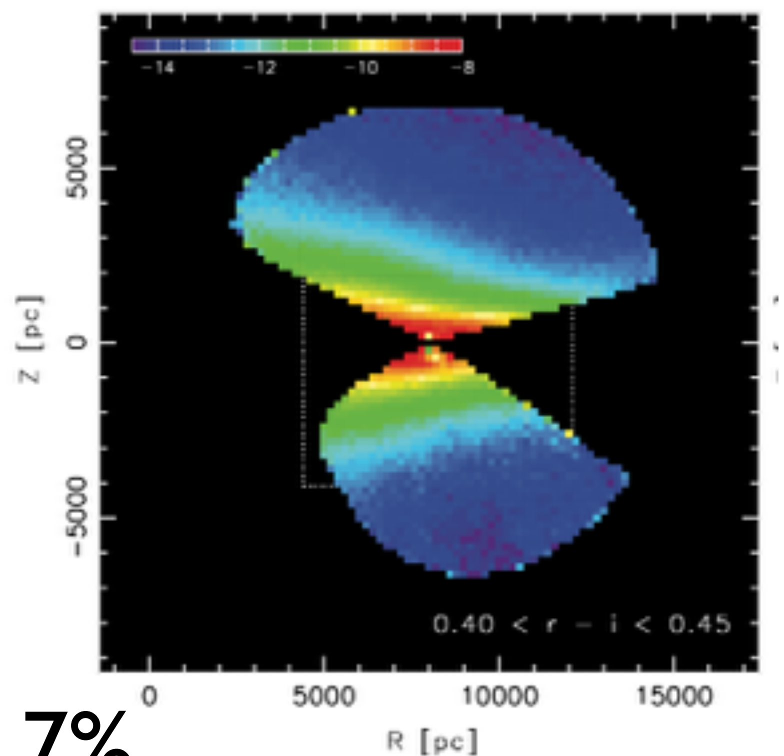

[Fe/H] (SDSS, Ivezic et al '08)

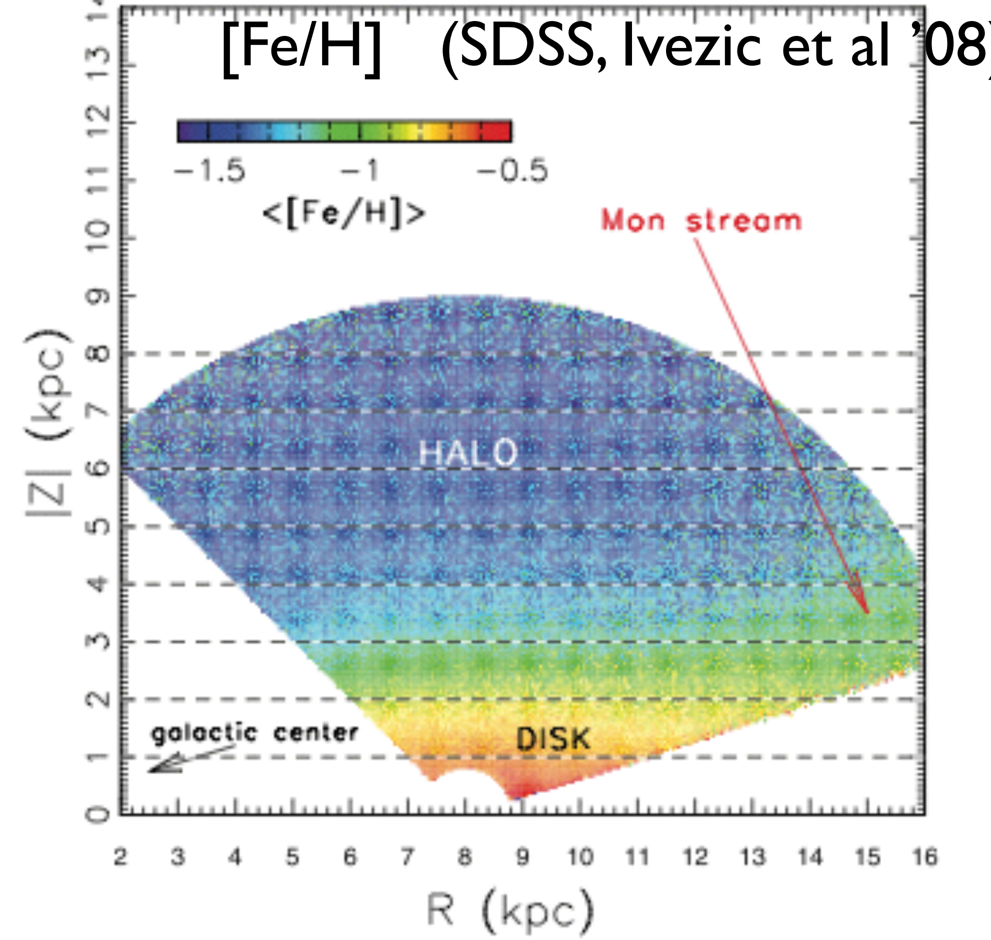

$\Sigma_{thick}/\Sigma_{thin} \sim 7\%$

$\rho_{thick}/\rho_{thin} \sim 2\%$

thin disk Hz ~ 300pc
thick disk Hz ~ 1kpc

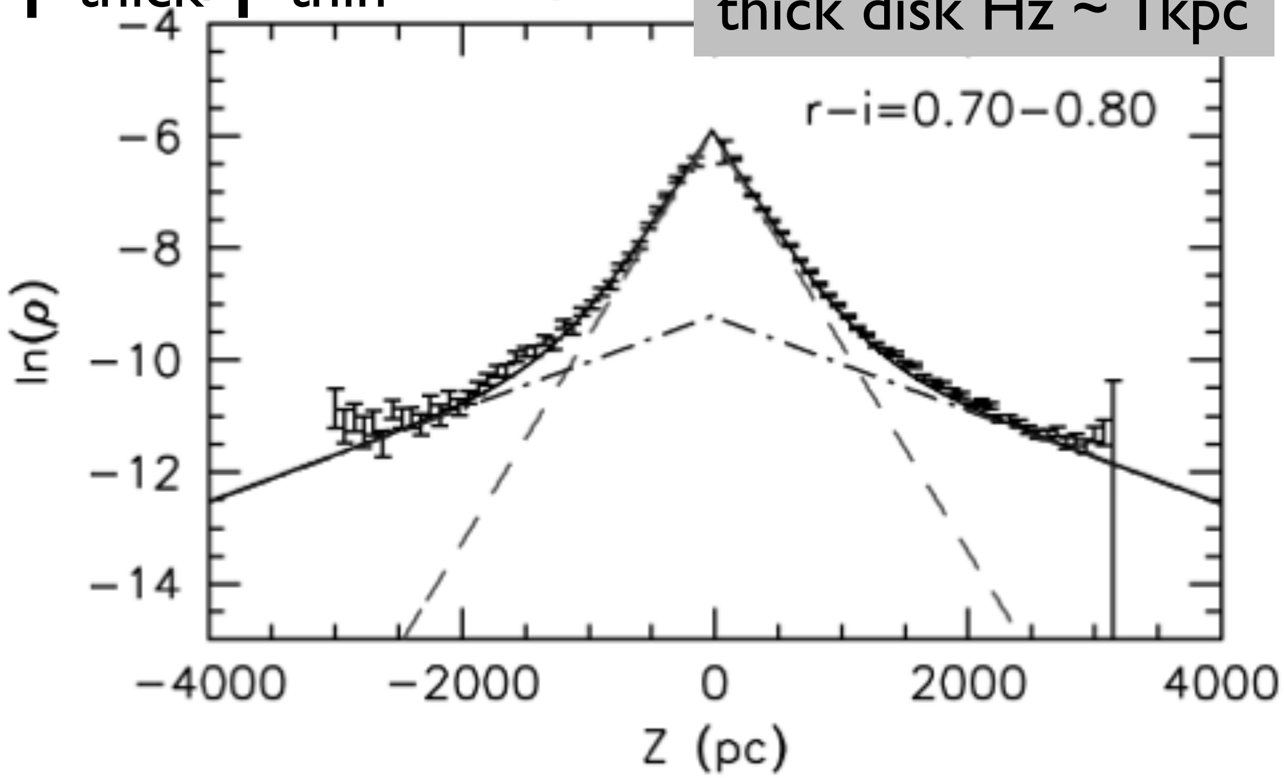

thin disk: [Fe/H] > -0.6
thick disk: lower average

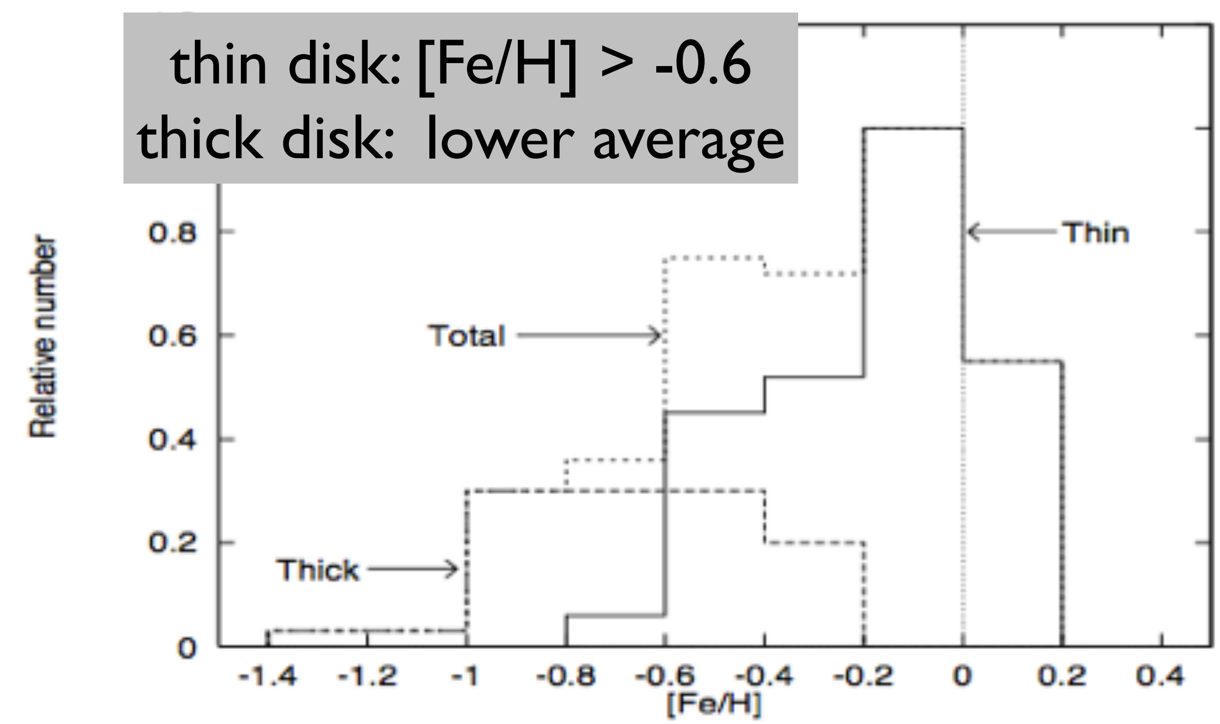

Figure 1. Iron MDFs for Thick and Thin disks, after Gilm

the "G-dwarf problem
(lack of metal-poor disk stars, even at 11Gyrs)

Break-down of the epicycle approximation:

$$\Phi_{\text{eff}} = \Phi_{\text{eff}}(R_{\text{g}}, 0) + \tfrac{1}{2}\left(\frac{\partial^2 \Phi_{\text{eff}}}{\partial R^2}\right)_{(R_{\text{g}},0)} x^2 + \tfrac{1}{2}\left(\frac{\partial^2 \Phi_{\text{eff}}}{\partial z^2}\right)_{(R_{\text{g}},0)} z^2 + \mathrm{O}(xz^2). \quad (3.76)$$

Taylor expansion fails when large x,z oscillations (hotter populations)

Break-down of the epicycle approximation:

<v>: asymmetric drift, density gradient matters; rotational support reduced

the spring constants (κ, ν) no longer constants

<v^2>: ratio modified

$$\boxed{\frac{\overline{[v_\phi - v_c(R_0)]^2}}{\overline{v_R^2}} \simeq \frac{-B}{A-B} = -\frac{B}{\Omega_0} = \frac{\kappa_0^2}{4\Omega_0^2}}$$

392 *W. Dehnen and J. J. Binney*

epicycles only apply to
small dispersions

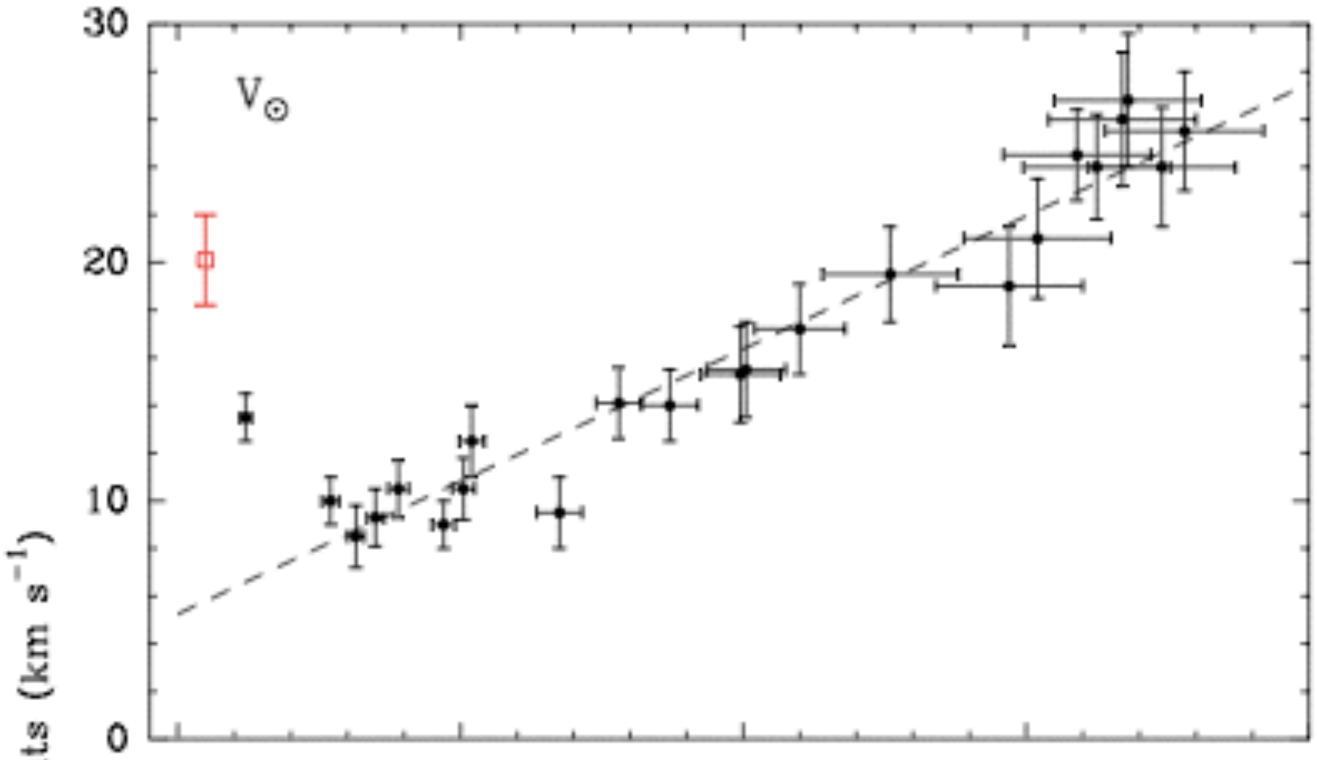

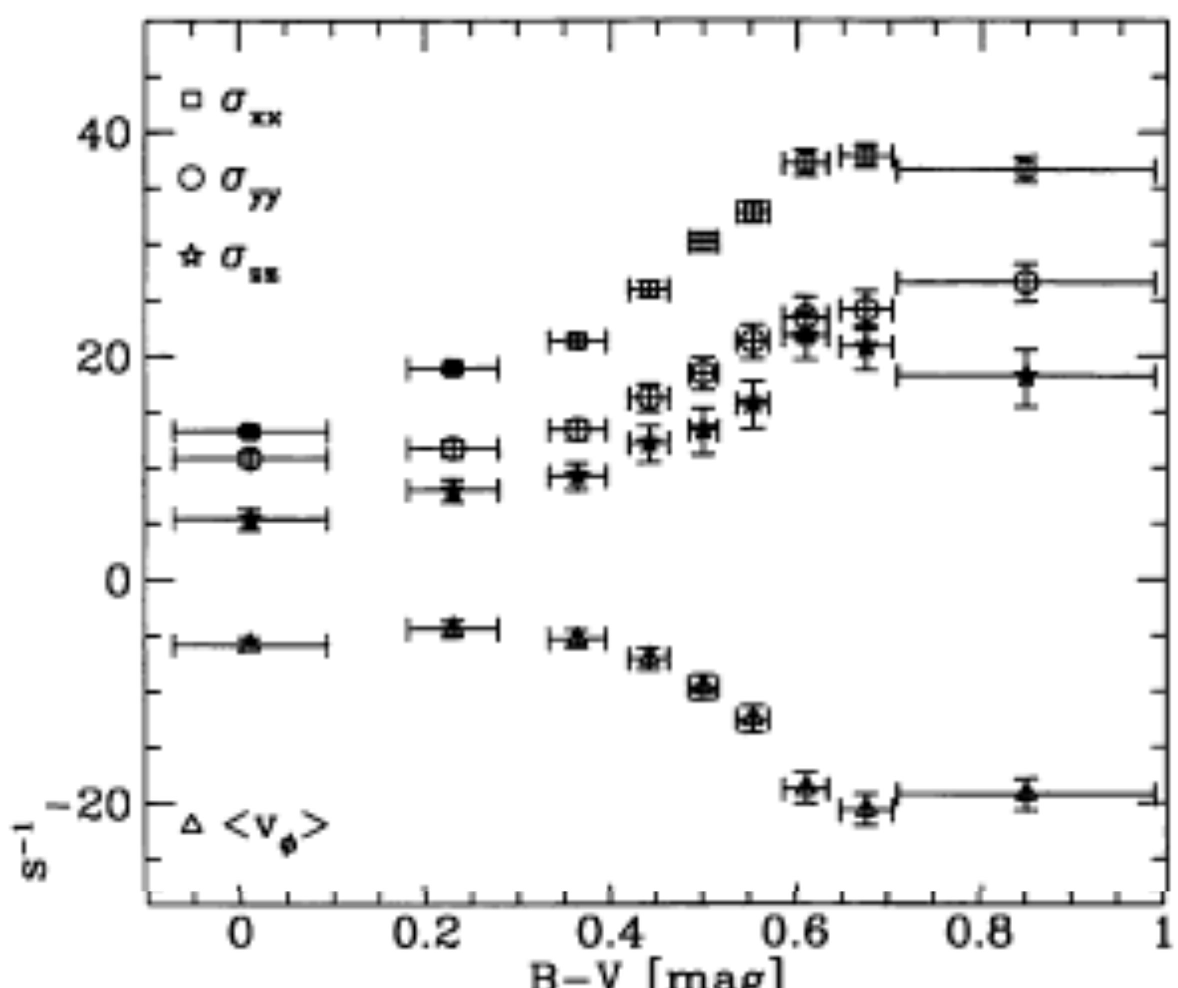

Break-down of the epicycle approximation:

rotational lag (asymmetric drift)

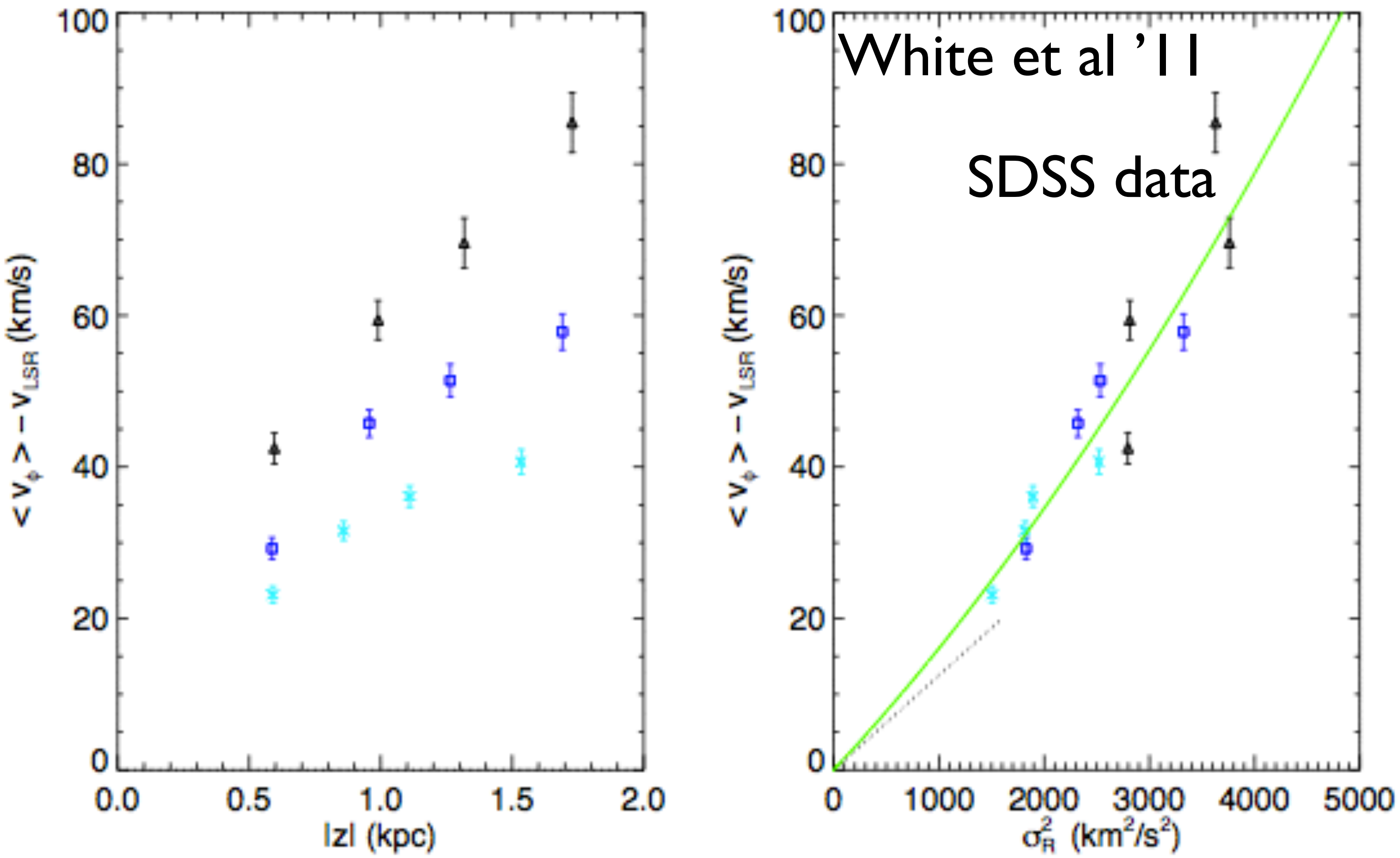

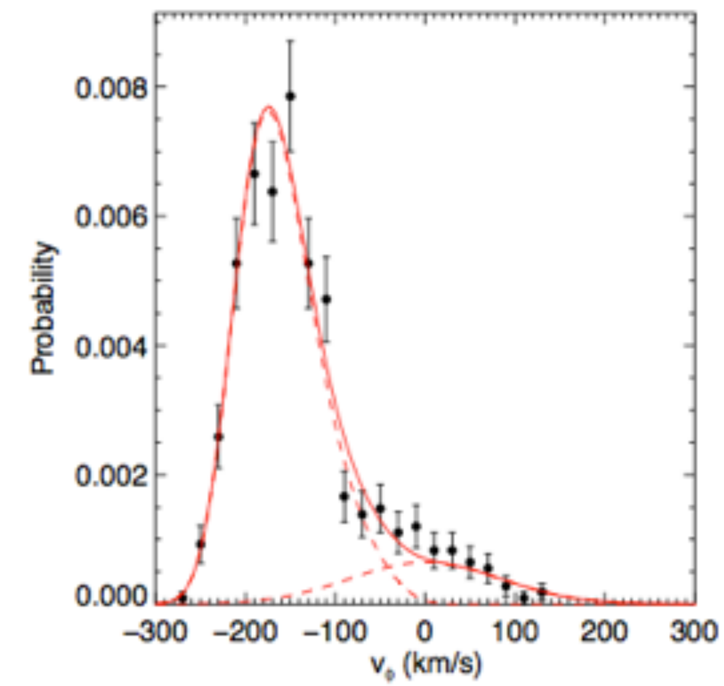

FIG. 1.— An example of one of the fits to our distribution of v_ϕ, using the method described in Section 3.2 This figure shows the most metal-poor bin for stars at heights of around 1 kpc below the plane (corresponding to the 10th column of Table 1).

Figure 1. The rotational lag, plotted against z (left) and against the radial velocity dispersion (right). The triangles, squares and crosses correspond to metal-poor, intermediate-metallicity and metal-rich populations, respectively. The dotted line in the right panel corresponds to the solar-neighborhood relation from Dehnen & Binney (1998a) and the solid line denotes an empirical fit with the lag equal to $0.0149\sigma_R^2 + 1.21 \times 10^{-6}\sigma_R^4$. Figure taken from Smith et al. (2012).

To account for these, need a new tool:
distribution function & Jeans equations

result into equation (4.4) we obtain the **collisionless Boltzmann equation**[1]

$$\frac{\partial f}{\partial t} + \dot{\mathbf{q}} \cdot \frac{\partial f}{\partial \mathbf{q}} + \dot{\mathbf{p}} \cdot \frac{\partial f}{\partial \mathbf{p}} = 0, \tag{4.6}$$

or $df/dt = 0$

- Integral of motion, or any function of the integral of motion satisfies the **collisionless Boltzmann equation.**
- Regular motion has 3 integrals of motion.
- 6-D variables: 3 integrals of motion, 3 phases

Orbits in axisymmetric potential

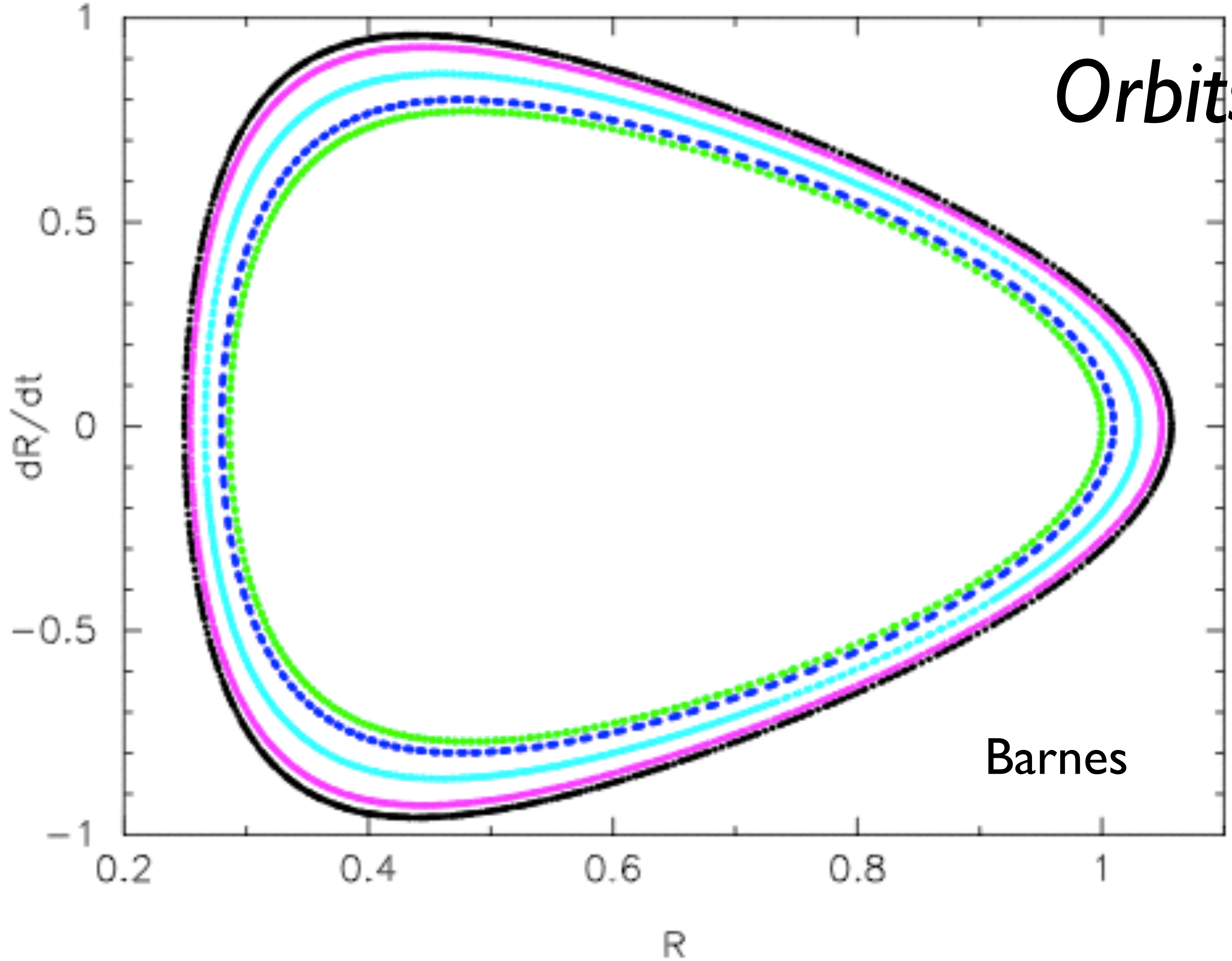

Figure 8.2: Surface of section for five orbits in the logarithmic potential (8.1

same E/L_z

non-crossing in surface of section

bound by a 3rd integral

3rd integral not analytical

total L almost conserved

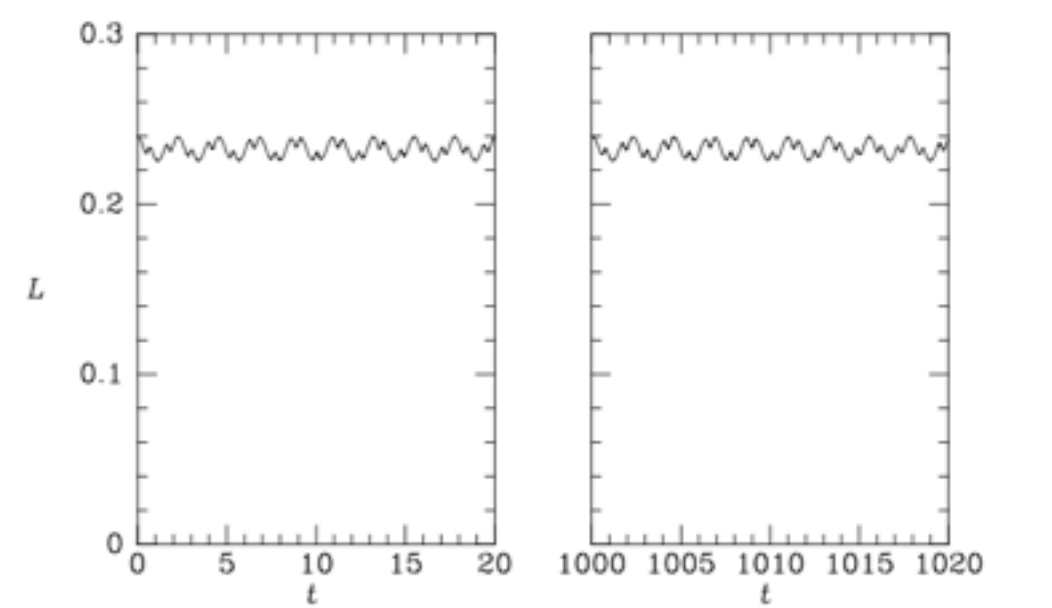

Figure 3.6 The total angular momentum is almost constant along the orbit shown in th left panel of Figure 3.5. For clarity $L(t)$ is plotted only at the beginning and end of a lon integration.

In summary, the Jeans theorem tells us that if $I_1, \ldots, I_n$ are n independent integrals in a given potential, then any DF of the form $f(I_1)$, $f(I_1, I_2)$, $\ldots, f(I_1, \ldots, I_n)$ is a solution of the collisionless Boltzmann equation. The strong Jeans theorem tells us that if the potential of a steady-state galaxy is such that almost all orbits are regular, then for all practical purposes the galaxy may be represented by a DF of the form $\boxed{f(I_1, I_2, I_3)}$, where I_1, I_2, I_3 are three independent isolating integrals.

BT p. 285

which distribution does a real galaxy take?
and why?

If potential can decompose $\Phi \approx \Phi_R(R) + \Phi_z(z)$

motion conserves $H_z = \frac{1}{2}\dot{z}^2 + \Phi_z(z)$

so distribution function $f = f(H, L_z, H_z)$

$$f(H, L_z, H_z) = S(L_z) \exp\left(-\frac{\Delta}{\sigma_R^2} - \frac{H_z}{\sigma_3^2}\right).$$

small departure from guiding centre motion

$$\Delta = H - E_c(L_z) \approx H_R + H_z$$

Shu '69, physically motivated
"Schwarzschild Distribution Function"

$$f(H, L_z, H_z) = S(L_z)\exp\left(-\frac{\Delta}{\sigma_R^2} - \frac{H_z}{\sigma_3^2}\right).$$

Shu '69, **physically motivated**
"Schwarzschild Distribution Function"

this seems a reasonably good approximation for stars in the solar neighbourhood.

but how do stars acquire this distribution?

why not other forms?
— *S(Lz) corresponds to $\Sigma(R)$*
— *Gibbs hypothesis*
— *constraint: only some forms are compatible with $\Phi(R,z)$*
— *a result of prior heating?*
— *certain forms maximize entropy?*
— *results of initial condition?*

observationally, $\sigma_3^2 \sim 1/2\ \sigma_R^2$

How to use Distribution Functions?

$$\frac{\partial f}{\partial t} + \dot{\mathbf{q}} \cdot \frac{\partial f}{\partial \mathbf{q}} + \dot{\mathbf{p}} \cdot \frac{\partial f}{\partial \mathbf{p}} = 0,$$

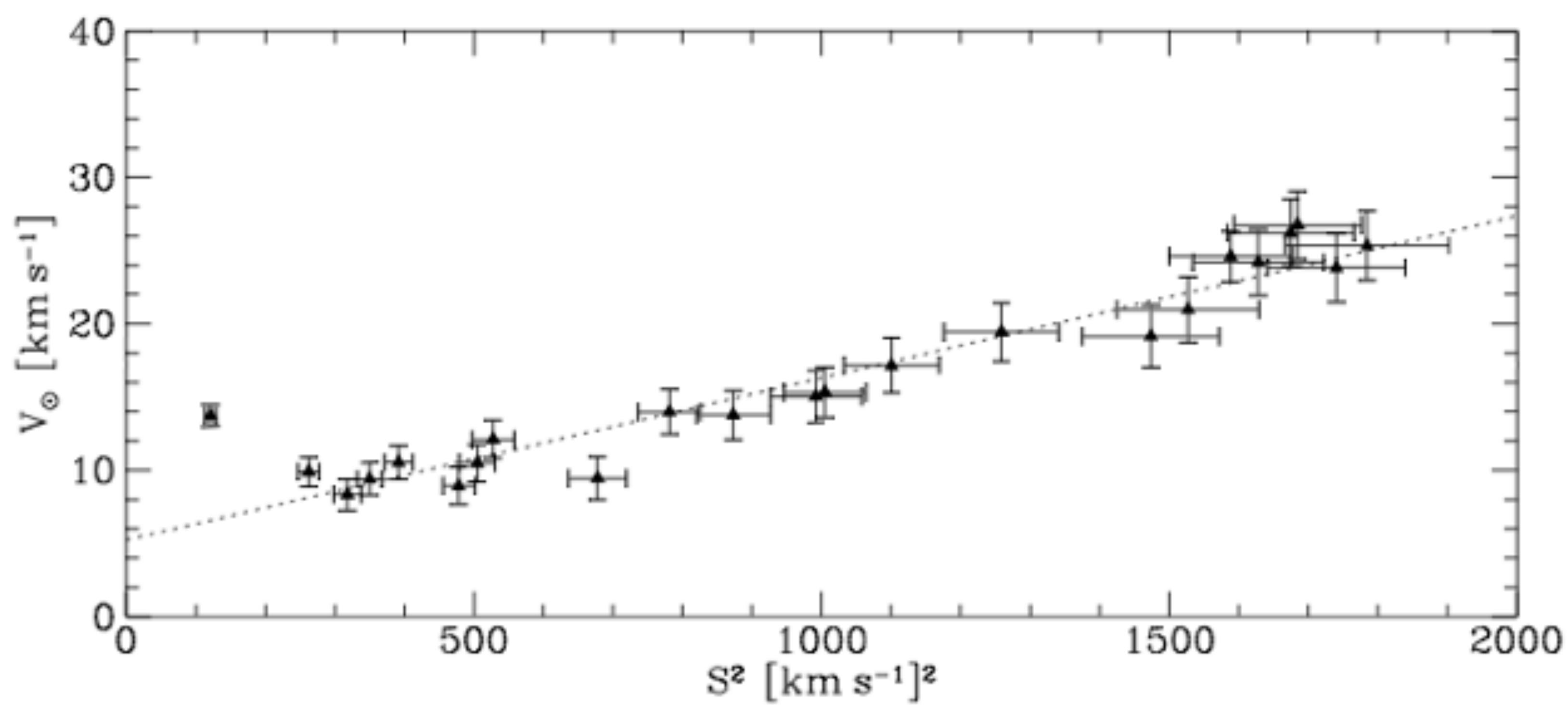

Figure 4.21 The asymmetric drift v_a for different stellar types is a linear function of the random velocity S^2 of each type. The vertical coordinate is actually $v_a + \widetilde{v}_{\phi,\odot}$ where $\widetilde{v}_{\phi,\odot}$ is the azimuthal velocity of the Sun relative to the LSR (after Dehnen & Binney 1998b).

keep taking moments… Jeans equations (1919)

The Jeans equation (1919)

$$\frac{\partial \nu}{\partial t} + \frac{\partial(\nu \overline{v}_i)}{\partial x_i} = 0.$$

$$\nu \frac{\partial \overline{v}_j}{\partial t} + \nu \overline{v}_i \frac{\partial \overline{v}_j}{\partial x_i} = -\nu \frac{\partial \Phi}{\partial x_j} - \frac{\partial(\nu \sigma_{ij}^2)}{\partial x_i}.$$

the radial Jeans equation in cylindrical coordinates, steady state

$$\frac{\partial(\nu \overline{v_R^2})}{\partial R} + \frac{\partial(\nu \overline{v_R v_z})}{\partial z} + \nu \left(\frac{\overline{v_R^2} - \overline{v_\phi^2}}{R} + \frac{\partial \Phi}{\partial R} \right) = 0. \qquad (4.222a)$$

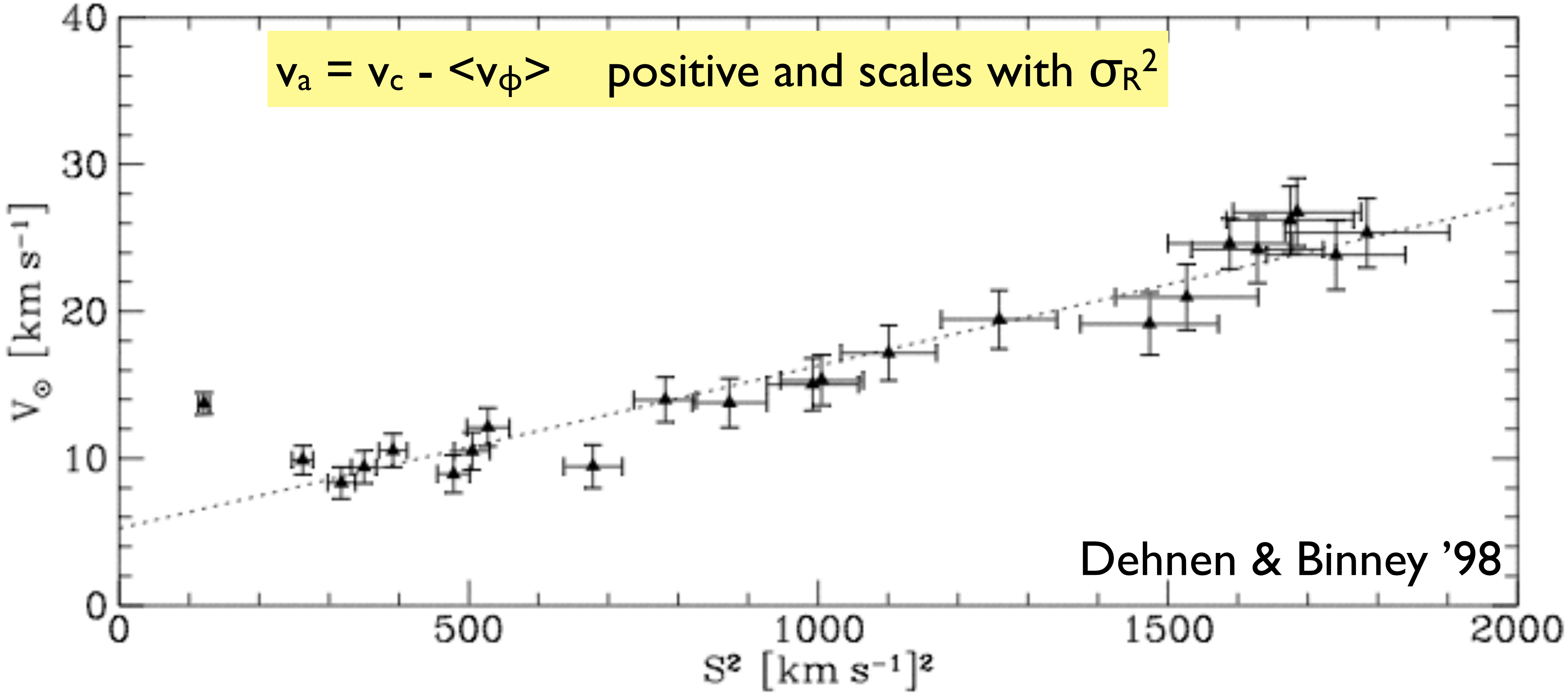

Figure 4.21 The asymmetric drift v_a for different stellar types is a linear function of the random velocity S^2 of each type. The vertical coordinate is actually $v_a + \widetilde{v}_{\phi,\odot}$ where $\widetilde{v}_{\phi,\odot}$ is the azimuthal velocity of the Sun relative to the LSR (after Dehnen & Binney 1998b).

The radial Jeans equation:

$$v_a \simeq \frac{\overline{v_R^2}}{2v_c}\left[\frac{\sigma_\phi^2}{\overline{v_R^2}} - 1 - \frac{\partial \ln(\nu\overline{v_R^2})}{\partial \ln R} - \frac{R}{\overline{v_R^2}}\frac{\partial(\overline{v_R v_z})}{\partial z}\right].$$

the gradient measures…

why can it apply to diff. populations?

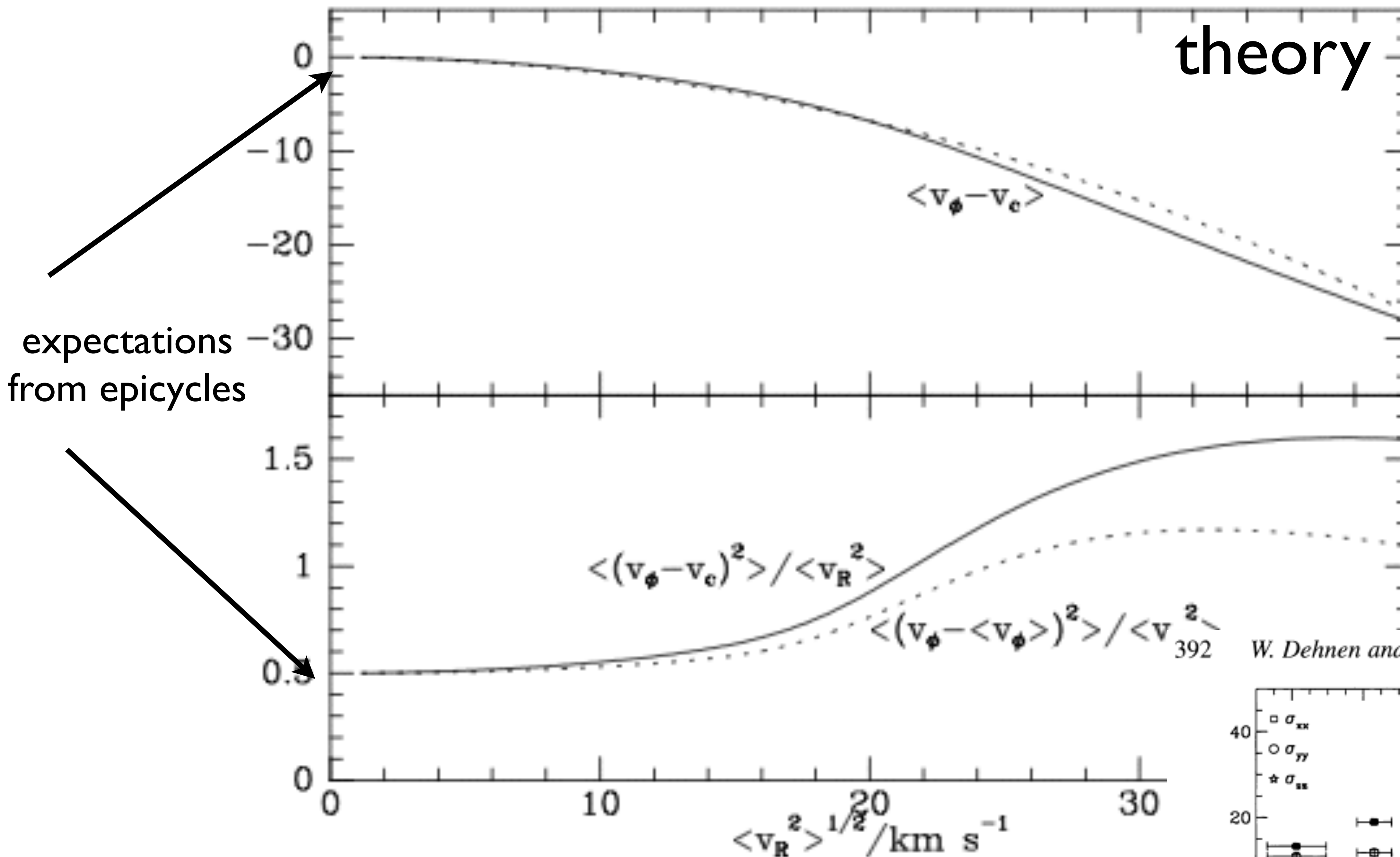

Figure 4.16 Upper panel: the mean value of $\widetilde{v}_\phi$ as a functic
velocity distributions like those plotted in Figure 4.15. The dasl
fit to the curve. Lower panel: for the same distributions thi
$\overline{(v_\phi - \overline{v}_\phi)^2}/\overline{v_R^2}$ (dashed).

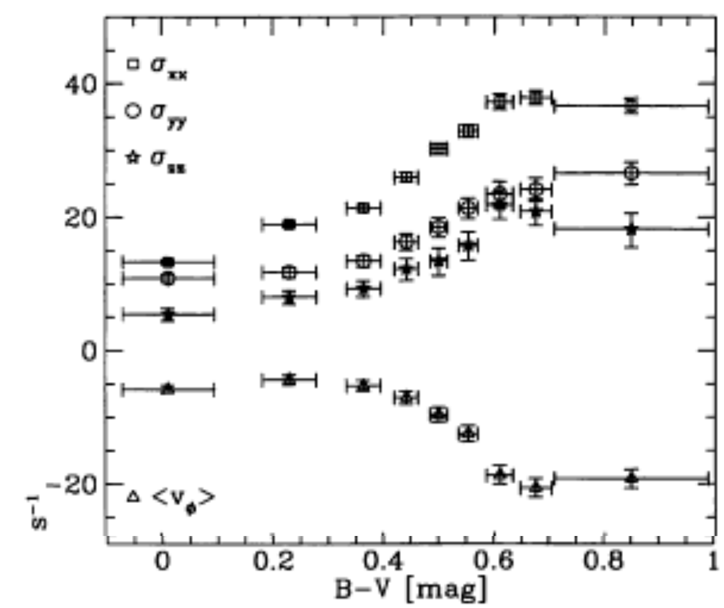

Figure 5. Velocity dispersions for stars in different colour bins. The top panel shows the mean rotation velocity (negative values imply lagging with respect to the LSR) and the three main velocity dispersions. In the three bottom panels $\sigma'_{ij} = \mathrm{sign}(\sigma^2_{ij})\,|\sigma^2_{ij}|^{1/2}$ is plotted for the mixed components of the tensor σ^2_{ij}.

The vertical Jeans equation (beyond the epicycles)

$$\frac{1}{R}\frac{\partial(R\nu\overline{v_R v_z})}{\partial R}+\frac{\partial(\nu\overline{v_z^2})}{\partial z}+\nu\frac{\partial\Phi}{\partial z}=0,\qquad 4\pi G\rho=-\frac{\partial}{\partial z}\left(\frac{1}{\nu}\frac{\partial(\nu\overline{v_z^2})}{\partial z}\right).$$

nu is tracer density, not rho

$$\rho(0)=(0.10\pm0.01)\,\mathcal{M}_\odot\,\mathrm{pc}^{-2}.\qquad \Sigma_{1.1}(R_0)=(71\pm6)\,\mathcal{M}_\odot\,\mathrm{pc}^{-2}.$$

using A/F stars

using G/K stars

Holmberg & Flynn '00, Hipparcos data

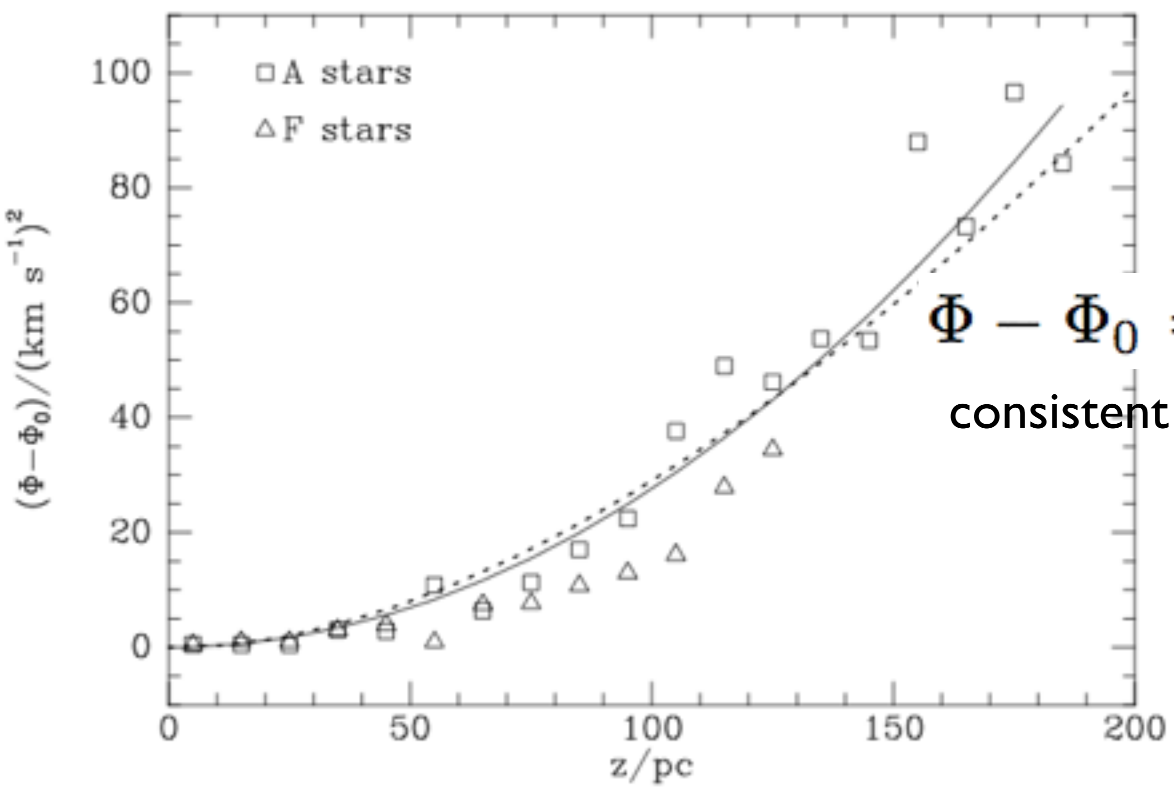

$$\Phi-\Phi_0=\tfrac{1}{2}kz^2,$$

consistent with…

4.26 The change in gravitational potential near the Sun between the midplane
ht z above the plane. Squares show values obtained with equations (4.276) from
ar sample of Holmberg & Flynn (2000), while the triangles are from their F-star
The full curve is a least-squares fit of a parabola: it is the internal gravitational
of a homogeneous slab with mass density $0.101\,\mathcal{M}_\odot\,\mathrm{pc}^{-3}$. The dashed curve
e potential of Model I of §2.7.

Smith, Whiteoak, Evans '12, SDSS data

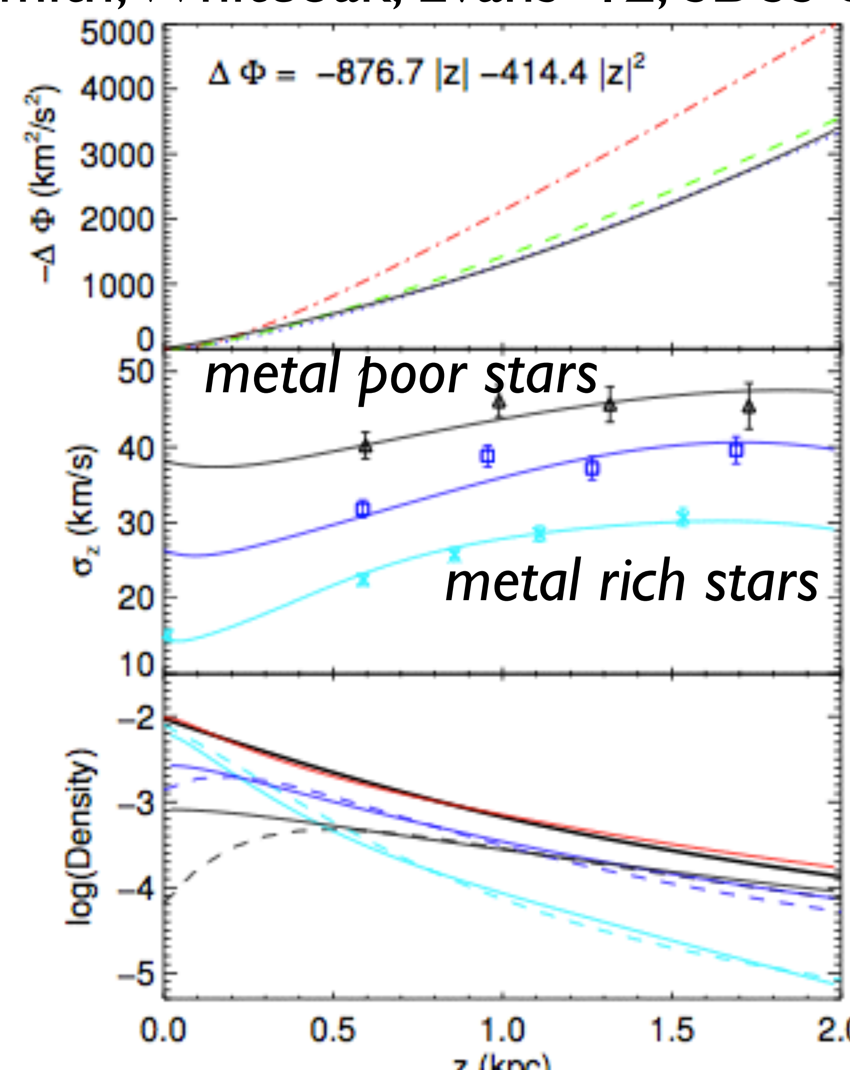

Measured mass-to-light ratios locally: (extend to +/- 1.1kpc)

Table 1.1 Inventory of the solar neighborhood

BT Chap. 1

component	volume density ($\mathcal{M}_\odot\,\mathrm{pc}^{-3}$)	surface density ($\mathcal{M}_\odot\,\mathrm{pc}^{-2}$)	luminosity density ($L_\odot\,\mathrm{pc}^{-3}$)	surface brightness ($L_\odot\,\mathrm{pc}^{-2}$)
visible stars	0.033	29	0.05	29
stellar remnants	0.006	5	0	0
brown dwarfs	0.002	2	0	0
ISM	0.050	13	0	0
total	0.09 ± 0.01	49 ± 6	0.05	29
dynamical	0.10 ± 0.01	74 ± 6	–	–

NOTES: Volume and luminosity densities are measured in the Galactic midplane and surface density is the total within ± 1.1 kpc of the plane. Luminosity density and surface brightness are given in the R band. Dynamical estimates are from §4.9.3. Most other entries are taken from Flynn et al. (2006).

in disk midplane, negligible dark matter

vertically (to +/-1.1kpc), dark matter ~ baryons

GAIA data

Next week: spirals — presentations

BT 6.1: observations; 'leading/trailing', pitch angle/winding problem,
pattern speed, angular momentum transport
Volunteers (2): Mark, Miranda

BT 6.2: Corotation resonance, Lindblad resonance, dispersion relation
for waves (either in fluid or in stellar disks), "Toomre Q"
Volunteers (2): Fei, Alex

BT 6.3: numerical results, 'swing amplifier'
Volunteer (1): Nilu

supplementary reading:

Dynamics of Disks & Warps, Sellwood, 2010
http://arxiv.org/pdf/1006.4855v3.pdf

Dynamics of Secular Evolution, Binney, 2012
http://lanl.arxiv.org/pdf/1202.3403v1.pdf

Non-spherical potential:

triaxial

potential-density pair
stereotype motions
numerical results

BT 2.4, 2.5, 3.3, 3.4

Summary: potentials & orbits

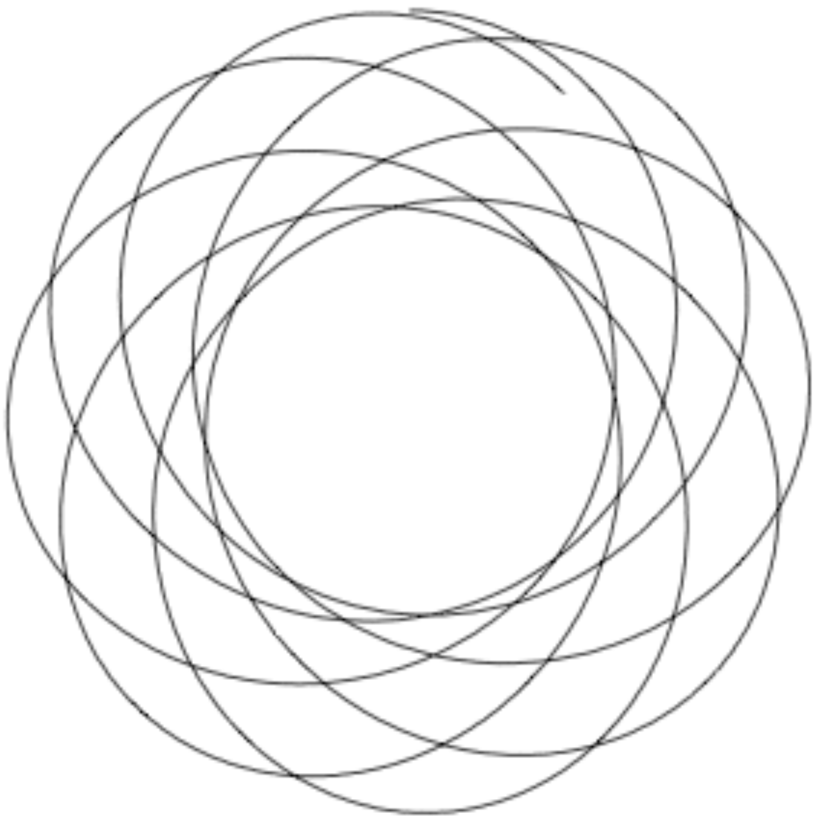

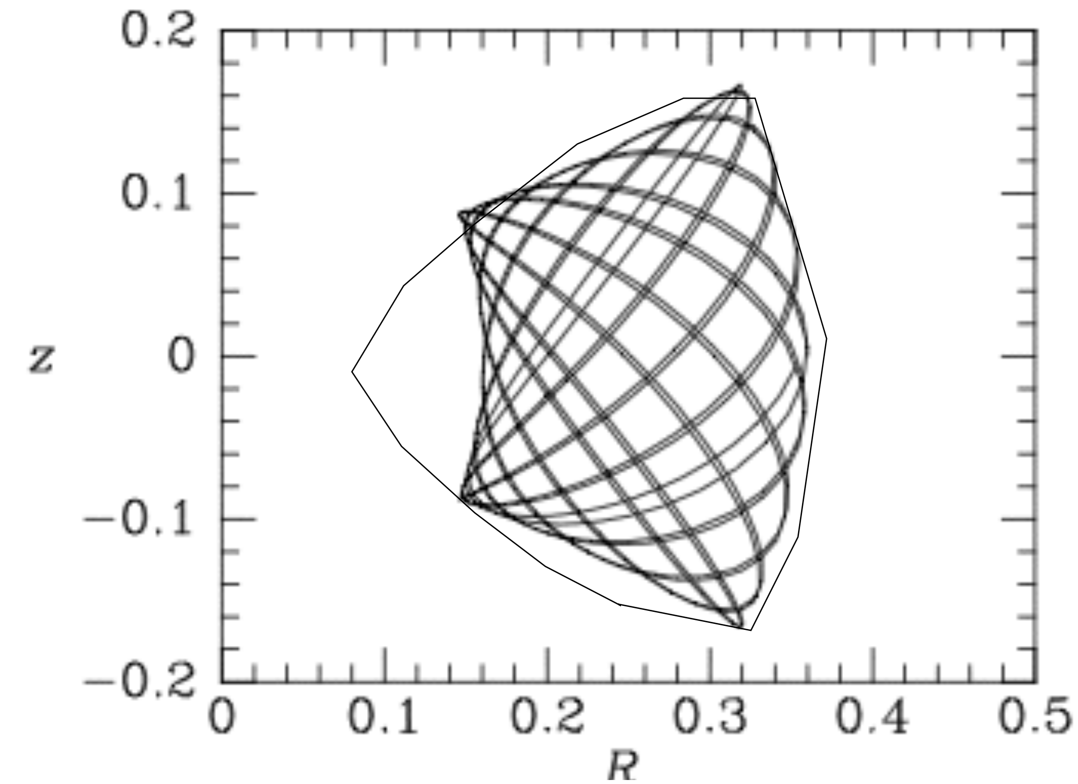

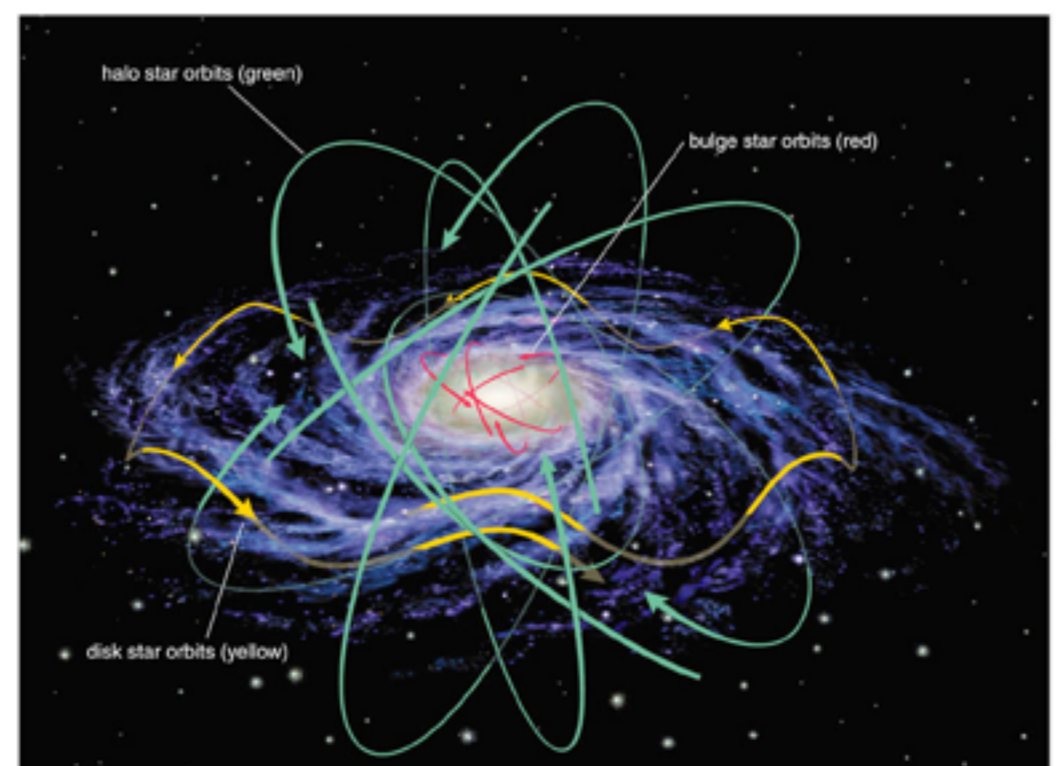

- spherical potential:
- Non-spherical potential: axisymmetric
- Non-spherical potential: non-axisymm planar 2-D

Logarithmic potential (2-D)

$$\Phi_{\rm L}(x,y) = \tfrac{1}{2}v_0^2 \ln\left(R_{\rm c}^2 + x^2 + \frac{y^2}{q^2}\right) \quad (0 < q \leq 1). \tag{3.103}$$

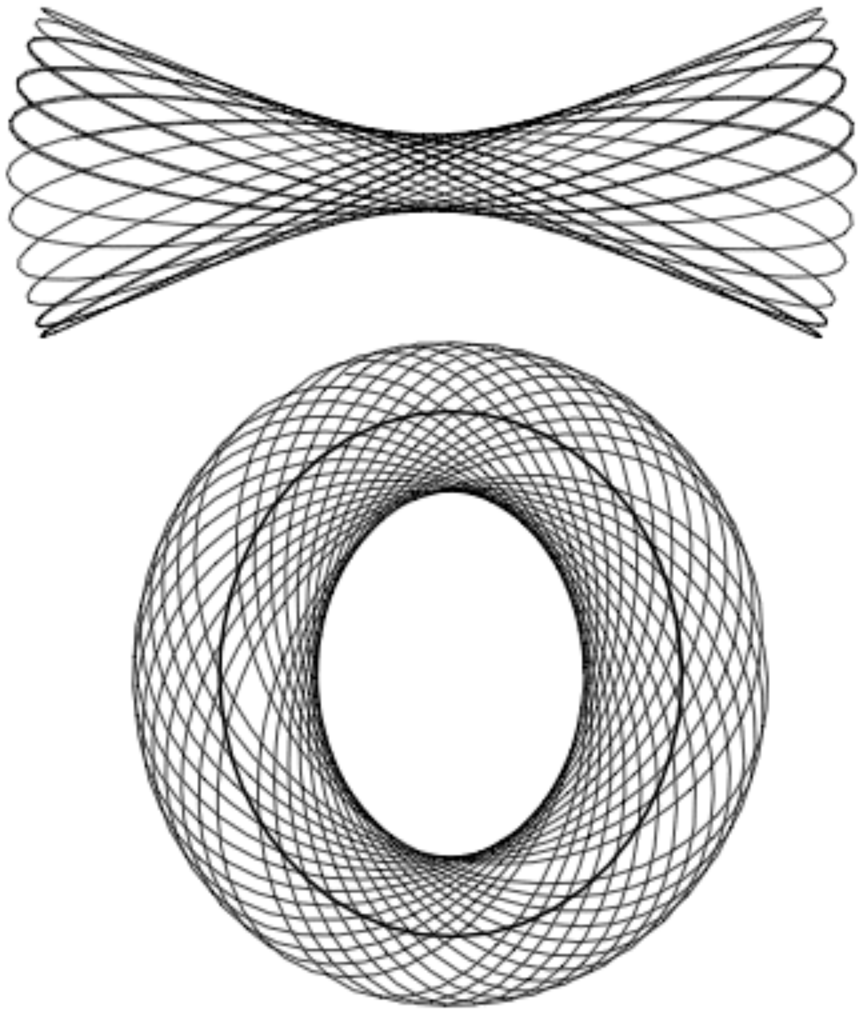

centre-philic

centre-phobic

Figure 3.8 Two orbits of a common energy in the potential Φ_L of equation (3.103) when $v_0 = 1$, $q = 0.9$ and $R_c = 0.14$: top, a box orbit; bottom, a loop orbit. The closed parent of the loop orbit is also shown. The energy, $E = -0.337$, is that of the isopotential surface that cuts the long axis at $x = 5R_c$.

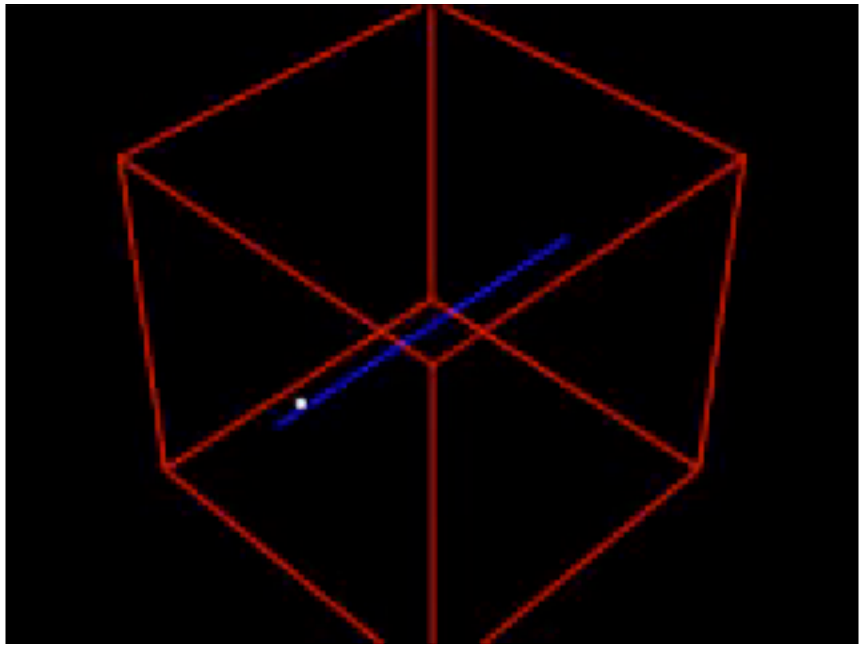

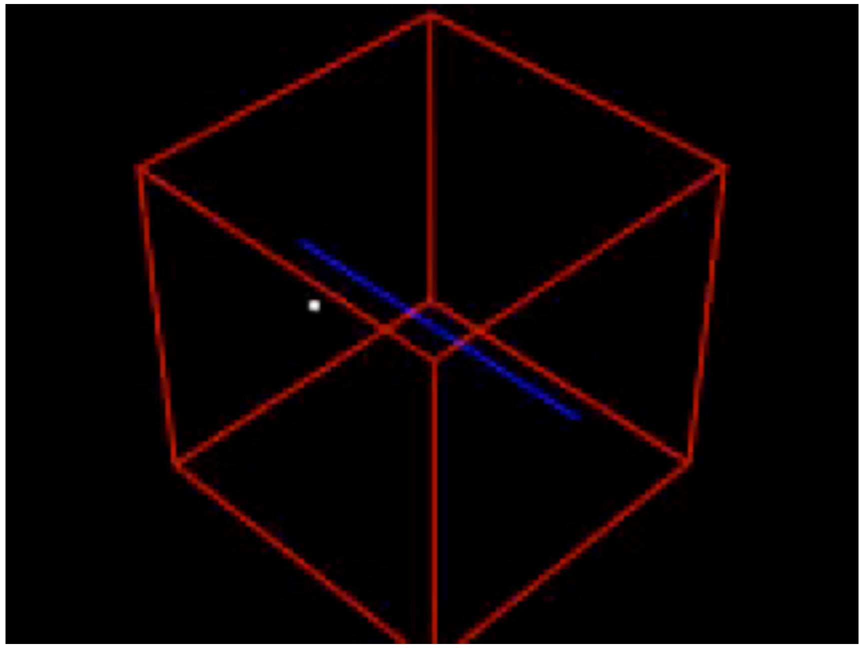

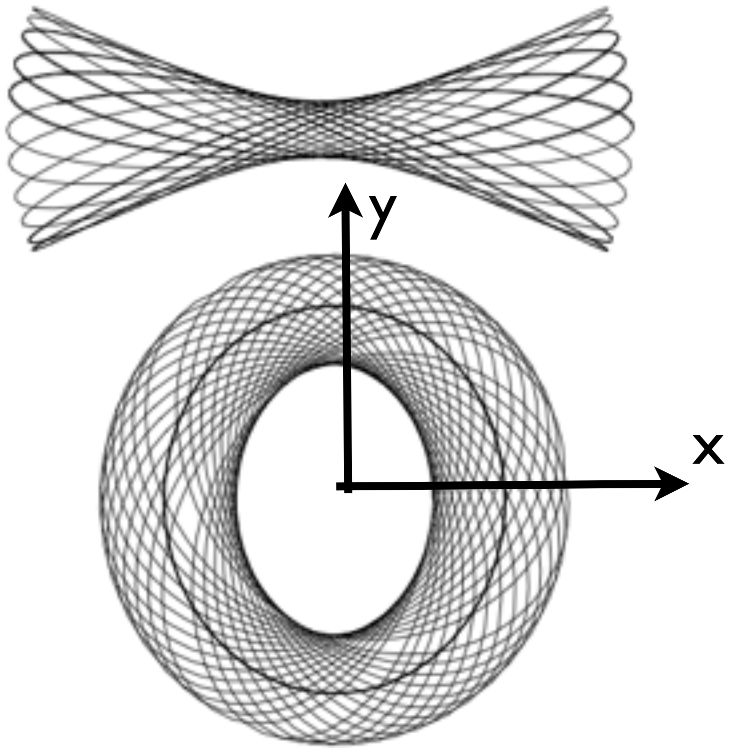

Angular momentum (z-axis)

$$J = \mathbf{r} \times \mathbf{v} = x v_y - y v_x$$

J changes sign in boxy orbit (stems from J=0 orbits)

J ~ conserved in loopy orbit (relic of axi-symmetric potential)

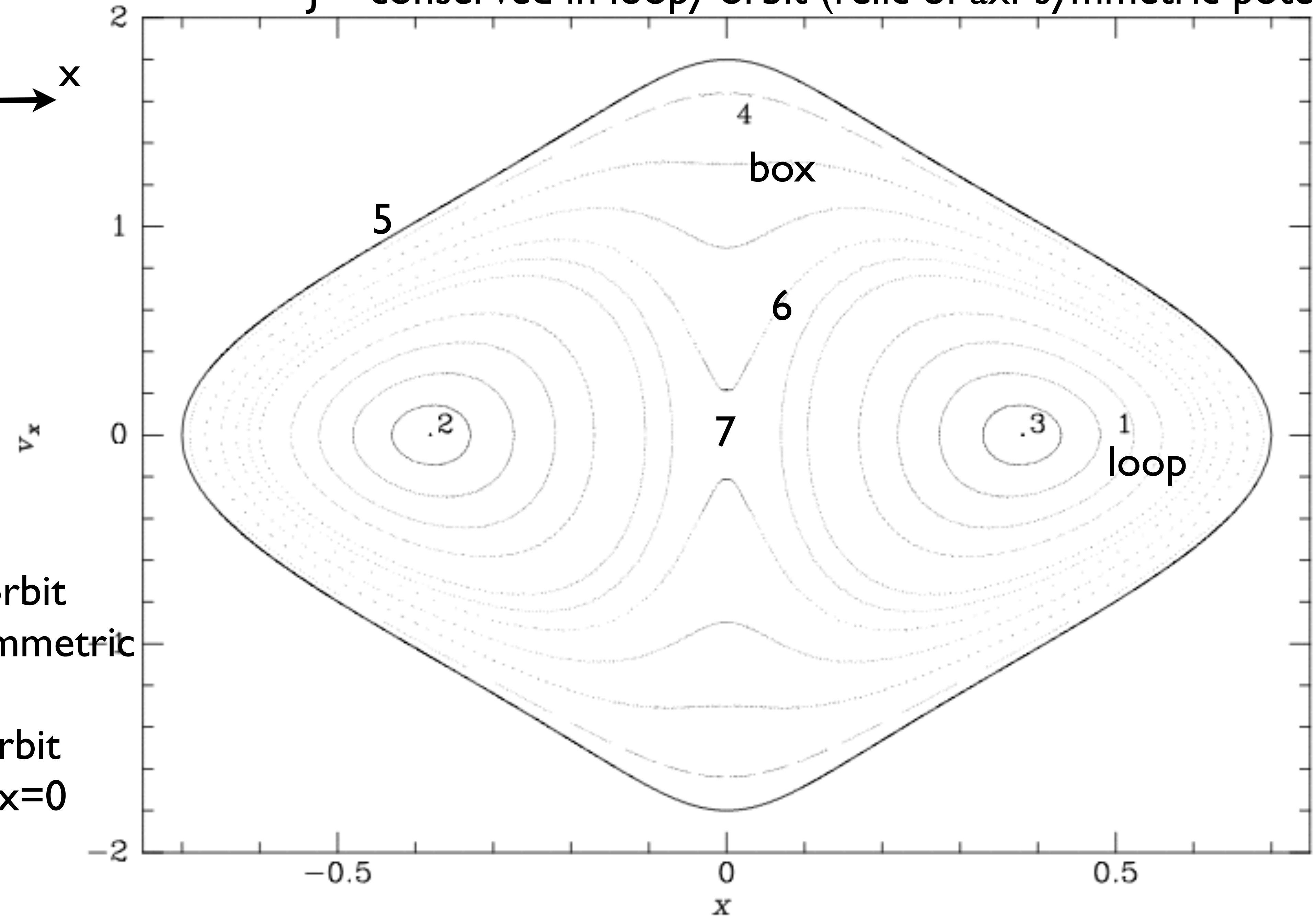

2,3: loopy, periodic orbit
surprising for non-axisymmetric

5,7: boxy, periodic orbit
purely along y=0 or x=0

Figure 3.9 The $(x, \dot{x})$ surface of section formed by orbits in Φ_L of the same energy as the orbits depicted in Figure 3.8. The isopotential surface of this energy cuts the long axis at $x = 0.7$. The curves marked 4 and 1 correspond to the box and loop orbits shown in the top and bottom panels of Figure 3.8.

Surface of section when y=0 and dydt > 0

$$H'_x \equiv \tfrac{1}{2}\dot{x}^2 + \Phi(x,0). \tag{3.108}$$

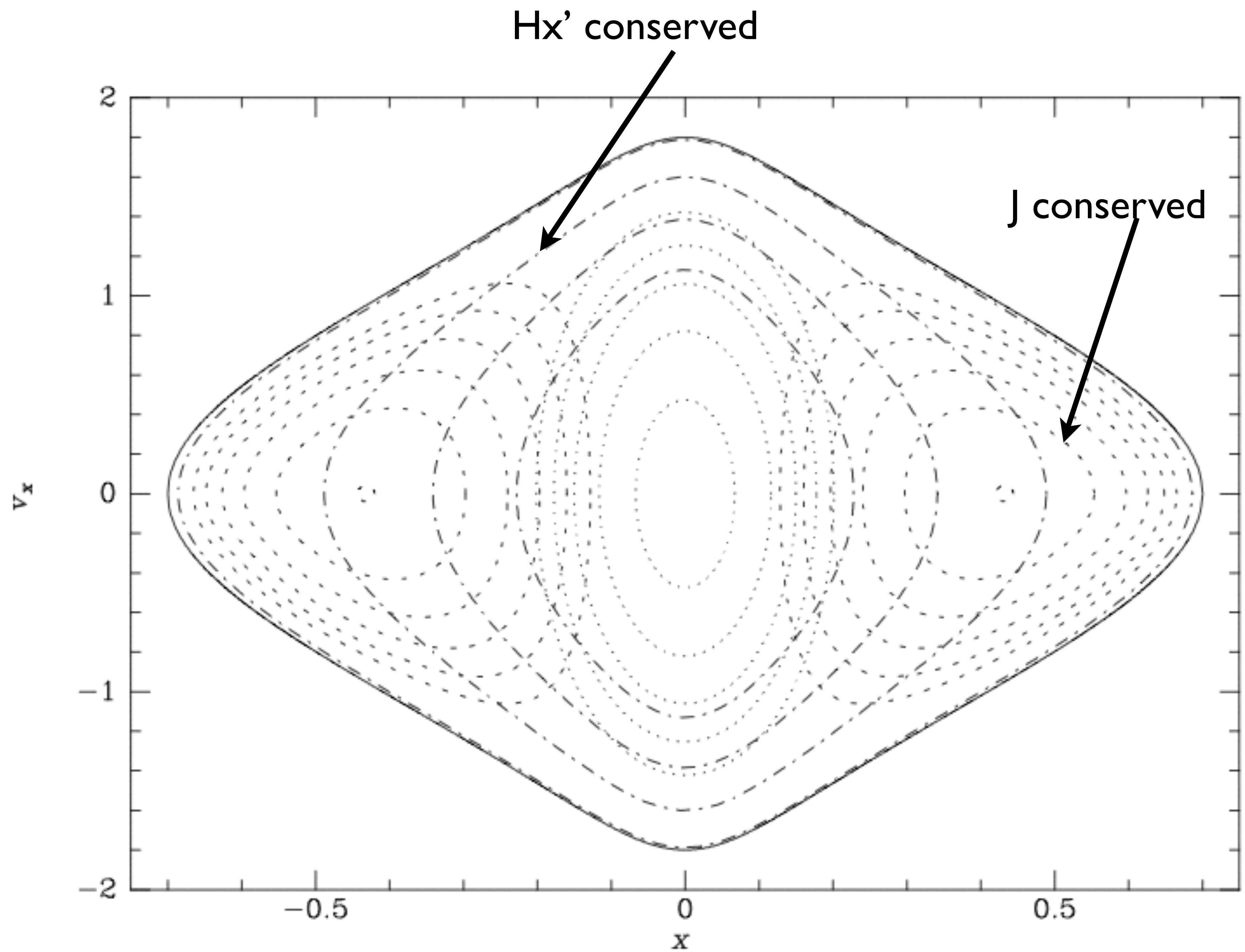

Figure 3.11 The appearance of the surface of section Figure 3.9 if orbits conserved (a) angular momentum (eq. 3.107; dashed curves), or (b) H_x (eq. 3.105; inner dotted curves), or (c) H'_x (eq. 3.108; outer dot-dashed curves).

transition from loop to box and back: roughly corre. to to changing Lz?

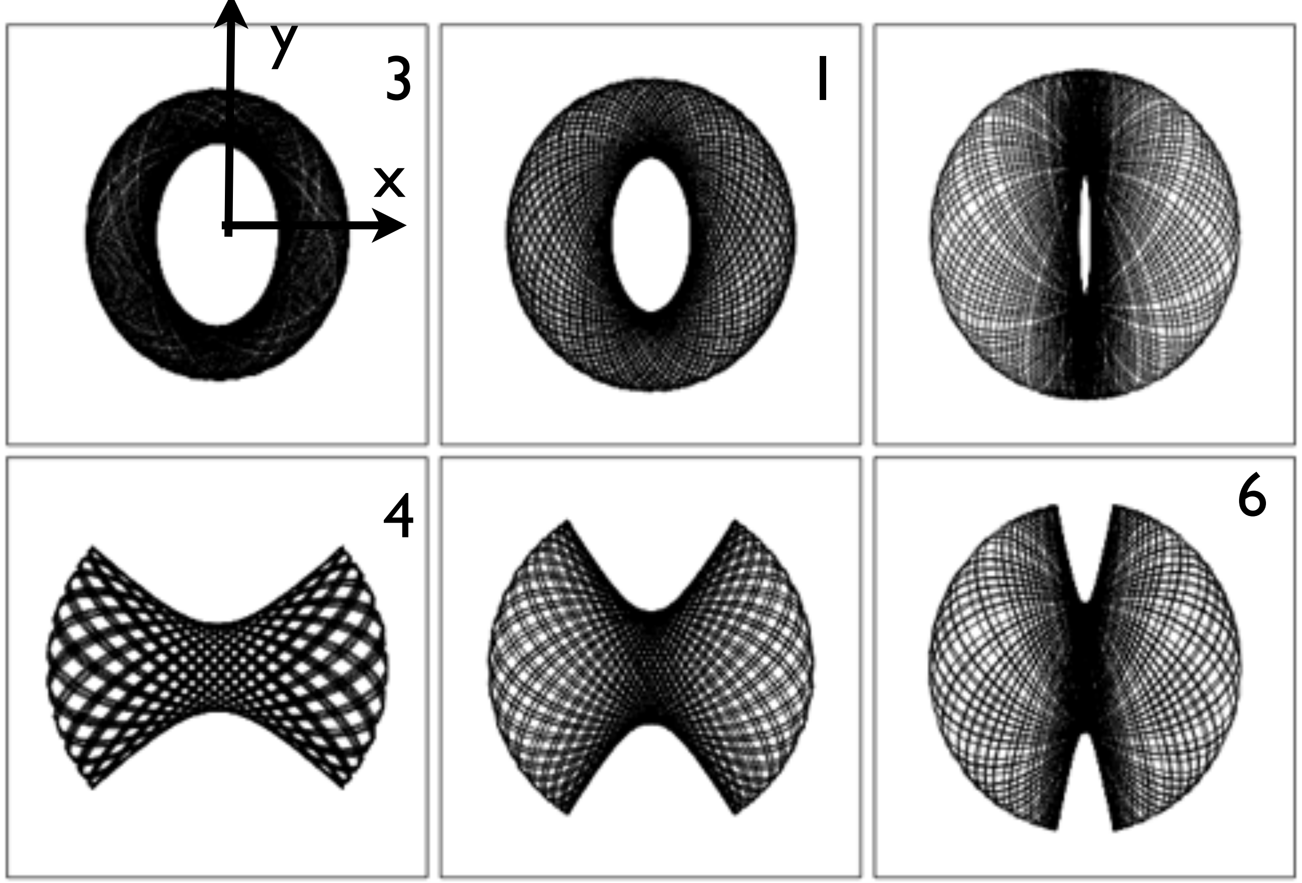

Figure 3.10 A selection of loop (top row) and box (bottom row) orbits in the potential $\Phi_L(q = 0.9, R_c = 0.14)$ at the energy of Figures 3.8 and 3.9.

Figure 3.10 A selection of loop (top row) and box (bottom row) orbits in the potential $\Phi_L(q = 0.9, R_c = 0.14)$ at the energy of Figures 3.8 and 3.9.

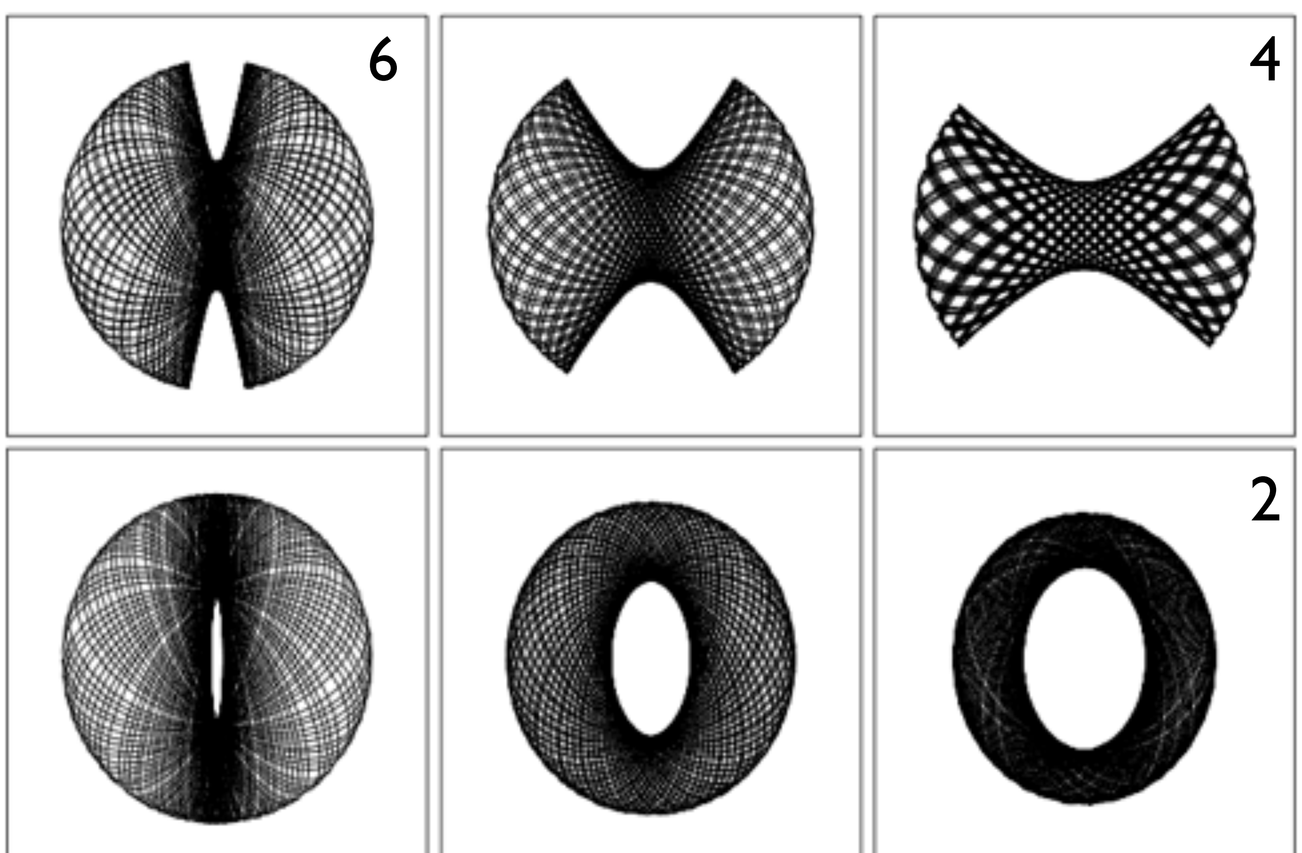

3, 1, 6, 4, 5, 4, 6, 4, 2

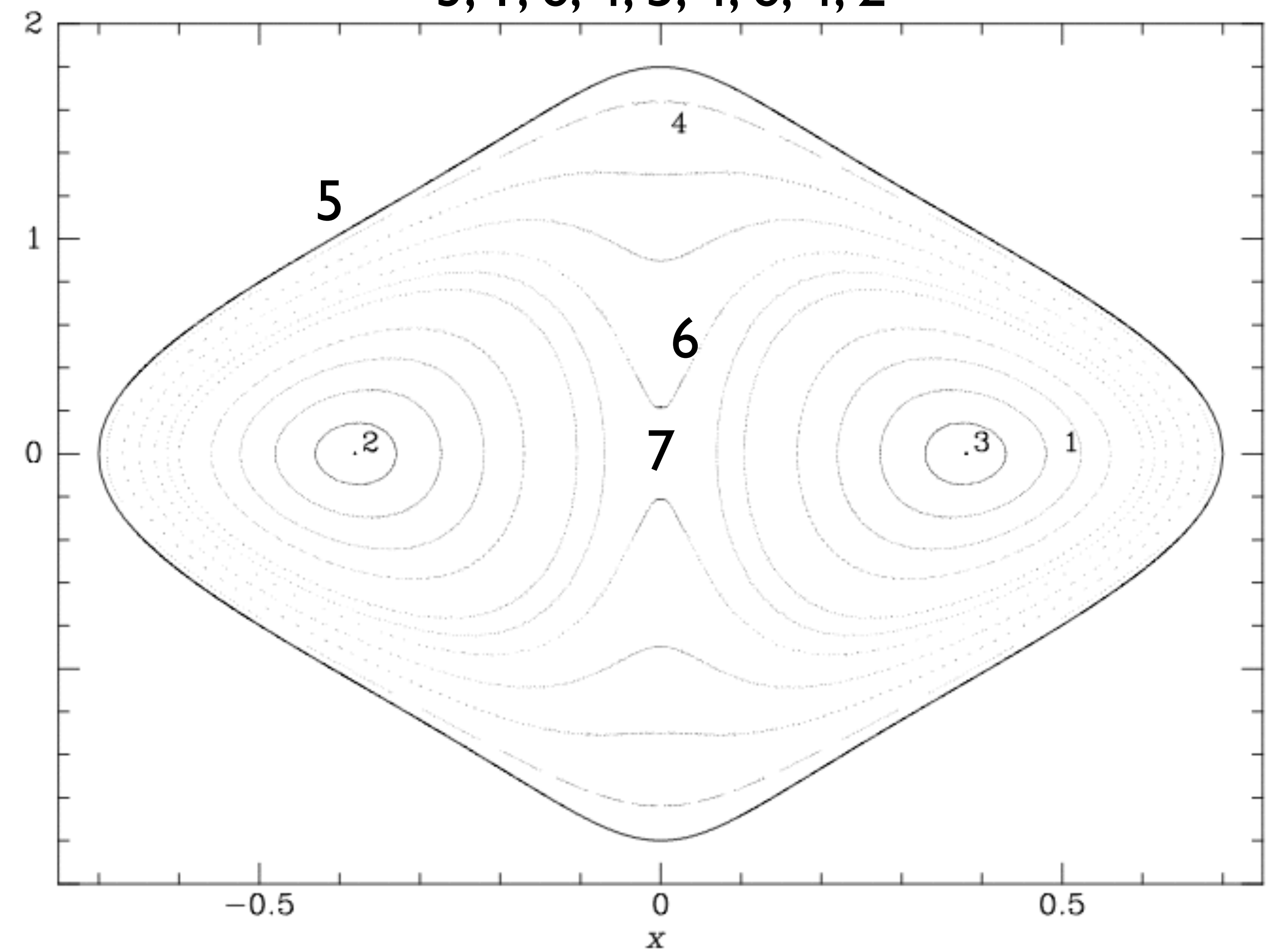

3.9 The $(x, \dot{x})$ surface of section formed by orbits in Φ_L of the same energy as the lepicted in Figure 3.8. The isopotential surface of this energy cuts the long axis at . The curves marked 4 and 1 correspond to the box and loop orbits shown in the l bottom panels of Figure 3.8.

what about 7?

$$\Phi_L(x, y) = \tfrac{1}{2} v_0^2 \ln\left(R_c^2 + x^2 + \frac{y^2}{q^2}\right) \quad (0 < q \le 1). \qquad (3.103)$$

Box/Loop —- connection with the spheroidal coordinates

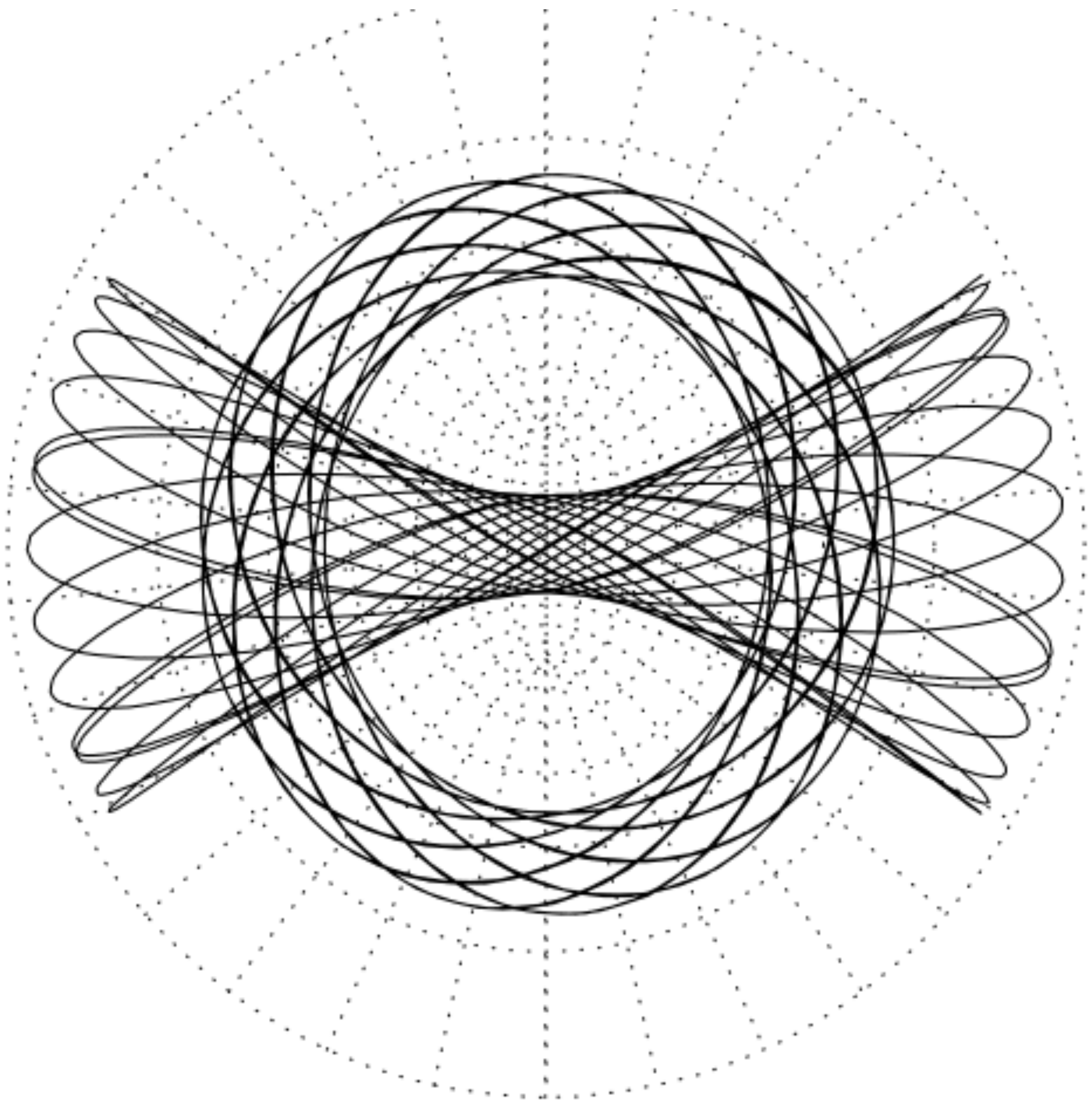

Figure 3.30 The boundaries of loop and box orbits in barred potentials approximately coincide with the curves of a system of spheroidal coordinates. The figure shows two orbits in the potential Φ_{L} of equation (3.103), and a number of curves on which the coordinates u and v defined by equations (3.267) are constant.

The advance of box

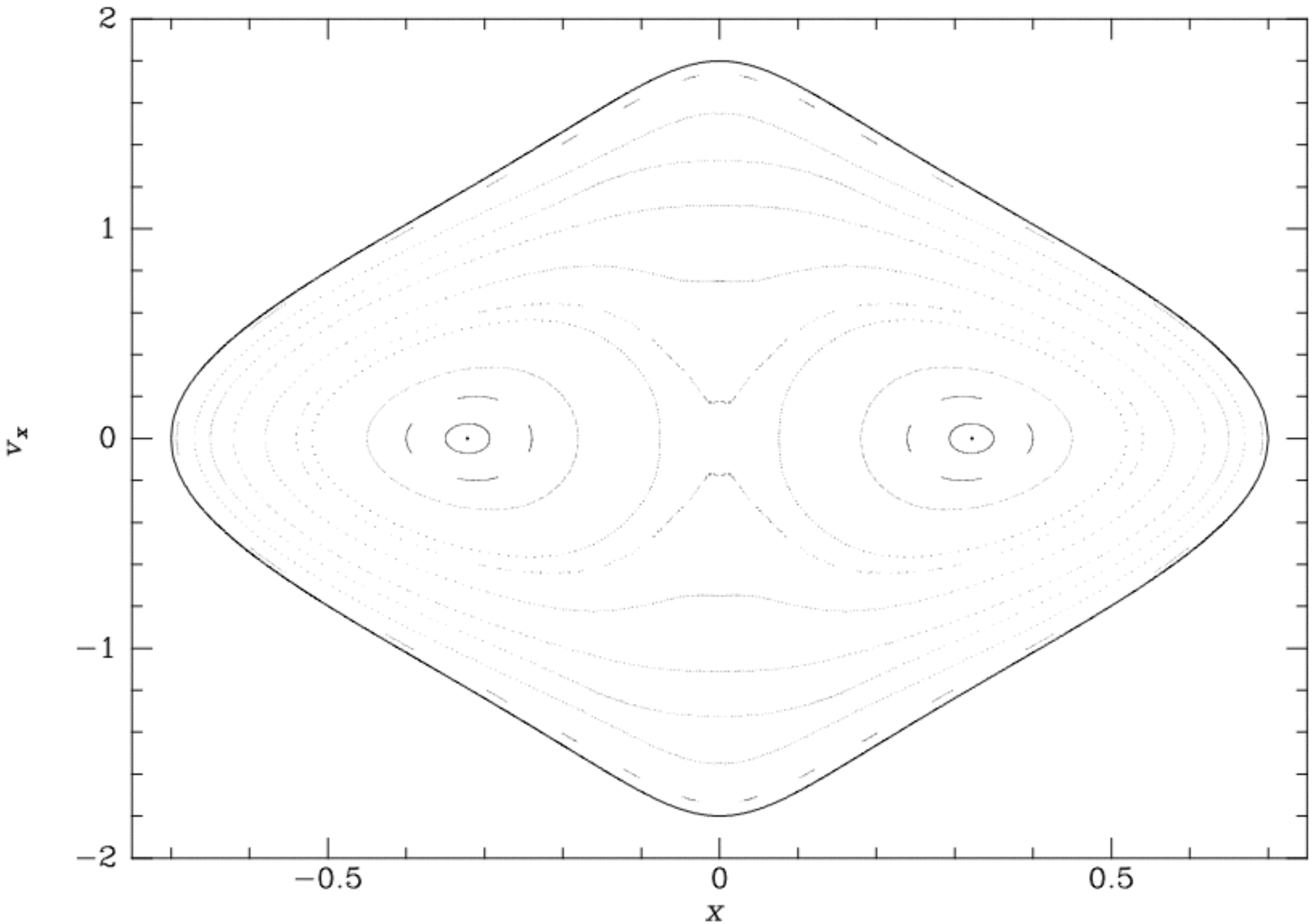

Figure 3.12 When the potential Φ_L is made more strongly barred by diminishing q, the proportion of orbits that are boxes grows at the expense of the loops: the figure shows the same surface of section as Figure 3.9 but for $q = 0.8$ rather than $q = 0.9$.

Possibility of resonant orbits — leading to chaos

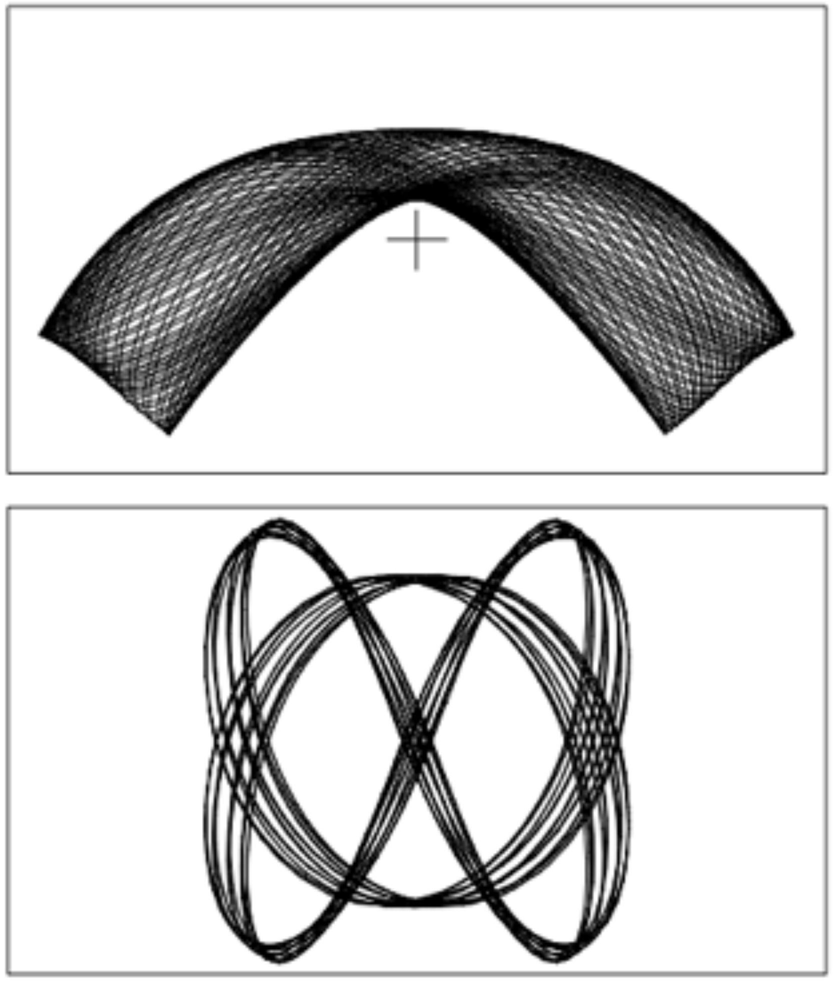

Figure 3.40 The appearance in real space of a banana orbit (top) and a fish orbit (bottom). In the upper panel the cross marks the center of the potential. Resonant box orbits of these types are responsible for the chains of islands in Figure 3.39. The banana orbits generate the outer chain of four islands, and the fish orbits the chain of six islands further in.

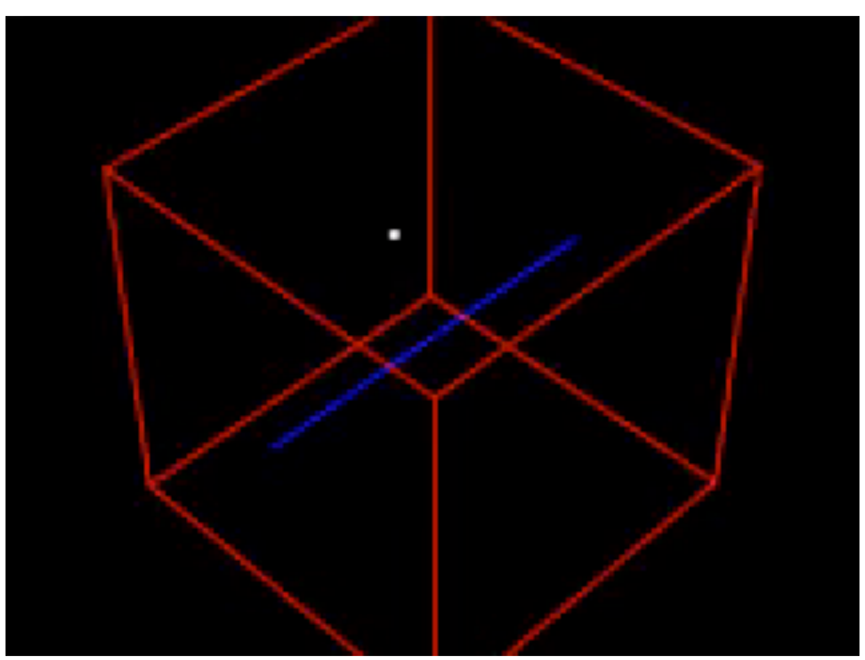

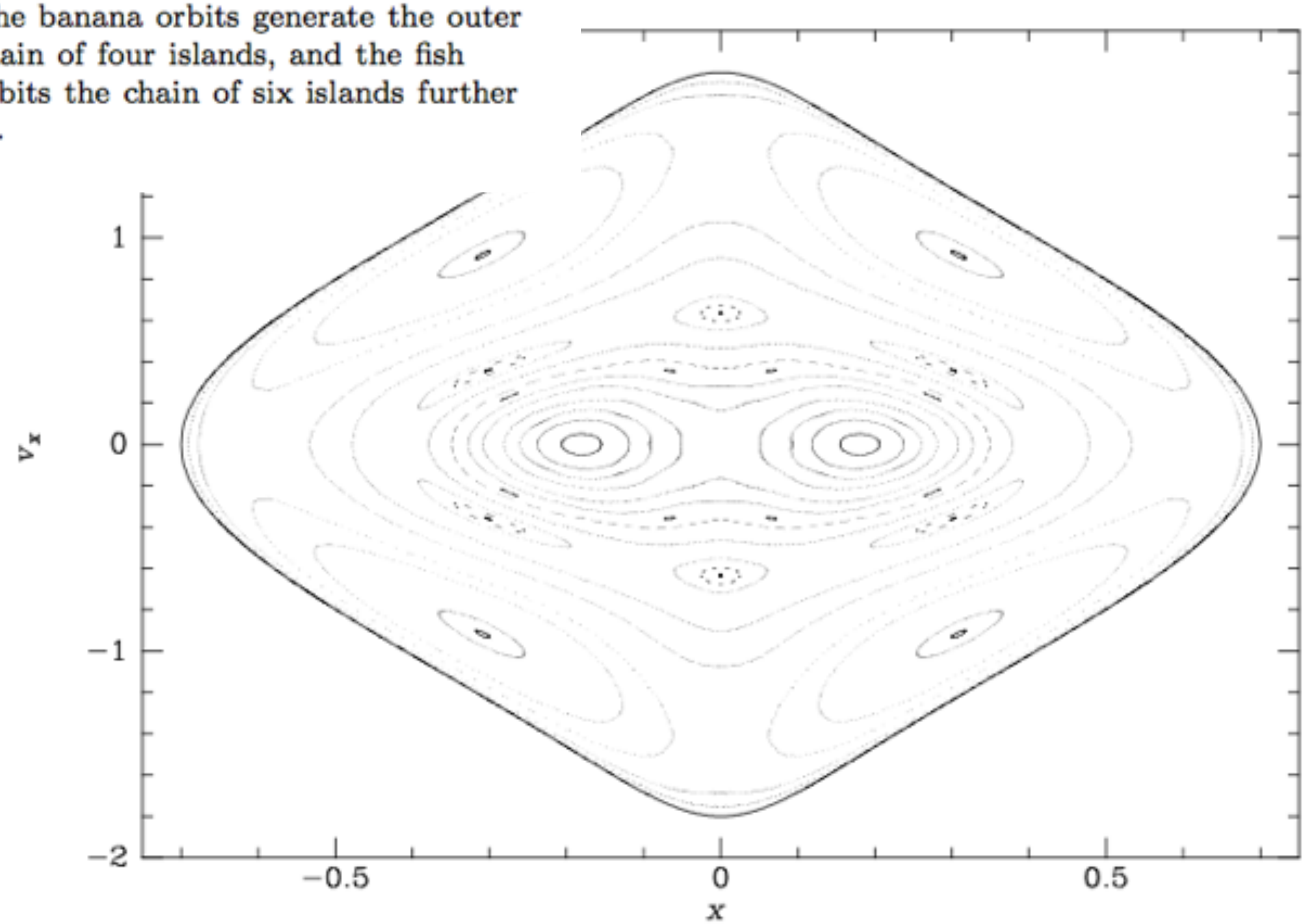

Figure 3.39 A surface of section for motion in Φ_L (eq. 3.103) with $q = 0.6$.

Rotating bars

if potential static in time: E conserved

if potential time-varying: E not conserved
periodic (rotation)
aperiodic

$$E = \frac{1}{2}v^2 + \Phi$$
$$\frac{dE}{dt} = v \cdot \frac{dv}{dt} + \frac{d\Phi}{dt} = -v \cdot \frac{d\Phi}{dr} + \frac{\partial \Phi}{\partial t} + v\frac{d\Phi}{dr} = \frac{\partial \Phi}{\partial t}$$

Lagrangian points of a rotating potential

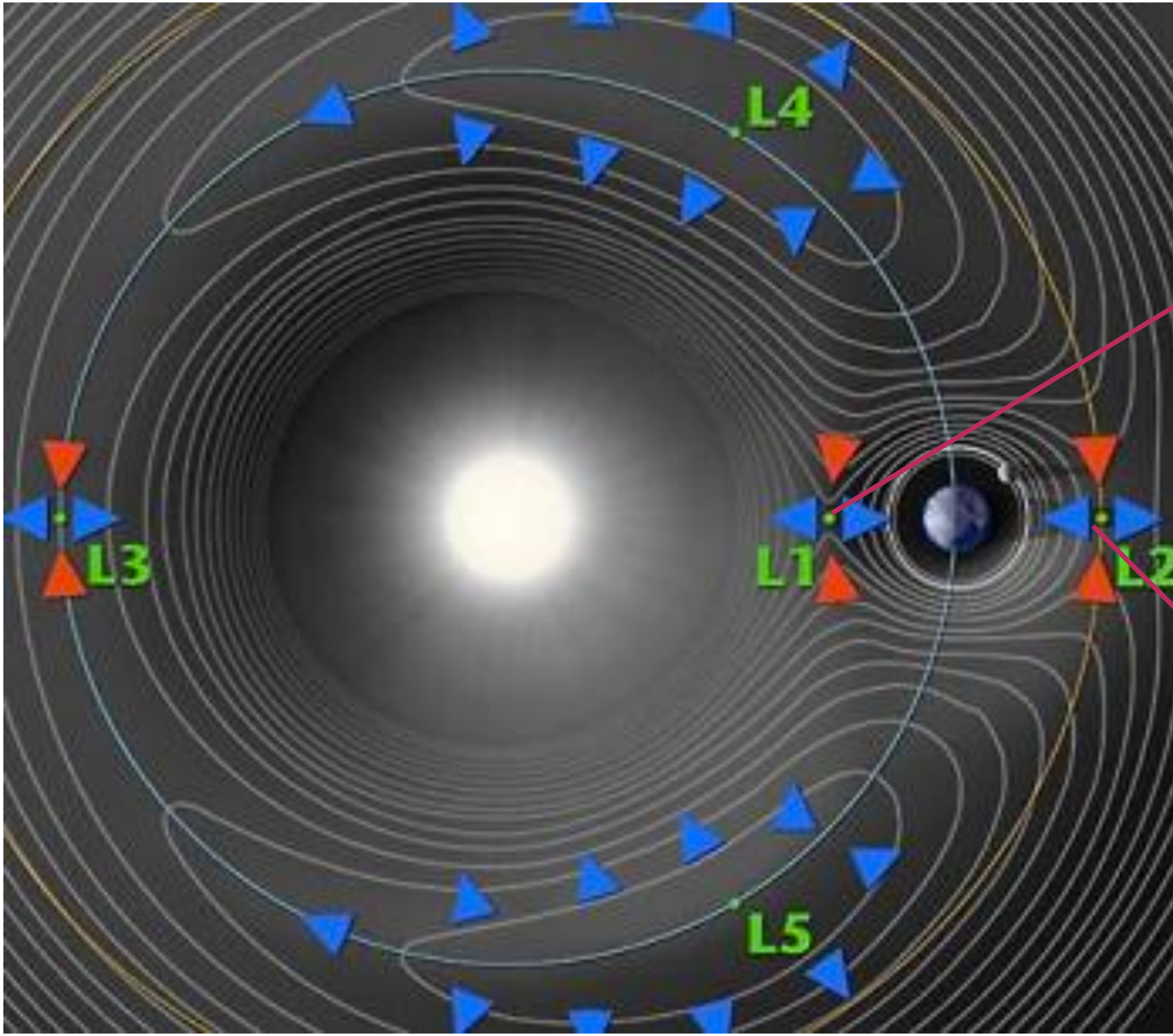

SOHO

WMAP

Planck

JWST

The singular logarithmic potential in two dimensions is represented by

$$\Phi = \tfrac{1}{2} \ln (x^2 + y^2/b^2) \, . \tag{2}$$

Miralda-Escude & Schwarzschild ’89

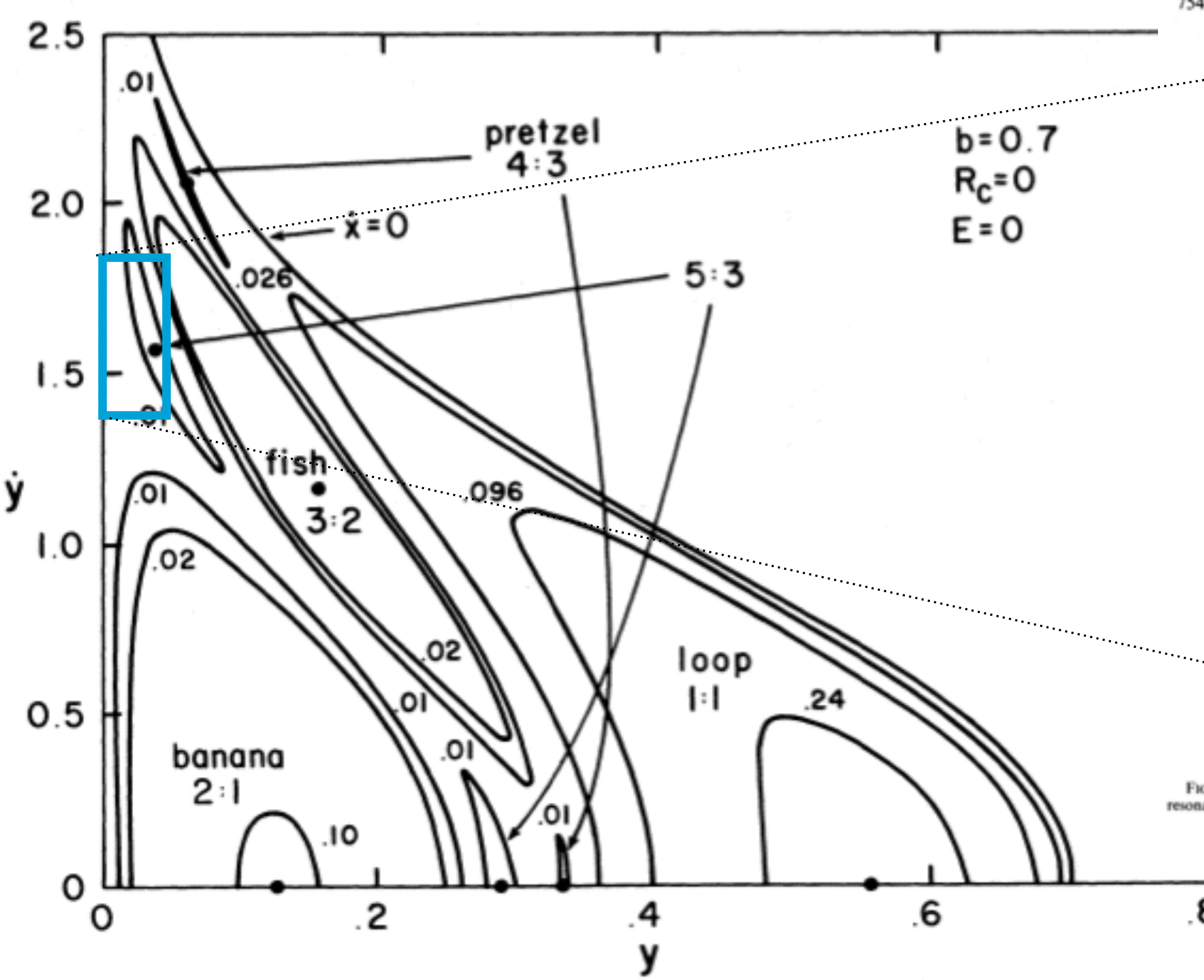

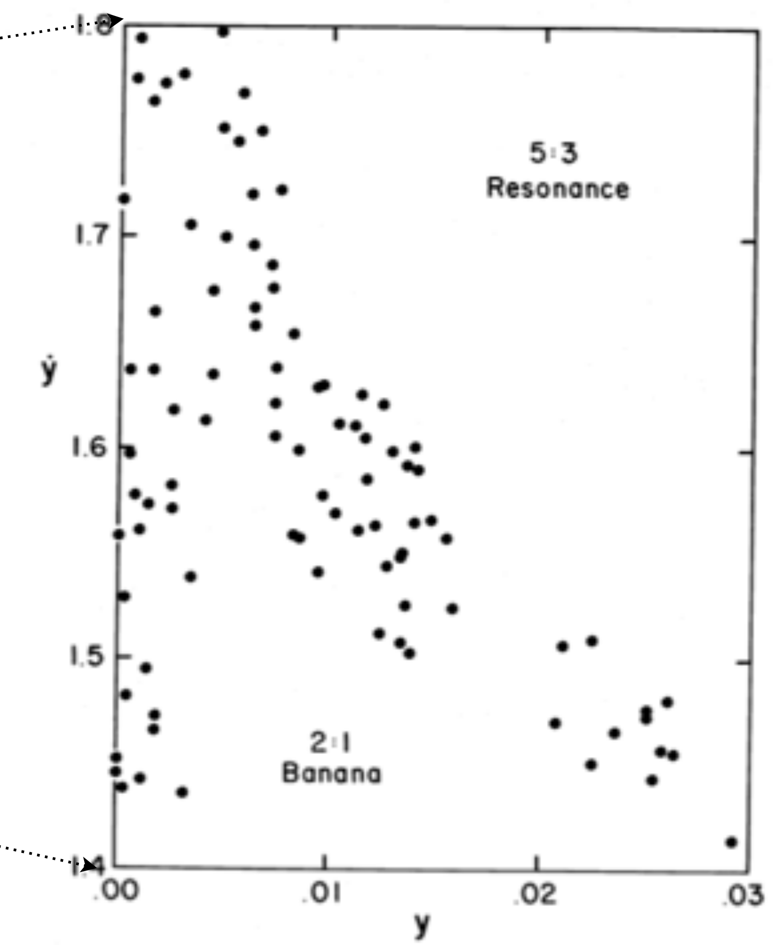

FIG. 3.—Stochastic orbit in small magnified portion of surface of section for $b = 0.7$ and $E = 0$. Adjacent to the stochastic resonance (*above*) and the 2:1 banana (*below*).

FIG. 1.—Surface of section for singular logarithmic potential with axis ratio $b = 0.7$. The invariant curves are labeled with their r_{min} values. Dots represent closed orbits.

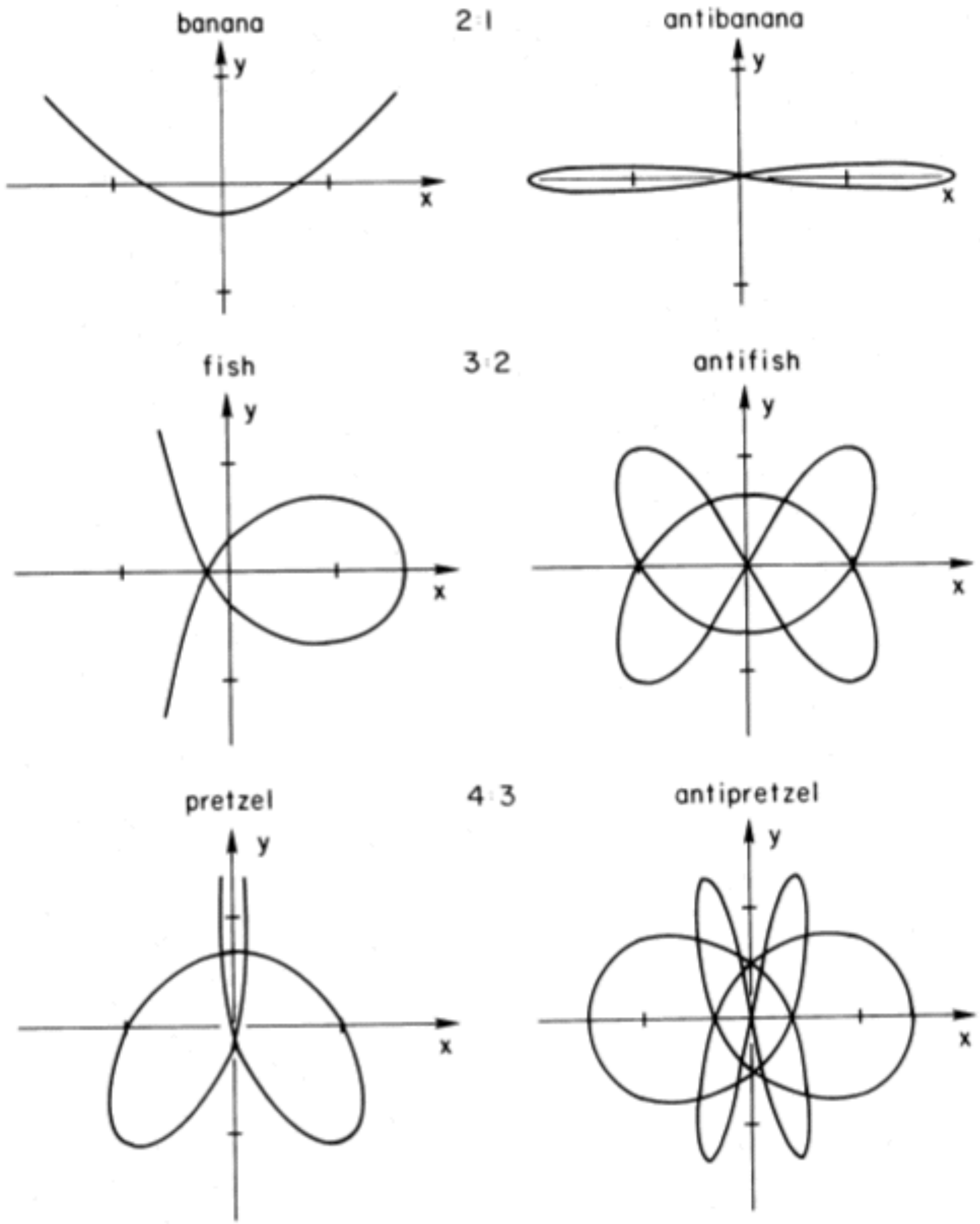

G. 4.—Closed boxlets in the singular logarithmic potential with axis ratio $b = 0.7$. *Left*: centrophobic (stable). *Right*: centrophilic (unstable).

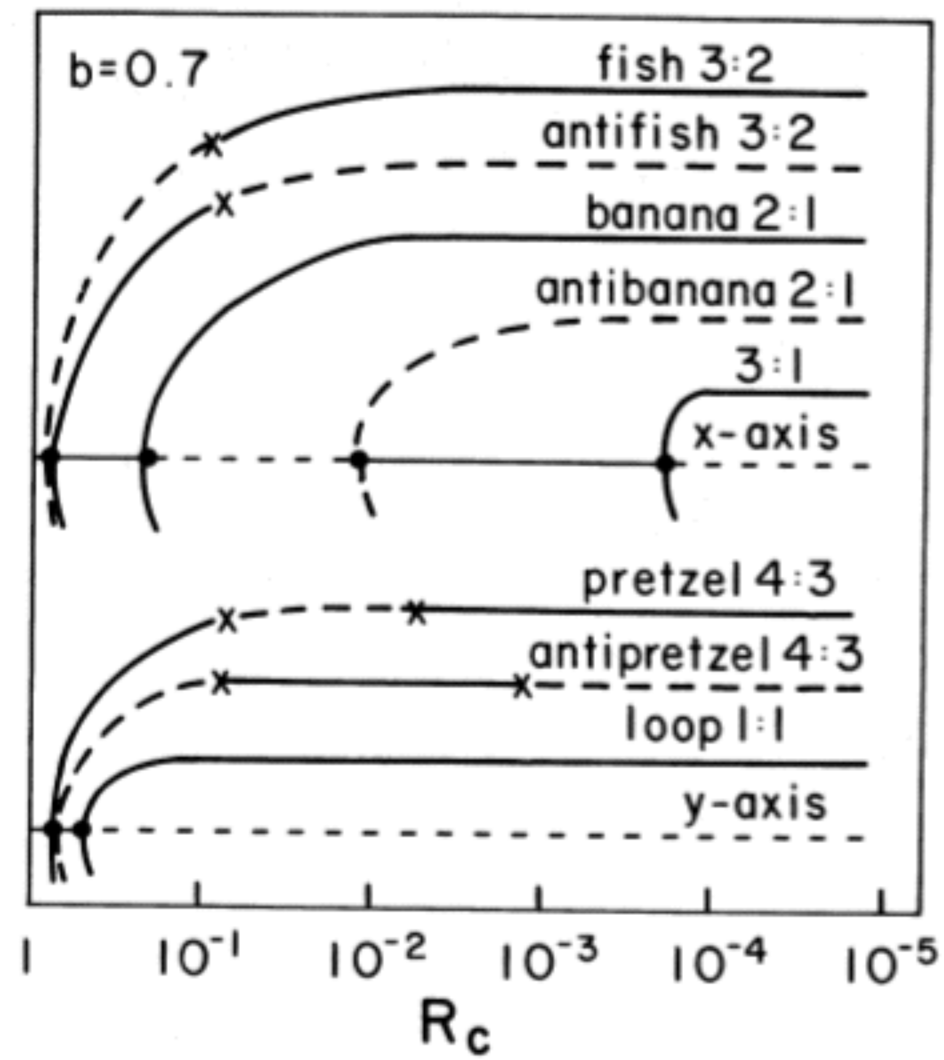

FIG. 5.—Schematic bifurcation diagram for $b = 0.7$. *Solid lines*: stable orbits. *Dashed lines*: unstable orbits. *Dots*: bifurcations of boxlets from axial orbits. *Crosses*: bifurcations of higher resonances from boxlets.

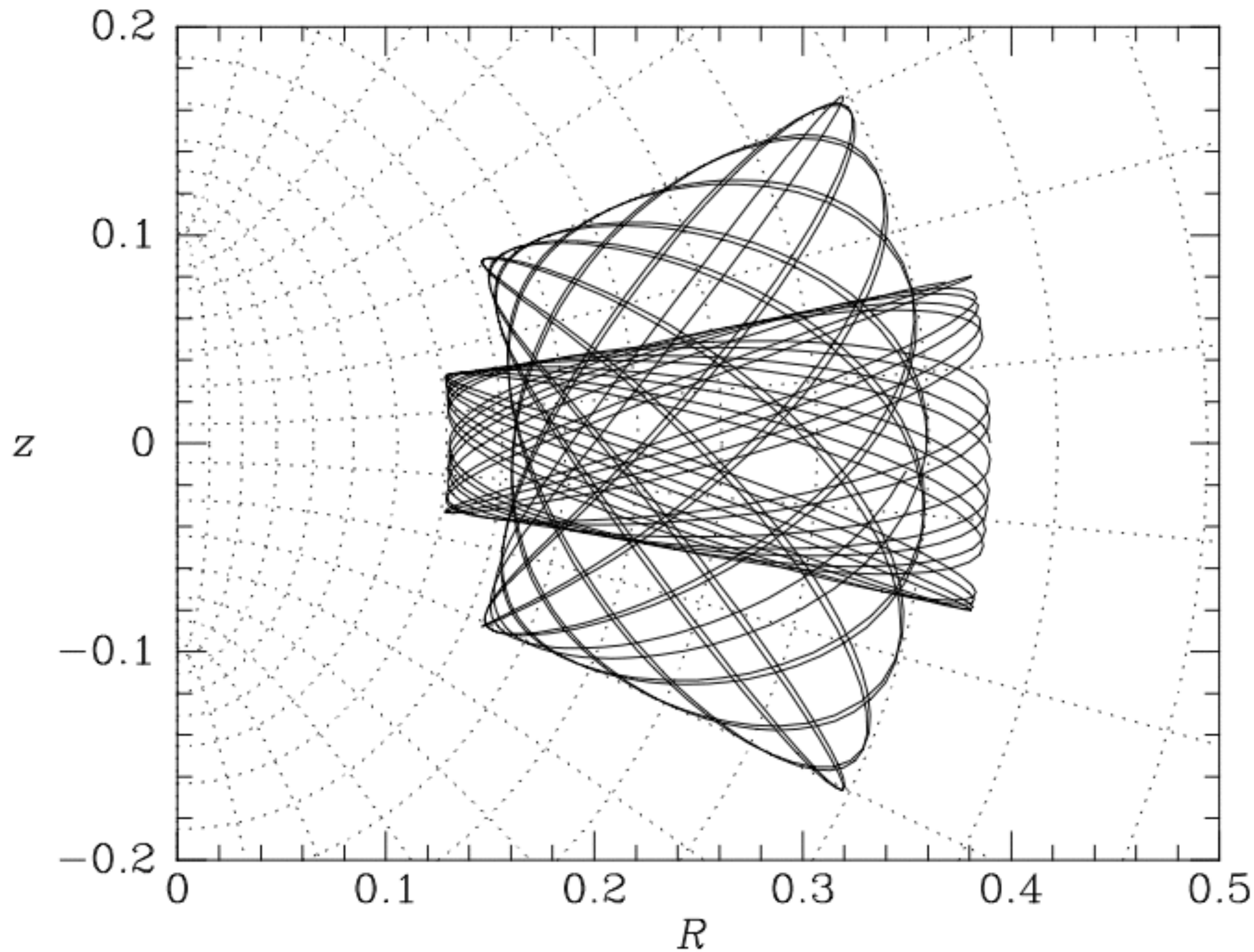

Figure 3.27 The boundaries of orbits in the meridional plane approximately coincide with the coordinate curves of a system of spheroidal coordinates. The dotted lines are the coordinate curves of the system defined by (3.242) and the full curves show the same orbits as Figure 3.4.

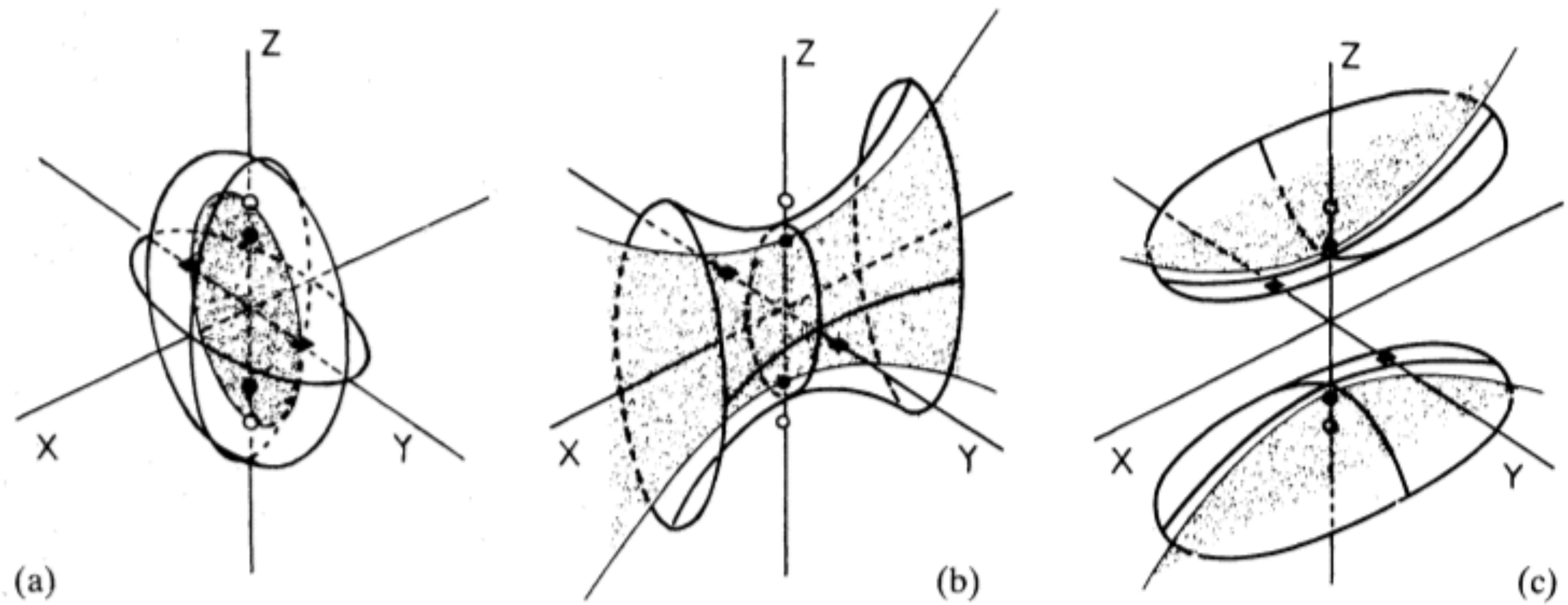

Figure 2. Ellipsoidal coordinates. The three pairs of foci are denoted by the open and filled circles and the filled squares. (a) Surfaces of constant λ are ellipsoids. The degenerate ellipsoid $\lambda=-\alpha$, inside the focal ellipse, is shaded. (b) Surfaces of constant μ are hyperboloids of one sheet. The degenerate hyperboloid $\mu=-\beta$, between the two branches of the focal hyperbola, is shaded. (c) Surfaces of constant ν are hyperboloids of two sheets. The degenerate hyperboloid $\nu=-\beta$ is shaded.

de Zeeuw '85

- spherical potential:
- Non-spherical potential: axisymmetric
- Non-spherical potential: non-axisymm.
  — planar 2-D
- Non-spherical potential: non-axisymm.
  — triaxial

Only 4?

touching the zero velocity surface

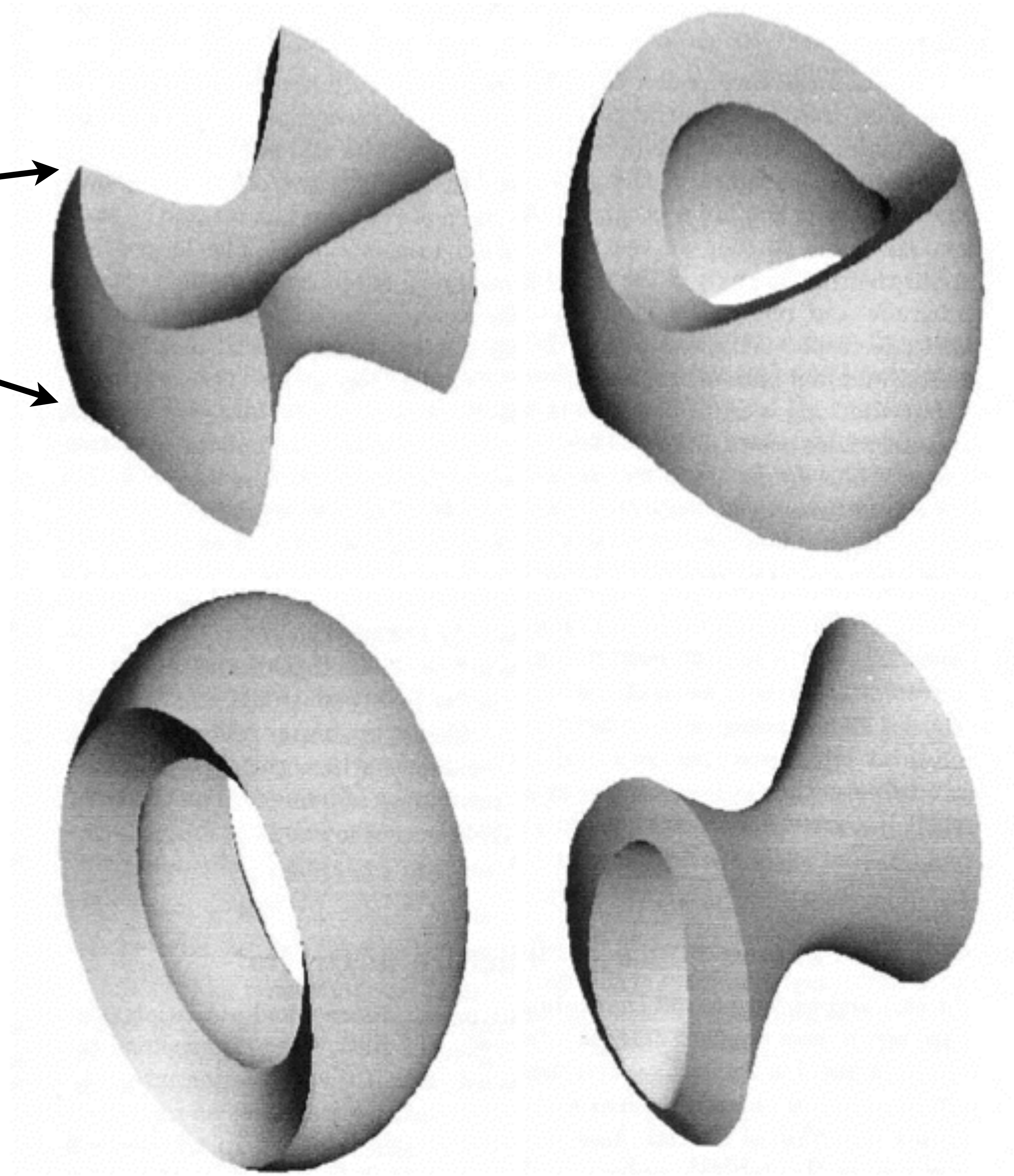

Figure 3.46 Orbits in a non-rotating triaxial potential. Clockwise from top left: (a) box orbit; (b) short-axis tube orbit; (c) inner long-axis tube orbit; (d) outer long-axis tube orbit. From Statler (1987), by permission of the AAS.

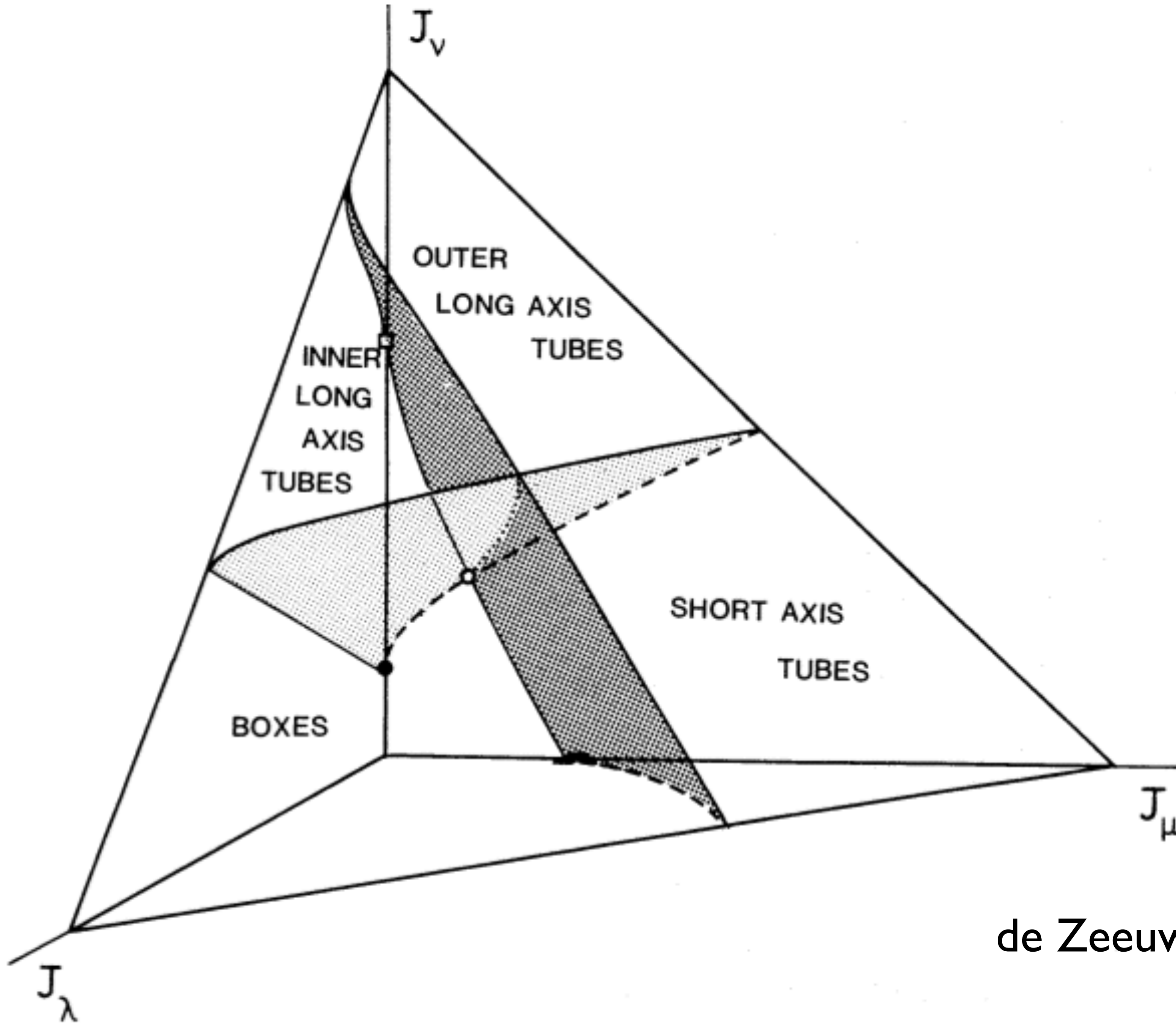

de Zeeuw '85

Figure 28. Action-diagram for the three-dimensional orbits in the perfect ellipsoid. The volumes occupied by the four families of general orbits are indicated. The locations of all limiting and transitional orbits are described in the text. The light and dark shaded surfaces correspond to the unstable orbits in the (x, z)- and (y, z)-plane, respectively. Dashed lines indicate simple periodic orbits that are unstable in one direction. The dotted line represents the z-axis orbits that are unstable in two directions. The filled and open circles and squares have the same meaning as in Section 5. The diagram is equivalent to Fig. 17.

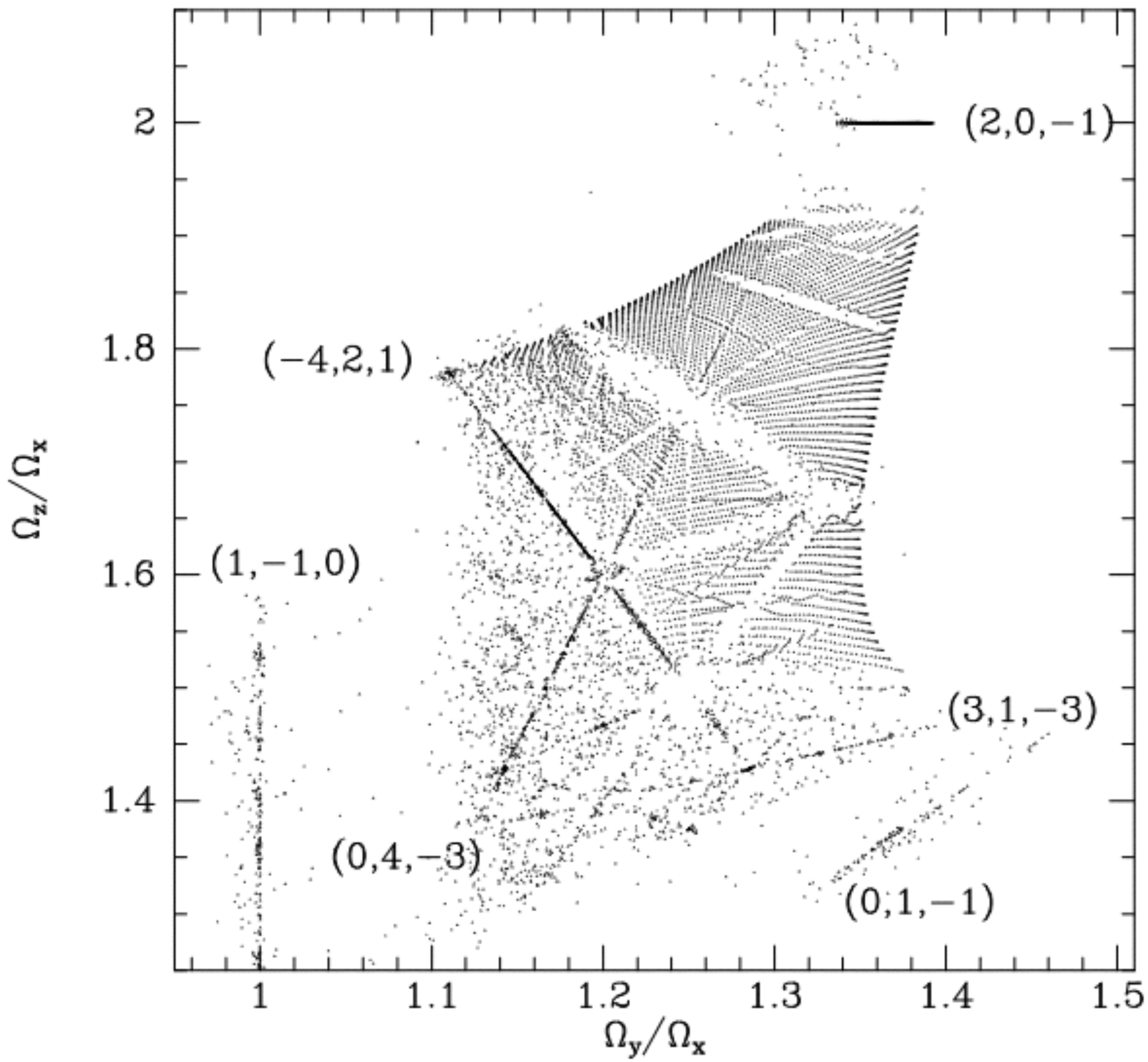

Figure 3.45 The ratios of orbital frequencies for orbits integrated in a three-dimensional non-rotating bar potential.

FMA was originally applied to the dynamics of planets by Jacques Lasker who in 1989 demonstrated that the dynamics of the solar system was chaotic. FMA initially applied to accelerators by Lasker and S. Dumas (PRL 1993). Lasker and D. Robin later extended the work to the ALS.

Frequency map analysis and particle accelerators
Laskar '03

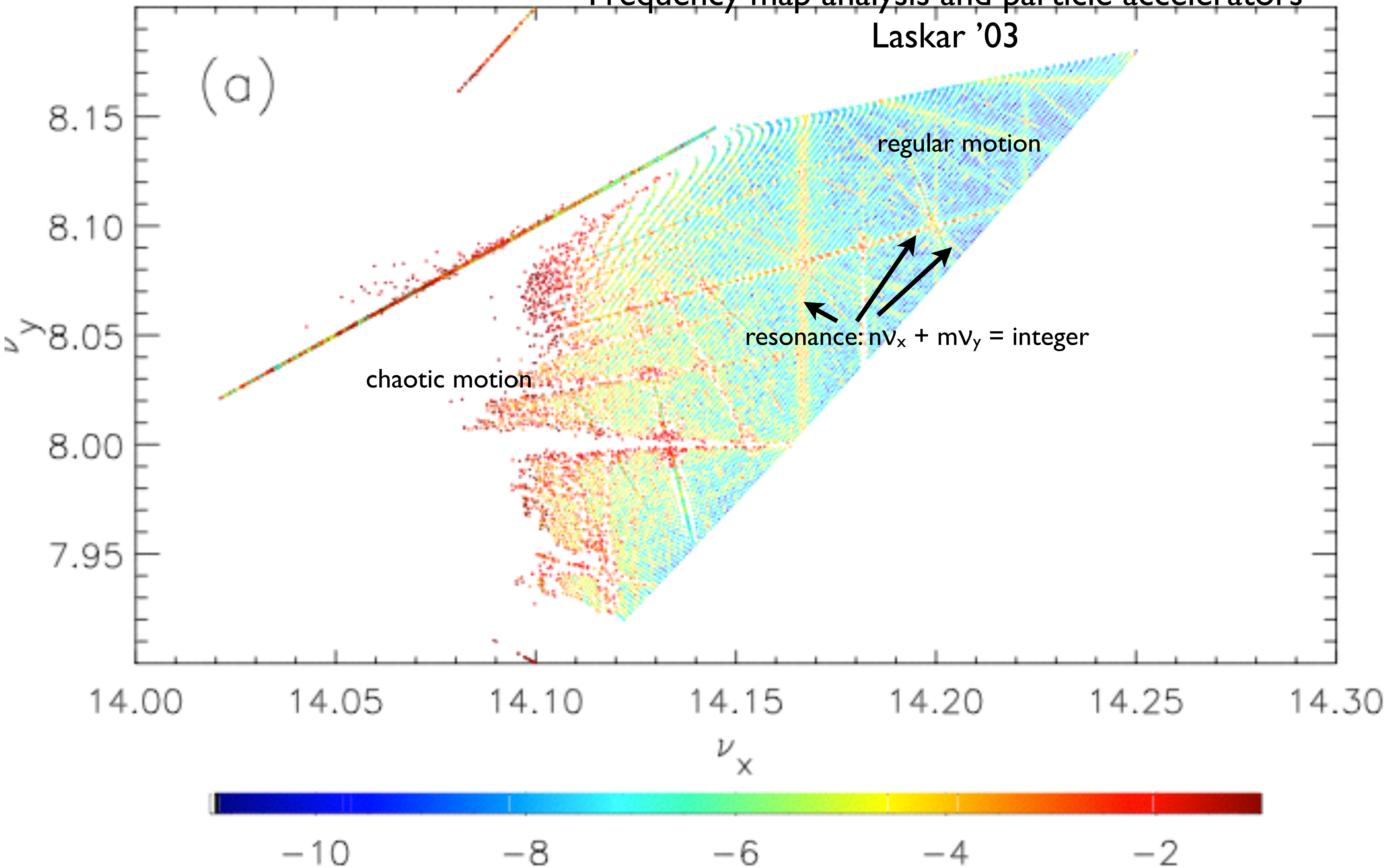

FMA - Introduction

- The oscillating electrons in the storage ring generally obey "quasi-harmonic" motion close to the origin for a "good working point".
- Large amplitudes sample more non-linear fields and motion becomes diffusive - i.e., the frequency of oscillation (tune) changes with turn number. Motion close to a resonance also exhibits diffusion.
- Frequency map analysis examines dynamics in frequency space rather than configuration space.
- Regular or quasi-regular periodic motion is a fixed point in frequncy space characterised by a tune value.
- Irregular trajectories exhibit diffusion in frequency space - with the tunes changing in time.
- The mapping of configuration space (x & y) to frequency space (Q_x & Q_y) will be regular for regular motion and irregular for chaotic or diffusive motion.
- Making a map - numerically integrate the equations of motion for a set of initial conditions (x, y, x',y') and compute the frequencies as a function of time (turn number)

FMA - Introduction

- FMA constructs the frequency map $F^T : (x,y) \rightarrow (Q_x, Q_y)$ from the space of initial conditions to tune space over a finite time span T by searching for quasi-periodic motion of the transverse motion.
- It is independent of the initial momenta (x'_0, y'_0)
- It converges as $1/T^4$ compared to $1/T$ for a FFT
- For regular motion it is invariant in time otherwise the time variation of the tunes called orbit diffusion gives a stability criterion.
- The study of the map gives information about resonances and nonlinear behaviour.

Synchrotron motion is generally ignored since the longitudinal tune compared to the transverse tunes is much smaller

FMA was originally applied to the dynamics of planets by Jacques Lasker who in 1989 demonstrated that the dynamics of the solar system was chaotic. FMA initially applied to accelerators by Lasker and S. Dumas (PRL 1993). Lasker and D. Robin later extended the work to the ALS.

Merritt '93 : Dynamics of Elliptical Galaxies (Science)

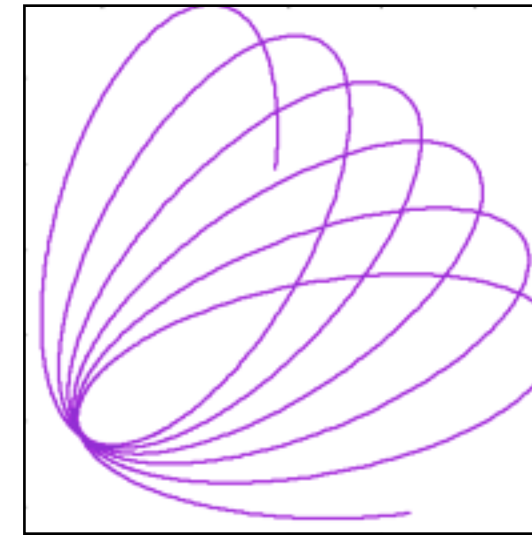

•spherical potential: precessing, planar motion (motion regular)

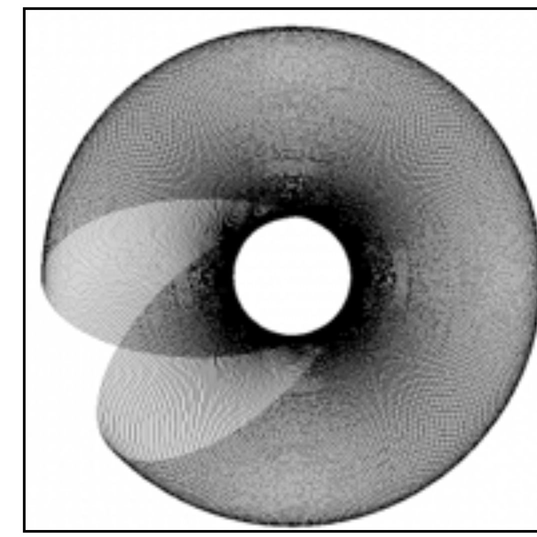

•axisymmetric potential: annular orbit precesses around z-axis, donut-shaped, typically 3 integrals of motion (motion all regular)

•triaxial potential:
when perfect ellipsoid (Stackel potential), regular
when general, often still integrals of motion
4 family of orbits
--boxy: centrophilic, dominating elliptical galaxies, but easily perturbed by central density/BH
--loopy: centrophobic, 3-groups

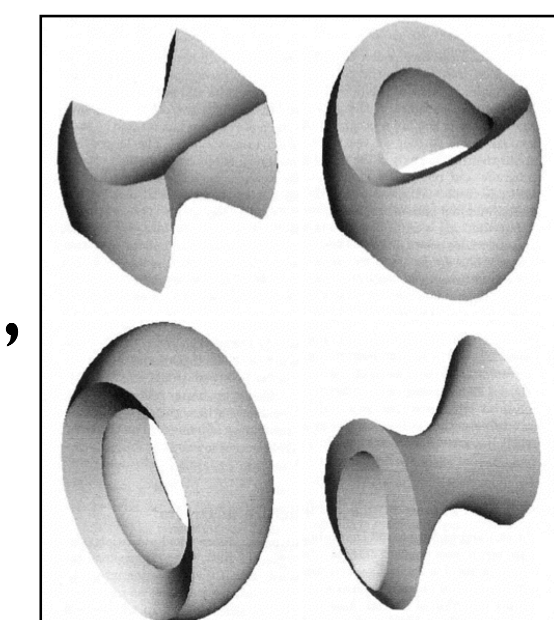

Eyre & Binney '10 "the Mechanics of Tidal Streams"

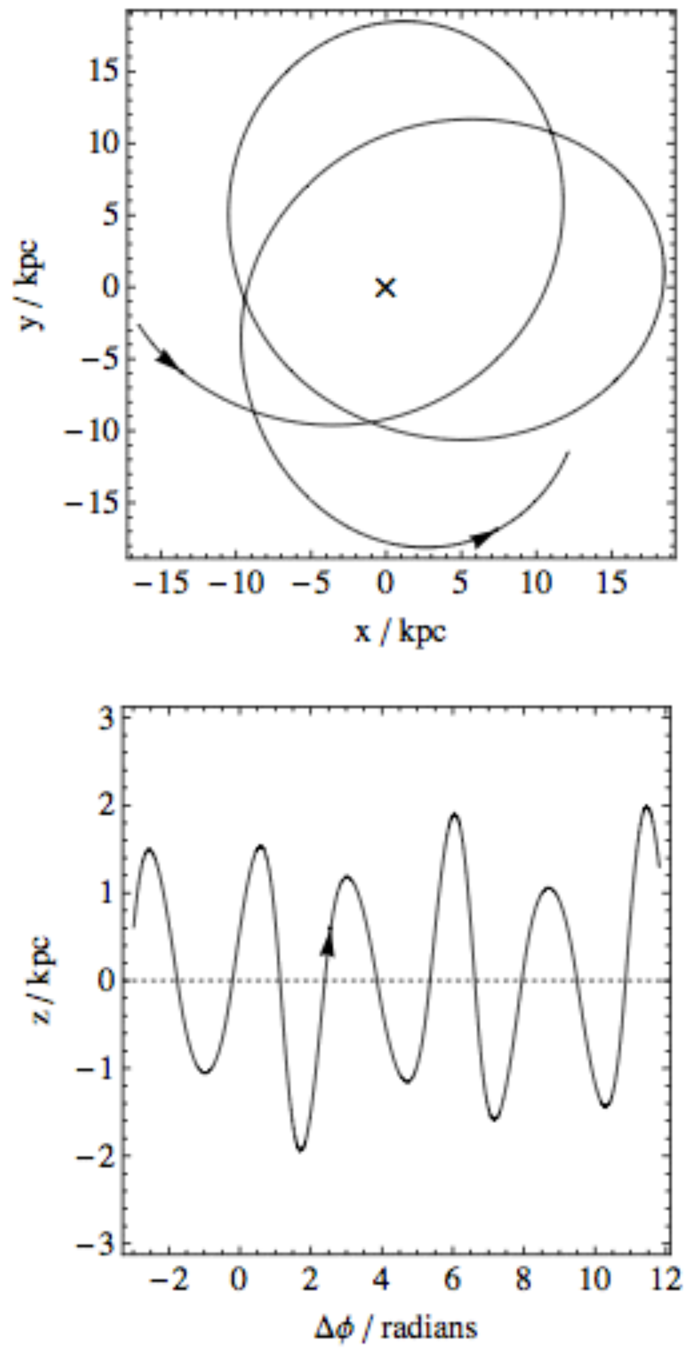

Figure 17. The real-space trajectory of the SO1 orbit in the Stäckel potential SP1. The upper panel shows a plan view of the galactic plane, while the lower panel plots height above the plane, z, against azimuthal coordinate, ϕ.

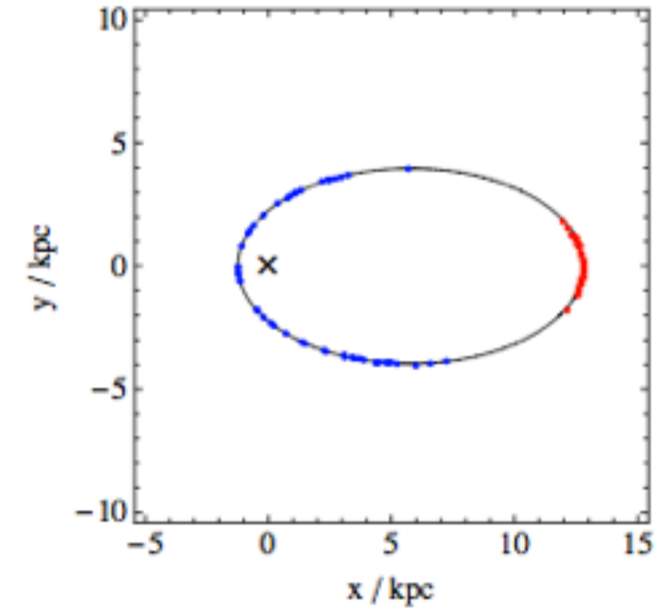

Figure 1. The solid line shows the orbit K1 (Table 1) in a Kepler potential, on which a cluster of 50 test particles has been evolved. The particles were released at apocentre. The red dots show the positions of the test particles near apocentre, after 24 complete orbits, at $t = 4.02\,\mathrm{Gyr}$. The blue dots show the same test particles near pericentre, approximately half an orbit later. In both cases, the dots delineate the progenitor orbit precisely.

Spherically symmetric (isochrone)

$$\Phi(r) = -\frac{GM}{b + \sqrt{b^2 + r^2}},$$

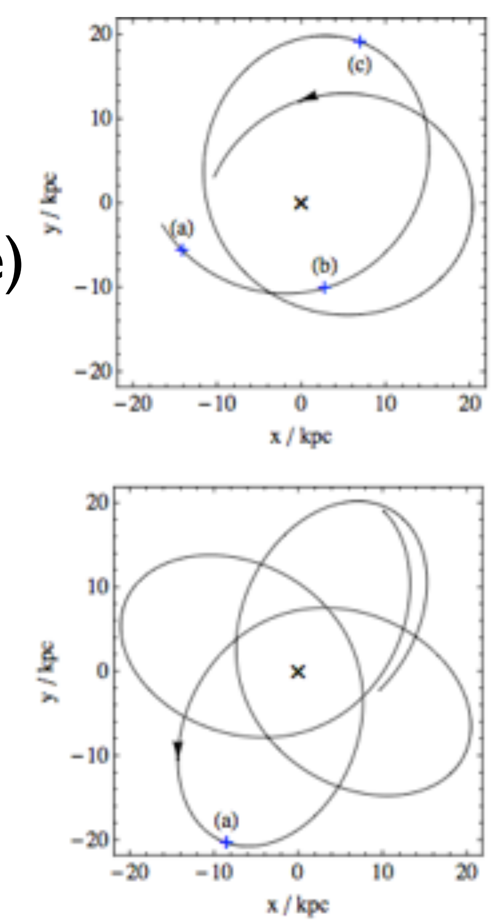

Figure 9. Plan views of the orbits used in this section. The top panel sho
I4, with (a), (b) and (c) marking the positions of the cluster corresponding

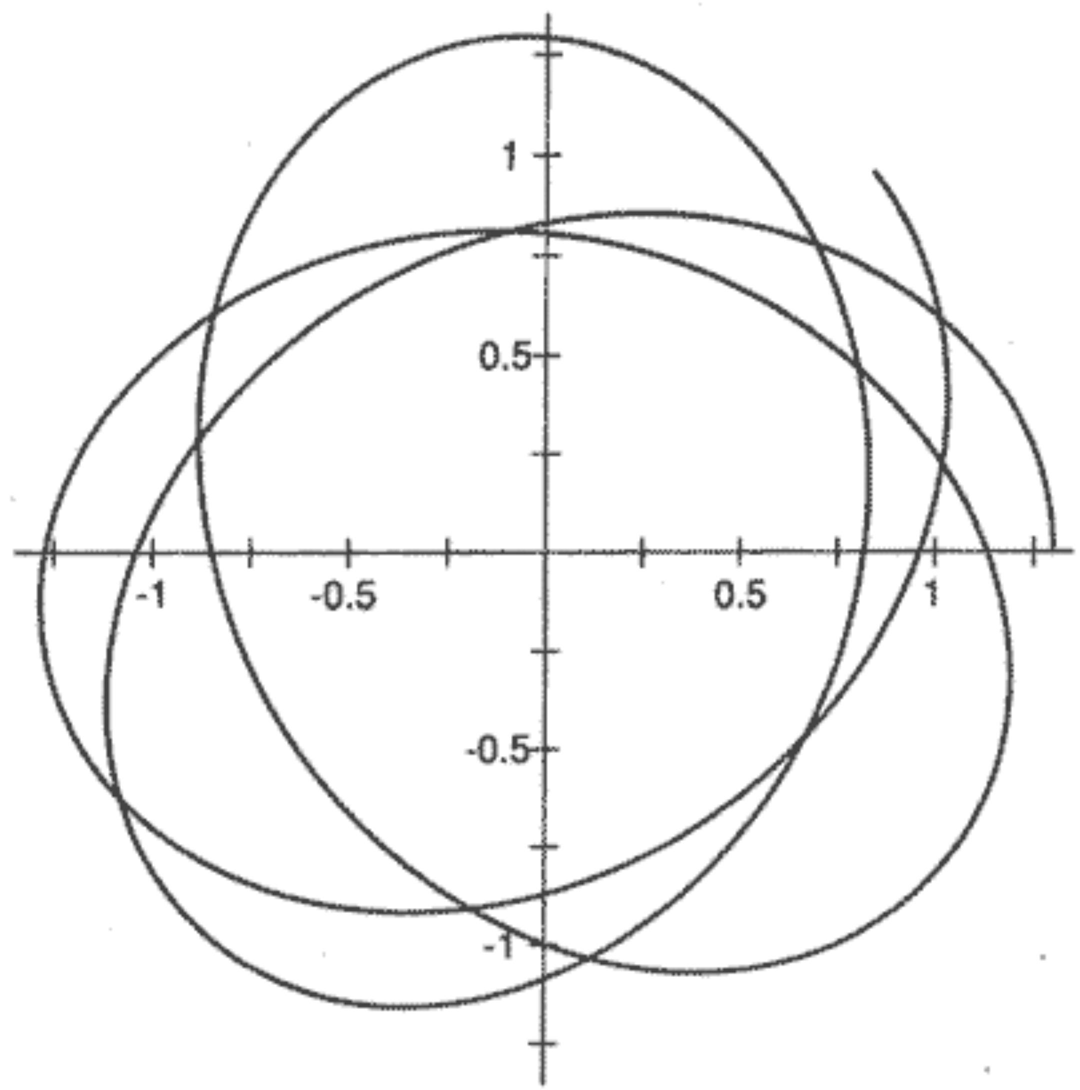

Figure 3.9 Path of the star of Figure 3.7, viewed from above the Galactic plane; the orbit started with ($R = 1.3,\ \phi = 0$) and ($\dot{R} = 0,\ R\dot{\phi} = 0.4574$).